EXCITED STATE DYNAMICS OF ATMOSPHERIC SPECIES: COLLISIONAL QUENCHING OF OH $A\ ^2\Sigma^+$ AND PHOTODISSOCIATION OF CH_2I_2 AND CH_2OO

Julia H. Lehman

A DISSERTATION

in

Chemistry

Presented to the Faculties of the University of Pennsylvania

in

Partial Fulfillment of the Requirements for the

Degree of Doctor of Philosophy

2013

Marsha I. Lester, Edmund J. Kahn Distinguished Professor
Supervisor of Dissertation

Gary Molander, Hirschmann-Makineni Professor of Chemistry
Graduate Group Chairperson

Dissertation Committee:

Feng Gai, Professor of Chemistry
Michael R. Topp, Professor of Chemistry
Jeffery G. Saven, Associate Professor of Chemistry

EXCITED STATE DYNAMICS OF ATMOSPHERIC SPECIES: COLLISIONAL QUENCHING OF OH $A\,^2\Sigma^+$ AND PHOTODISSOCIATION OF CH_2I_2 AND CH_2OO

DEDICATION

To my family.

ACKNOWLEDGMENTS

First and foremost, I want to thank my advisor, Professor Marsha I. Lester. She has been an inspiration and a huge influence on me over the last five years. Her enthusiasm for science is contagious and she has an incredible ability to convey her knowledge through teaching and discussion. Her guidance and encouragement has gotten me to where I am today and where I hope to be in the future. I also thank my dissertation committee, Professors Feng Gai, Michael Topp, and Jeffery Saven, for their support, encouragement, and stimulating scientific discussions.

I also thank many of the former and current Lester group members: Dr. Joseph M. Beames and Dr. Bridget A. O'Donnell for always keeping the group office entertaining and a place open for any discussion, no matter how many "stupid questions" are asked; Dr. Logan P. Dempsey, my fantastic lab mentor for the brief time we overlapped, who taught me how to run experiments and how "quenching" occurs; and the continuing members of the lab, especially Fang Liu and Hongwei Li.

Last, but certainly not least, I want to thank my family. You have all been so supportive and encouraging throughout my education and I thank you for that. I truly appreciate the endless notecards, constant supply of delicious food, and of course the weekend visits and phone conversations. Thank you.

ABSTRACT

EXCITED STATE DYNAMICS OF ATMOSPHERIC SPECIES: COLLISIONAL QUENCHING OF OH $A\ ^2\Sigma^+$ AND PHOTODISSOCIATION OF CH_2I_2 AND CH_2OO

Julia H. Lehman

Marsha I. Lester

This thesis focuses on the nonradiative disposal of energy following electronic excitation of atmospherically relevant species. Specifically, this work examines (1) removal of population from electronically excited OH $A\ ^2\Sigma^+$ through collisions with molecular partners via regions of conical intersection and (2) UV photodissociation of diiodomethane, CH_2I_2, and the simplest Criegee intermediate, CH_2OO. By mapping out product translational and/or internal energy distributions from these events, insights are gained into the mechanism and/or dynamics by which such processes occur.

Products from nonreactive and/or reactive quenching of OH/D $A\ ^2\Sigma^+$ by H_2, O_2, CO, and Kr are studied using a laser pump-probe scheme with fluorescence detection, determining the OH/D $X\ ^2\Pi$ product state distribution that results from nonreactive quenching and/or the product translational energy release to H, D, or O-atoms as a result of reactive quenching. By comparing with complementary theory, the outcomes of collisional quenching are shown to provide experimental observables that reflect on the nonadiabatic coupling as the system evolves to nonreactive or reactive products through regions of conical intersection (CI). Significant rotational excitation of the OH $X\ ^2\Pi$ nonreactive products is indicative of a strong torque placed on OH in the vicinity of the CI, while minimal vibration shows that the OH bondlength is essentially unchanged in

the quenching process. The kinetic energy release to H, D, and O-atom reaction products and the corresponding internal energy of the correlated fragments provide additional insights on the forces or geometric configurations in the vicinity of the CIs.

The photodissociation dynamics of CH_2I_2 and CH_2OO are also examined using a laser pump-probe scheme with ionization detection of the I- or O-atom fragments. The ionized products are detected with a newly built velocity map ion imaging apparatus giving mass and 2D spatial resolution. The product translational energy distributions derived from the image yield the nascent internal energy distributions of the molecular cofragments as well as the ground state binding energy for CH_2OO. The angular distributions are indicative of prompt dissociation and the character of the electronic state(s) involved in dissociation process.

TABLE OF CONTENTS

DEDICATION ..... **III**

ACKNOWLEDGMENTS ..... **IV**

ABSTRACT ..... **V**

TABLE OF CONTENTS ..... **VII**

LIST OF TABLES ..... **XI**

LIST OF ILLUSTRATIONS ..... **XII**

CHAPTER 1
INTRODUCTION **1**

References **13**

CHAPTER 2
COLLISIONAL QUENCHING OF OD $A\ ^2\Sigma^+$ BY H_2: EXPERIMENTAL AND THEORETICAL STUDIES OF THE STATE-RESOLVED OD $X\ ^2\Pi$ PRODUCT DISTRIBUTION AND BRANCHING FRACTION **16**

I. Introduction **17**

II. Experimental Methods **22**

III. Theoretical Methods **24**

IV. Results **24**
A. OD $A\ ^2\Sigma^+$ Lifetimes 24
B. OD $X\ ^2\Pi$ Product State Distribution 26
C. Branching Fraction for OD $X\ ^2\Pi$ Products 33

V. Discussion **35**
A. Hydroxyl Product Vibrational Distribution 35
B. Hydroxyl Product Rotational Distribution 36
C. Branching Fraction for Nonreactive Quenching 41

VI. Conclusions **44**

Acknowledgments **45**

References **45**

CHAPTER 3
REACTIVE QUENCHING OF OD $A\ ^2\Sigma^+$ BY H_2: TRANSLATIONAL ENERGY DISTRIBUTIONS FOR H- AND D-ATOM PRODUCT CHANNELS 48

I. Introduction 49

II. Experimental Methods 55

III. Results 58
A. Doppler profiles of H- and D-atom products 58
B. Analysis of Doppler profiles 62
C. Translational energy distributions 66

IV. Discussion 67

V. Conclusions 77

Acknowledgements 79

References 79

CHAPTER 4
REACTIVE QUENCHING OF OH $A\ ^2\Sigma^+$ BY O_2 AND CO: EXPERIMENTAL AND NONADIABATIC THEORETICAL STUDIES OF H- AND O-ATOM PRODUCT CHANNELS 81

I. Introduction 82

II. Experimental Methods 88

III. Experimental Results 91
A. Quenching of OH $A\ ^2\Sigma^+$ by O_2 and CO 91
B. H-atom Products of Reactive Quenching 93
C. O-atom Products of Reactive Quenching 101
D. Branching to Reactive Quenching 103

IV. Theoretical Methods 106

V. Theoretical Results 109
A. Locus of Points of Conical Intersection 109
B. Local Topography of Conical Intersection 116

VI. Discussion 122
A. Branching to Quenching Product Channels 122
B. Connections to Regions of Conical Intersection 123

VII. Conclusions 127

Acknowledgements 129

References 130

CHAPTER 5
ELECTRONIC QUENCHING OF OH $A\ ^2\Sigma^+$ INDUCED BY COLLISIONS WITH Kr ATOMS 133

I. Introduction 134

II. Experimental Methods 139
A. Lifetime and Population Measurements 139
B. Thermally averaged electronic quenching cross-sections. 140

III. Experimental Results 142
A. OH $A\ ^2\Sigma^+$ Lifetimes 142
B. OH $A\ ^2\Sigma^+$ Electronic Quenching Cross-Sections. 144
C. OH $X\ ^2\Pi$ Product State Distribution. 146

IV. Theoretical Methods and Results 149
A. Potential Energy Surfaces and Couplings. 149
B. Trajectory Surface Hopping Calculations 156

V. Discussion 159

VI. Conclusions 164

Acknowledgements 165

References 165

CHAPTER 6
ION IMAGING STUDIES OF THE PHOTODISSOCIATION DYNAMICS OF CH_2I_2 AT 248 NM 170

I. Introduction 171

II. Experimental Methods 174

III. Results 177
A. TKER Distribution 177
B. Angular Distribution 182

IV. Discussion 184

V. Conclusion 187

References 189

CHAPTER 7
UV PHOTODISSOCIATION DYNAMICS OF CH_2OO 191

References 204

APPENDIX I
DOPPLER PROFILE ANALYSIS PROCEDURE 206

I. Analysis Procedure 207

II. Reanalysis of H/D-atom Doppler profiles from OH $A\ ^2\Sigma^+ + D_2$ 210

III. Revised analysis of H-atom Doppler profile for OH $A\ ^2\Sigma^+ + H_2$.....212

References 216

APPENDIX II
PHOTODISSOCIATION OF CH_2I_2 AT 313 NM..... 217

References 220

LIST OF TABLES

CHAPTER 2 16

Table 1. Observables derived from experiment and theory on the OH/D products of nonreactive quenching from OH or OD $A\ ^2\Sigma^+$ with H_2 31

CHAPTER 4 81

Table 1. Parameters derived from the H-atom Doppler profiles obtained from the quenching of OH $A\ ^2\Sigma^+$ by O_2 and CO.....96

Table 2. Experimentally determined O 2p $^3P_{J=0,1,2}$ fine-structure population distribution after quenching of OH $A\ ^2\Sigma^+$ by O_2 or CO as well as the statistical fine-structure distribution based on degeneracy.....104

Table 3. Summary of experimentally determined product branching ratios following the quenching of OH $A\ ^2\Sigma^+$ by H_2, O_2, and CO. 107

Table 4. Geometric parameters, conical intersection parameters, and energies relative to the OH $A\ ^2\Sigma^+$ + CO asymptote for the four energy minimized crossings 113

Table 5. Geometric parameters for the OH-CO system at points along the seam of intersection identified leading to the R2 energy minimized crossing.....114

CHAPTER 7 191

Table 1. Characteristics of the total kinetic energy and anisotropic angular distributions derived from reconstructed images of O ^1D products following photolysis of CH_2OO at 308, 330, and 360 nm 196

APPENDIX I
DOPPLER PROFILE ANALYSIS PROCEDURE 206

Table 1. Parameters characterizing product translational energy distribution following reactive quenching of OH $A\ ^2\Sigma^+$ by H_2 and its isotopic variants 215

LIST OF ILLUSTRATIONS

CHAPTER 1 1

Figure 1. Simplified reaction coordinate for quenching of OH $A\ ^2\Sigma^+$ by H_2 via the C_{2v} HO-H_2 conical intersection 5

CHAPTER 2 16

Figure 1. Schematic diagram of the $2A'$ and $1A'$ potentials for OD ($A\ ^2\Sigma^+$, $X\ ^2\Pi$) + H_2 as a function of separation distance.....20

Figure 2. Experimentally measured OD $X\ ^2\Pi$ quantum state distribution arising from quenching of OD $A\ ^2\Sigma^+$ (v'=0, N'=0) by H_2 under single collision conditions 27

Figure 3. Theoretical OD $X\ ^2\Pi$ rovibrational distribution determined from classical trajectory calculations of the post-quenching dynamics of OD $A\ ^2\Sigma^+$ by H_2.....32

Figure 4. Experimental and theoretical OD $X\ ^2\Pi$ (v''=0) product state distributions compared with those for OH $X\ ^2\Pi$ (v''=0) following quenching of OD or OH $A\ ^2\Sigma^+$ by H_2.....39

Figure 5. The experimental and theoretical results from Fig. 4, OD $X\ ^2\Pi$ (v''=0) and OH $X\ ^2\Pi$ (v''=0) product state distributions, replotted as a function of OH or OD internal energy. 43

CHAPTER 3 48

Figure 1. Simplified reaction coordinate for quenching of OD $A\ ^2\Sigma^+$ by H_2 via the C_{2v} DO-H_2 conical intersection 52

Figure 2. Doppler profiles of H and D atom products from reactive quenching of OD $A\ ^2\Sigma^+$ by H_2, centered about their respective two-photon transitions.....59

Figure 3. Doppler profiles for H and D atom products arising from quenching of OD $A\ ^2\Sigma^+$ by H_2, which is replotted as Doppler shifts from line center 61

Figure 4. Translational energy distributions, $P(E_T)$, derived for the H- and D-atom products from reactive quenching of OH $A\ ^2\Sigma^+ + H_2$, OH $A\ ^2\Sigma^+ + D_2$, and OD $A\ ^2\Sigma^+ + H_2$ 65

Figure 5. Product translational energy distributions $P(E_T)$ for OD $A\ ^2\Sigma^+ + H_2 \rightarrow H + HOD$ and OD $A\ ^2\Sigma^+ + H_2 \rightarrow D + H_2O$ channels derived from experiment 71

Figure 6. Product translational energy distributions $P(E_T)$ for the dominant OH $A\ ^2\Sigma^+ + D_2 \rightarrow D +$ HOD channel 73

CHAPTER 4 81

Figure 1. Schematic energy level diagrams for quenching of initially prepared OH $A\ ^2\Sigma^+$ in collisions with O_2 and CO.....84

Figure 2. H-atom Doppler profiles of signals produced in reactive quenching of OH $A\ ^2\Sigma^+$ with O_2 and CO 94

Figure 3. Product translational energy distribution arising from reactive quenching of OH $A\ ^2\Sigma^+$ with O_2, producing H + O_3 98

Figure 4. Product translational energy distribution arising from reactive quenching of OH $A\ ^2\Sigma^+$ with CO, producing H + CO_2 100

Figure 5. O 2p $^3P_{J=0,1,2}$ fine-structure population distribution arising from reactive quenching of OH $A\ ^2\Sigma^+$ with O_2 and CO 102

Figure 6. Cartesian representations of the **g** and **h** vectors for the four main conical intersections identified for the OH + CO system 111

Figure 7. Cartesian representation of the **g** vectors on the C and O atoms and the atomic positions along the seam of intersection 115

Figure 8. Topography of the cone of conical intersection in the vicinity of the four identified conical intersections for the OH + CO system 119

Figure 9. Three dimensional plots of the cone of intersections in the OH + CO system for regions C1, M1, R1, and R2 121

CHAPTER 5 133

Figure 1. Experimentally determined OH $A\ ^2\Sigma^+$ total decay rates for v=0 and v=1 as a function of rotational level in the collisional region of the supersonic expansion 143

Figure 2. Electronic quenching cross-sections for OH $A\ ^2\Sigma^+$ with Kr under thermal conditions 145

Figure 3. Nascent OH $X\ ^2\Pi$ quantum state distribution observed following quenching of OH $A\ ^2\Sigma^+$ (v=0, N=0) by Kr as a function of OH $X\ ^2\Pi$ internal energy 147

Figure 4. Nascent OH $X\ ^2\Pi$ quantum state distribution observed following quenching of OH $A\ ^2\Sigma^+$ (v=0, N=0) by Kr as a function of rotational level, N''.....148

Figure 5. Visualization of the approach of Kr to the OH(A) π_z and OH(X) π_y HOMO orbitals 151

Figure 6. OH ($X\ ^2\Pi$, $A\ ^2\Sigma^+$) + Kr MRCISD+Q potential energy curves for the two states of A′ reflection symmetry 155

Figure 7. Surface plot relative to the OH $A\ ^2\Sigma^+$ + Kr asymptote of the $\Pi_{A'}$ and $\Sigma_{A'}$ diabatic states as a function of the OH to Kr center of mass distanceand the angle of OH with respect to Kr 161

Figure 8. MRCISD+Q diabatic coupling $V_{\Sigma\Pi}$ PES 163

CHAPTER 6 170

Figure 1. Schematic energetic diagram for CH_2I_2 photodissociation following absorption at 248 nm and 313 nm 173

Figure 2. Raw images and reconstructed total kinetic energy release profiles of I* ($^2P_{1/2}$) 181

CHAPTER 7 191

Figure 1. Velocity mapped raw image with derived total kinetic energy release and anisotropy parameter distributions for O ^{1}D products resulting from photolysis of the simplest Criegee intermediate CH_2OO at 360 nm.....195

Figure 2. CH_2OO action spectrum and total kinetic energy release distributions for O ^{1}D + H_2CO X ^{1}A′ products arising from photodissociation of CH_2OO at 308 nm, 330 nm, and 360 nm 202

APPENDIX I 206

Figure 1. Example Gaussian Doppler profile plotted as a function of Doppler shift and velocity and corresponding translational energy distribution.....209

Figure 2. Doppler profiles arising from quenching of OH A $^2\Sigma^+$ by D_2, with original data and refit using the new analysis method 211

Figure 3. Doppler profile of the H-atom products resulting from quenching of OH A $^2\Sigma^+$ by H_2, as repeated in the present study.....214

CHAPTER 1
Introduction

The hydroxyl radical is an important species in atmospheric and combustion environments,[1,2] where it is often detected by laser-induced fluorescence (LIF) on the well-characterized $A\ ^2\Sigma^+$ - $X\ ^2\Pi$ band system.[3] However, collisions of electronically excited OH $A\ ^2\Sigma^+$ with partners prevalent in these environments open up alternative nonradiative decay pathways that efficiently remove OH from the excited electronic state, resulting. As a result, the OH $A \rightarrow X$ fluorescence emission is quenched. At a practical level, the rates for collisional quenching of OH $A\ ^2\Sigma^+$ by relevant species must be taken into account in order to utilize LIF for quantitative measurements of OH concentrations under these atmospheric or combustion conditions.[4,5] At a more detailed level, one would like to know the mechanism for collisional quenching of OH $A\ ^2\Sigma^+$. Specifically, does collisional quenching occur via reactive and/or nonreactive processes? What is the branching between these processes? Can additional insights on the mechanism be inferred from the partitioning of the initial electronic energy over internal and translational degrees of freedom in the quenched products? At a fundamental level, one would like to understand the nature of the coupling between the OH $A\ ^2\Sigma^+$ and $X\ ^2\Pi$ electronic states in the presence of the collision partner that gives rise to quenching. The nonadiabatic coupling between electronic states involves a breakdown of the Born-Oppenheimer approximation (BOA) and the intrinsic assumption that nuclear motion evolves on a single adiabatic electronic potential energy surface.[6] Such nonadiabatic

processes occur in the photophysics of many molecular systems, ranging from ethylene to DNA, in both gaseous and condensed phases, and are an active area of experimental and theoretical research in chemical physics today.[7-11]

The BOA is the cornerstone for studying chemical processes through quantum mechanics. The separation of electronic and nuclear motion, made possible by neglecting the first and second derivatives of the electronic wavefunction with respect to the nuclear coordinates, allow for heavy nuclei to move on a single potential energy surface created by the much faster moving electrons. However, when potentials approach each other, the coupling between the nuclear and electronic motion becomes important and the BOA breaks down, often forming what are known as conical intersections (CI). The coupling, often called derivative or nonadiabatic coupling, is defined in terms of the change in the electronic wavefunction with respect to nuclear coordinates divided by the energy difference between the electronic states.[6] In a molecular system with N internal degrees of freedom, degeneracy between electronic states will be found in a subspace of N-2 dimensions.[12] The nuclear coordinates that linearly lift the degeneracy define a "branching space" with associated vectors known as the energy difference (or tuning) coordinate **g** and the interstate coupling coordinate **h**.[13-15] The breakdown of the BOA is ubiquitous, especially in larger systems, and allows for nonadiabatic events to take place in regions of CI.[8-11]

The collisional quenching of OH $A\,^2\Sigma^+$ by simple molecular partners, e.g. H_2, N_2, CO, CO_2, O_2, and Kr, provide a rich test bed in which to explore the underlying mechanism for quenching. In recent years, it has become possible to extend the kinetic

rate studies to dynamical measurements that examine the outcomes of quenching, including branching between reactive and nonreactive decay processes, kinetic energy release, and quantum state distributions of the products.[16-28] The experimental results exhibit similarities in the outcomes of OH $A\ ^2\Sigma^+$ quenching with several collision partners, suggesting common features about the nonadiabatic dynamics. For a few of the OH $A\ ^2\Sigma^+$ + M systems studied experimentally in this thesis, specifically M= H_2, CO, and Kr, theoretical investigations have identified regions of strong nonadiabatic coupling that facilitate the quenching process.[20,22-24,29,30]

Much attention has been focused on understanding the regions at or near points of CI. [8-11] Derivative couplings between the electronic states are very strong in the vicinity of the CI (and infinitely large at the point of CI), which enables these regions to have a profound effect on nuclear dynamics. CIs allow for population to be funneled from one electronic potential to another, opening up nonradiative decay pathways. In the chapters that follow, electronic quenching occurs via passage through regions of CI. This thesis is not intended to include an exhaustive study of the theoretical treatment of conical intersections performed by others, but is rather a focused look in at the local forces in the vicinity of CIs relevant to quenching in OH $A\ ^2\Sigma^+$ + M systems for M = H_2, CO, and Kr. A detailed theoretical study of conical intersections, including relevant mathematical formulae and more complete references on the subject, is given in several excellent review articles on this topic.[8-11]

The four-atom OH $A\ ^2\Sigma^+$ + H_2 system, with its isotopically substituted variations, has emerged as a model system for examining the nonadiabatic coupling and associated

dynamics for collisional quenching. For this system, experimental studies have been complemented by first-principles theoretical calculations of the CI regions that couple the OH ($A\,^2\Sigma^+$, $X\,^2\Pi$) + H_2 potentials, including the reactive channel to H + H_2O products, as well as dynamical calculations of the outcomes.[20,21,29-35] Figure 1 illustrates the minimum energy path from the OH $A\,^2\Sigma^+$ + H_2 asymptote with the O-side of OH pointing toward H_2 to a CI in the HO-H_2 configuration.[29] Two pathways then emerge from the intersection, leading to OH $X\,^2\Pi$ + H_2 products (nonreactive quenching) and H + H_2O products (reactive quenching). This one-dimensional picture highlights key features of OH quenching by several partners: restricted access from the OH $A\,^2\Sigma^+$ + M asymptote to the downhill path leading to the CI region, branching in the CI region to multiple product channels, and evolution to OH $X\,^2\Pi$ + M and other reaction products.

The final two chapters of this thesis focus on photodissociation, another excited state population removal process, where photoexcitation causes chemical bond fission and new products to form through a collisionless process. Some of the same questions can be asked here: What products are formed from photodissociation? What is the branching between different product channels? Can additional insights on the dissociation dynamics be inferred from the partitioning of the available energy over internal and translational degrees of freedom in the new products? The linkage of experimental observables to available theoretical studies could provide new information regarding the photodissociation dynamics.

In a simple photodissociation of molecule AB, where AB + $h\nu \rightarrow$ A + B, two fragments are produced which move with equal momentum in opposite directions. In an

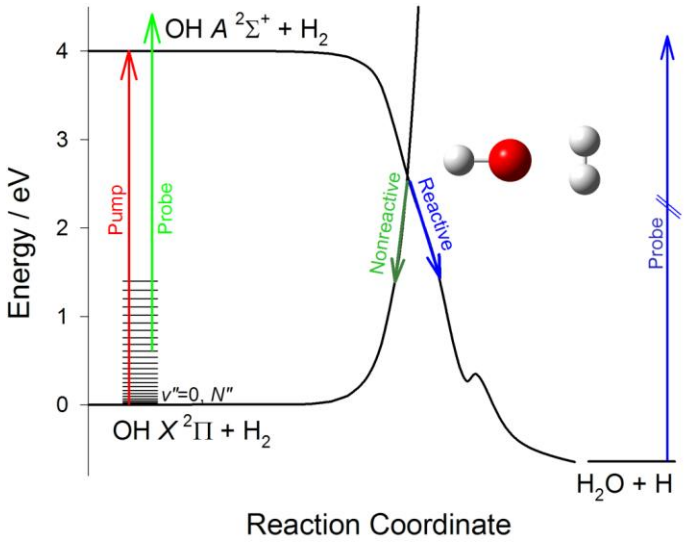

Figure 1. Simplified reaction coordinate for quenching of OH $A\ ^2\Sigma^+$ by H_2 [adapted from Ref. 29] via the C_{2v} HO-H_2 conical intersection [from Ref. 30]. Both nonreactive quenching producing OH $X\ ^2\Pi$ + H_2 and reactive quenching to H_2O + H are illustrated. The pump excitation that prepares OH $A\ ^2\Sigma^+$ (v'=0, N'=0) and probe schemes utilized for LIF detection of the quenched OH $X\ ^2\Pi$ and H-atom products are indicated.

ideal coincidence experiment, one would want to measure the speed and angular direction of each fragment from a single dissociation event, with a simultaneous measurement of the internal energy of both fragments corresponding to those velocities.[36] As many randomly oriented AB molecules dissociate from a point source, a sphere of fragments is formed, known as a Newton sphere, with a radius proportional to that fragment's speed. Velocity map ion imaging (VMI) is a very useful experimental technique to measure velocity (speed and angular information) of one fragment and thereby reflect the internal energy distribution of the cofragment.[37,38] For the ease of discussion, fragment A will be labeled as the imaged fragment and fragment B is the (nonimaged) cofragment. In VMI, the full three-dimensional Newtown sphere of the recoiling fragment A is projected onto a two-dimensional imaging plane.[36] Methods can be used to reconstruct the image into the original 3D Newton sphere,[39-41] at which point the kinetic energy release (KER) to fragment A as well as its angular distribution can be derived. The total kinetic energy release (TKER) to the products during photodissociation results from the conservation of momentum. Further information can be derived using the conservation of energy:

$$E_{avl} = E_{h\nu} - D_0 = TKER + E_A + E_B$$

where E_{avl} is the available energy, $E_{h\nu}$ is the photon energy, D_0 is the dissociation energy, and E_A and E_B are the internal energies of fragments A and B, respectively. There have been numerous recent advances regarding the experiment apparatus design and application of VMI to various systems, many of which are reviewed in detail in a book edited by Whitaker.[36] Often, VMI is used in conjunction with state-selective ionization techniques, such as resonance-enhanced multiphoton ionization (REMPI). This allows

the internal energy of A to be selected experimentally, becoming a known quantity, and thus the measured TKER distribution is directly related to the internal energy distribution of B (as long as D_0 is also known).

Additional information can be derived from the reconstructed Newton sphere, specifically the angular distribution of fragment A. Note that the angular distribution of fragment A will be the same as the angular distribution of fragment B if B were the imaged fragment. This is because the angular distribution is a reflection of the dissociation process and not dependent on which particle is imaged. The angular distribution, $I(\theta)$, is defined as $I(\theta) = 1 + \beta P_2(\cos\theta)$, where θ is the angle between the recoil direction and the polarization axis of the photolysis laser, P_2 is the second-order Legendre polynomial, and β is the anisotropy parameter. [42] The anisotropy parameter can range from -1 for a pure perpendicular transition to +2 for a pure parallel transition with the assumption of the rapid dissociation process compared to the rotational period of the diatomic molecule.

A newly built VMI apparatus is used to study the photodissociation of diiodomethane (CH_2I_2) and the simplest Criegee intermediate, CH_2OO. The photodissociation of CH_2I_2 produces iodine atoms which play a significant role in tropospheric ozone depletion reactions.[43] The dissociation is also of fundamental interest due to its complicated excited state spectroscopy[44] and photodissociation dynamics, primarily leading to $CH_2I + I(^2P_{3/2})/I^*(^2P_{1/2})$.[45-49] By characterizing the TKER distributions through imaging the I* fragment, reflecting the internal energy of the CH_2I cofragment, insight can be gained into the dissociation dynamics at 248 nm. CH_2I_2

photodissociation at 248 nm is also of renewed interest due to its recent use in a laboratory synthetic route to generate CH_2OO, the simplest Criegee intermediate, through a near thermoneutral reaction of CH_2I with O_2.[50,51] Thus, mapping out the internal energy of the CH_2I fragment gives additional information regarding the initial internal energy of CH_2OO.

Criegee intermediates are a class of important atmospheric intermediates generated from the ozonolysis of alkenes in the troposphere,[52] which until very recently could only be probed through indirect methods.[50,53] Alkenes from biogenetic or anthropogenic sources are an important tropospheric species. The major removal process of these unsaturated hydrocarbons is through reaction with ozone.[2,43,54] Criegee intermediates could be produced in the troposphere with a significant degree of internal excitation due to the large exothermicity of the ozonolysis process.[52,55,56] Atmospheric removal processes of the energized Criegee intermediates include bimolecular reactions, unimolecular reactions or isomerizations, or collisional relaxation. It was recently proposed that solar photolysis in the UV-A wavelength region of the simplest Criegee is an additional removal process.[57] The broad, unstructured *B*-*X* absorption spectrum of CH_2OO is consistent with the calculated repulsive nature of the *B*-state along the CH_2O-O coordinate. Solar photolysis in the UV-A wavelength region results in O ^{1}D generation, which is investigated in the brief final chapter of this thesis.

Chapter 2 is a joint experimental and theoretical study of outcomes resulting from the nonreactive quenching of electronically excited OD $A\ ^2\Sigma^+$ by H_2. The experiments utilize a pump-probe technique to detect the OD $X\ ^2\Pi$ product state

distribution under single collision conditions. The OD $X\ ^2\Pi$ products are observed primarily in their lowest vibrational state ($v''=0$) with substantially less population in $v''=1$. The OD $X\ ^2\Pi$ products are generated with a high degree of rotational excitation, peaking at $N''=21$ with an average rotational energy of 4600 cm^{-1}, and a strong propensity for populating the $\Pi(A')$ Λ-doublet component indicative of alignment of the half-filled $p\pi$ orbital in the plane of OD rotation. Branching fraction measurements show that the nonreactive channel accounts for less than 20% of quenching outcomes. Complementary classical trajectory calculations of the post-quenching dynamics are initiated from representative points along seams of conical intersections between the ground and excited-state potentials of OD ($A\ ^2\Sigma^+$, $X\ ^2\Pi$) + H_2. Diabatic modeling of the initial momenta in the dynamical calculations captures the key experimental trends: OD $X\ ^2\Pi$ products released primarily in their ground vibrational state with extensive rotational excitation and a branching ratio that strongly favors reactive quenching. The OD $A\ ^2\Sigma^+$ + H_2 results are also compared with previous studies on the quenching of OH $A\ ^2\Sigma^+$ + H_2; the two experimental studies show remarkably similar rotational energy distributions for the OH and OD $X\ ^2\Pi$ radical products.

Chapter 3 extends **Chapter 2** by probing the H- and D-atom products from reactive quenching of OD $A\ ^2\Sigma^+$ by H_2 via Doppler spectroscopy using two-photon ($2\ ^2S \leftarrow\leftarrow 1\ ^2S$) laser-induced fluorescence. Partial deuteration enables separation of the channel forming H + HOD products, which accounts for 75% of reactive quenching events, from the D + H_2O product channel. The Doppler profiles, along with those reported previously for other isotopic variants, are transformed into product translational

energy distributions using a robust fitting procedure based on discrete velocity basis functions, which is discussed in **Appendix I**. The product translational energy distribution for the H-atom channel is strongly peaked at low energy (below 0.5 eV) with a long tail extending to the energetic limit. By contrast, the D-atom channel exhibits a small peak at low translational energy with a distinctive secondary peak at higher translational energy (approximately 1.8 eV) before falling off to higher energy. In both cases, most of the available energy flows into internal excitation of the water products. Similar distributions are obtained upon reanalysis of D- and H-atom Doppler profiles, respectively, from reactive quenching of OH $A\ ^2\Sigma^+$ by D_2. The sum of the translational energy distributions for H- and D-atom channels is remarkably similar to that obtained for OH $A\ ^2\Sigma^+ + H_2$, where the two channels cannot be distinguished from one another. The product translational energy distributions from reactive quenching are compared with those obtained from a previous experiment performed at higher collision energy, quasiclassical trajectory calculations of the post-quenching dynamics, and a statistical model.

Chapter 4 examines the outcomes following collisional quenching of electronically excited OH $A\ ^2\Sigma^+$ by O_2 and CO in a combined experimental and theoretical study. The atomic products from reactive quenching are probed using two-photon laser-induced fluorescence to obtain H-atom Doppler profiles, O (^3P_J) atom fine structure distributions, and the relative yields of these products with H_2, O_2, and CO collision partners. The corresponding H-atom translational energy distributions are extracted for the $H + O_3$ and $H + CO_2$ product channels, in the latter case revealing that

most of the available energy is funneled into internal excitation of CO_2. The experimental product branching ratios show that the O-atom producing pathways are the dominant outcomes of quenching: the OH $A\ ^2\Sigma^+ + O_2 \rightarrow O + HO_2$ channel accounts for 48(3)% of products and the OH $A\ ^2\Sigma^+ + CO \rightarrow O + HCO$ channel yields 76(5)% of products. In addition, quenching of OH $A\ ^2\Sigma^+$ by O_2 generates $H + O_3$ products [12(3)%] and returns OH to its ground $X\ ^2\Pi$ electronic state [40(1)%; Ref. 19]. Quenching of OH $A\ ^2\Sigma^+$ by CO also yields $H + CO_2$ reaction products [26(5)%]; however, OH $X\ ^2\Pi$ ($v'' = 0,1$) products from nonreactive quenching are not observed. Theoretical studies characterize the properties of energy minimized conical intersections in four regions of strong nonadiabatic coupling accessible from the OH $A\ ^2\Sigma^+ + CO$ asymptote. Three of these regions have the O-side of OH pointing toward CO, which lead to atomic H and CO_2 products and/or nonreactive quenching. In the fourth region, energy minimized points are located on a seam of conical intersection from the OH $A\ ^2\Sigma^+ + CO$ asymptote to a conical intersection with an extended OH bond length and the H-side of OH pointing towards CO in a bent configuration. This region, exoergic with respect to the reaction asymptote, is likely to be the origin of the dominant O + HCO product channel.

Electronic quenching of OH $A\ ^2\Sigma^+$ by Kr is investigated in **Chapter 5** through experimental studies of the collision cross sections and the OH $X\ ^2\Pi$ product distribution. The quenching cross sections decrease with increasing rotational excitation in the excited OH $A\ ^2\Sigma^+$ electronic state. The OH $X\ ^2\Pi$ products of quenching exhibit a significant degree of rotational excitation, but minimal vibrational excitation. Complementary theoretical studies of the OH ($A\ ^2\Sigma^+$, $X\ ^2\Pi$) + Kr potential energy surfaces, nonadiabatic

coupling, and quasi-classical trajectory calculations are carried out to elucidate the quenching dynamics. Theoretically, the potential energy surfaces (PESs) for the two lowest diabatic states of A′ symmetry are computed along with the angularly dependent coupling between them. Coupling in near linear HO–Kr configurations provides the mechanism for the observed electronic quenching. A deep attractive well on the OH $A\ ^2\Sigma^+$ – Kr PES facilitates access to this region of strong coupling. Surface-hopping quasi-classical trajectory calculations yield quenching cross sections and OH $X\ ^2\Pi$ product rotational distribution in good accord with experimental observations.

In **Chapter 6**, the UV photodissociation of CH_2I_2 resulting in $CH_2I + I^*(^2P_{1/2})$ is investigated using a newly constructed velocity map ion imaging apparatus. A two-color experiment is used to examine photodissociation following absorption at 248 nm, resulting in $\langle E_T \rangle$=2080 cm^{-1}. This corresponds to only 14% of the available energy; the remaining 86% is channeled into the internal excitation of the CH_2I cofragment, where $\langle E_{int} \rangle$ = 12,710 cm^{-1} (36.3 kcal mol^{-1}), which is also predicted by a simple impulsive model. The dominant TKER feature has an anisotropy parameter of β=0.81, indicating a prompt dissociation process, but does not directly correlate to the predicted electronic character (B_2 and/or A_1) of the absorption band. The implication of the large degree of CH_2I internal excitation on the synthetic generation of the simplest Criegee intermediate, CH_2OO, is discussed. A one-color experiment which probes the dissociative adiabatic outcome following CH_2I_2 absorption to the $2B_1$ state near 313 nm is discussed in **Appendix II**.

Chapter 7 reports O ^{1}D generation following UV photodissociation of the simplest Criegee intermediate, CH_2OO. The O ^{1}D formation was monitored using 2+1 REMPI in combination with velocity map ion imaging. The O ^{1}D formed from photodissociation tracks with the CH_2OO $B\ ^1A' \leftarrow X\ ^1A'$ UV absorption spectrum previously measured in our laboratory.[57] From the spatial information derived from the velocity mapped image, the anisotropic angular distribution reflects the $\pi^* \leftarrow \pi$ character of the CH_2OO *B*-*X* electronic excitation. By changing the photodissociation wavelength and monitoring the kinetic energy release, an experimental upper limit of 53(1) kcal/mol dissociation energy to O ^{1}D + H_2CO $X\ ^1A_1$ was derived and compared with recent *ab intio* calculations. The generation of O ^{1}D from solar photolysis of CH_2OO can react with H_2O in the troposphere, forming secondary OH radicals.

References

1 I. Glassman and R. Yetter, *Combustion, Fourth Edition*. (Academic Press, Boston, 2008).
2 R. P. Wayne, *Chemistry of Atmospheres, Third Edition*. (Oxford University Press, Oxford, 2000).
3 J. Luque and D. R. Crosley, SRI International Report MP 99-009 (1999).
4 R. A. Copeland and D. R. Crosley, J. Chem. Phys. **84** (6), 3099 (1986).
5 D. E. Heard and D. A. Henderson, Phys. Chem. Chem. Phys. **2** (1), 67 (2000).
6 B. Retail and A. J. Orr-Ewing, in *Tutorials in Molecular Reaction Dynamics*, edited by M. Brouard and C. Vallance (Royal Society of Chemistry, Cambridge, 2010).
7 F. F. Crim, Faraday Discuss. **157**, 9 (2012).
8 W. Domcke and D. R. Yarkony, Annu. Rev. Phys. Chem. **63**, 325 (2012).
9 B. G. Levine and T. J. Martinez, Annu. Rev. Phys. Chem. **58**, 613 (2007).
10 S. Matsika and P. Krause, Annu. Rev. Phys. Chem. **62**, 621 (2011).
11 G. A. Worth and L. S. Cederbaum, Annu. Rev. Phys. Chem. **55**, 127 (2004).
12 J. von Neumann and E. Wigner, Physikalische Zeitschrift **30**, 467 (1929).
13 H. Koppel, W. Domcke, and L. S. Cederbaum, Adv. Chem. Phys. **57**, 59 (1984).
14 M. R. Manaa and D. R. Yarkony, J. Am. Chem. Soc. **116** (25), 11444 (1994).
15 D. R. Yarkony, J. Chem. Phys. **114** (6), 2601 (2001).

[16] I. B. Pollack, Y. X. Lei, T. A. Stephenson, and M. I. Lester, Chem. Phys. Lett. **421** (4-6), 324 (2006).
[17] L. P. Dempsey, C. Murray, and M. I. Lester, J. Chem. Phys. **127**, 151101 (2007).
[18] L. P. Dempsey, C. Murray, P. A. Cleary, and M. I. Lester, Phys. Chem. Chem. Phys. **10** (10), 1424 (2008).
[19] L. P. Dempsey, T. D. Sechler, C. Murray, and M. I. Lester, J. Phys. Chem. A **113** (25), 6851 (2009).
[20] P. A. Cleary, L. P. Dempsey, C. Murray, M. I. Lester, J. Kłos, and M. H. Alexander, J. Chem. Phys. **126** (20), 204316 (2007).
[21] J. H. Lehman, L. P. Dempsey, M. I. Lester, B. Fu, E. Kamarchik, and J. M. Bowman, J. Chem. Phys. **133** (16), 164307 (2010).
[22] L. P. Dempsey, T. D. Sechler, C. Murray, M. I. Lester, and S. Matsika, J. Chem. Phys. **130** (10), 104307 (2009).
[23] J. H. Lehman, M. I. Lester, J. Kłos, M. H. Alexander, P. J. Dagdigian, D. Herráez-Aguilar, F. J. Aoiz, M. Brouard, H. Chadwick, T. Perkins, and S. A. Seamonse, J. Phys. Chem. A, Submitted (2013).
[24] J. H. Lehman, M. I. Lester, and D. R. Yarkony, J. Chem. Phys. **137** (9), 094312 (2012).
[25] D. T. Anderson, M. W. Todd, and M. I. Lester, J. Chem. Phys. **110** (23), 11117 (1999).
[26] M. W. Todd, D. T. Anderson, and M. I. Lester, J. Phys. Chem. A **105**, 10031 (2001).
[27] J. H. Lehman, J. L. Bertrand, T. A. Stephenson, and M. I. Lester, J. Chem. Phys. **135** (14), 144303 (2011).
[28] M. Ortiz-Suárez, M. F. Witinski, and H. F. Davis, J. Chem. Phys. **124** (20), 201106 (2006).
[29] M. I. Lester, R. A. Loomis, R. L. Schwartz, and S. P. Walch, J. Phys. Chem. A **101** (49), 9195 (1997).
[30] B. C. Hoffman and D. R. Yarkony, J. Chem. Phys. **113** (22), 10091 (2000).
[31] E. Kamarchik, B. N. Fu, and J. M. Bowman, J. Chem. Phys. **132** (9), 091102 (2010).
[32] B. Fu, E. Kamarchik, and J. M. Bowman, J. Chem. Phys. **133** (16), 164306 (2010).
[33] P. Y. Zhang, R. F. Lu, T. S. Chu, and K. L. Han, J. Phys. Chem. A **114** (24), 6565 (2010).
[34] P. Y. Zhang, R. F. Lu, T. S. Chu, and K. L. Han, J. Chem. Phys. **133** (17), 174316 (2010).
[35] M. A. Collins, O. Godsi, S. Liu, and D. H. Zhang, J. Chem. Phys. **135**, 234307 (2011).
[36] B. J. Whitaker, *Imaging in Molecular Dynamics Technology and Applications*. (Cambridge University Press, 2003).
[37] P. L. Houston, J. Phys. Chem. **100** (31), 12757 (1996).
[38] A. T. J. B. Eppink and D. H. Parker, Rev. Sci. Instrum. **68** (9), 3477 (1997).

[39] V. Dribinski, A. Ossadtchi, V. A. Mandelshtam, and H. Reisler, Rev. Sci. Instrum. **73** (7), 2634 (2002).
[40] G. A. Garcia, L. Nahon, and I. Powis, Rev. Sci. Instrum. **75** (11), 4989 (2004).
[41] G. M. Roberts, J. L. Nixon, J. Lecointre, E. Wrede, and J. R. R. Verlet, Rev. Sci. Instrum. **80** (5) (2009).
[42] R. N. Zare and D. R. Herschbach, Proceedings of the IEEE **51** (1), 173 (1963).
[43] B. J. Finlayson-Pitts and J. N. Pitts, *Chemistry of the Upper and Lower Atmosphere*. (Academic Press, San Diego, 2000).
[44] M. Ito, P. C. Huang, and E. M. Kosower, Transactions of the Faraday Society **57** (10), 1662 (1961).
[45] S. L. Baughcum and S. R. Leone, J. Chem. Phys. **72** (12), 6531 (1980).
[46] K. W. Jung, T. S. Ahmadi, and M. A. El-Sayed, Bull. Korean Chem. Soc. **18** (12), 1274 (1997).
[47] M. Kawasaki, S. J. Lee, and R. Bersohn, J. Chem. Phys. **63** (2), 809 (1975).
[48] J. B. Koffend and S. R. Leone, Chem. Phys. Lett. **81** (1), 136 (1981).
[49] H. F. Xu, Y. Guo, S. L. Liu, X. X. Ma, D. X. Dai, and G. H. Sha, J. Chem. Phys. **117** (12), 5722 (2002).
[50] C. A. Taatjes, G. Meloni, T. M. Selby, A. J. Trevitt, D. L. Osborn, C. J. Percival, and D. E. Shallcross, J. Am. Chem. Soc. **130** (36), 11883 (2008).
[51] E. P. F. Lee, D. K. W. Mok, D. E. Shallcross, C. J. Percival, D. L. Osborn, C. A. Taatjes, and J. M. Dyke, Chemistry – A European Journal **18** (39), 12411 (2012).
[52] R. Criegee, Angewandte Chemie International Edition in English **14** (11), 745 (1975).
[53] O. Welz, J. D. Savee, D. L. Osborn, S. S. Vasu, C. J. Percival, D. E. Shallcross, and C. A. Taatjes, Science **335** (6065), 204 (2012).
[54] J. H. Seinfeld and S. N. Pandis, *Atmospheric Chemistry and Physics - From Air Pollution to Climate Change*, 2nd ed. (John Wiley & Sons., New York, 2006).
[55] J. G. Calvert, R. Atkinson, J. A. Kerr, S. Madronich, G. K. Moortgat, T. J. Wallington, and G. Yarwood, *The Mechanisms of Atmospheric Oxidation of the Alkenes* (Oxford University Press, Oxford, 2000).
[56] O. Horie and G. K. Moortgat, Acc. Chem. Res. **31** (7), 387 (1998).
[57] J. M. Beames, F. Liu, L. Lu, and M. I. Lester, J. Am. Chem. Soc. **134** (49), 20045 (2012).

CHAPTER 2
Collisional quenching of OD $A\ ^2\Sigma^+$ by H_2: Experimental and theoretical studies of the state-resolved OD $X\ ^2\Pi$ product distribution and branching fraction

The experimental research presented in this chapter was performed at the University of Pennsylvania and the theoretical calculations were performed at Emerson University. This research has been published as a paper in the *Journal of Chemical Physics*.

Reference: J. H. Lehman, L. P. Dempsey, M. I. Lester, B. Fu, E. Kamarchik, and J. M. Bowman, *J. Chem. Phys.*, **133**, 164307 (2010).

I. Introduction

Hydroxyl radicals play a central role in atmospheric and combustion environments where their abundance is often monitored by laser-induced fluorescence (LIF) on the *A*-*X* band system.[1] Collisions of OH $A\ ^2\Sigma^+$ with molecular partners present in these environments open nonradiative decay pathways that efficiently remove population from the excited OH $A\ ^2\Sigma^+$ electronic state. This results in reduced fluorescence lifetimes and quantum yields. To account for these effects, quenching cross sections for OH $A\ ^2\Sigma^+$ have been evaluated over a wide range of temperatures and initial OH $A\ ^2\Sigma^+$ rotational levels for many collision partners.[2-5] In general, quenching cross sections decrease with increasing temperature, indicating that attractive forces govern the kinetics. Furthermore, the cross sections decrease with increasing OH $A\ ^2\Sigma^+$ rotational level, suggesting that only certain orientations of OH $A\ ^2\Sigma^+$ with its collision partner lead to quenching. Prior kinetic studies have shown that isotopic substitution of OD for OH does not affect the overall rate of quenching under thermal conditions.[2,3,6,7]

A number of different empirical models have been proposed to predict the rates for collisional quenching based on the kinetics measurements,[3,8-11] yet the underlying mechanism has remained elusive. Recent experiments have begun to examine the outcomes of collisional quenching of OH $A\ ^2\Sigma^+$ and are starting to provide new insight on the mechanism.[12-20] Collisional removal of OH from the excited $A\ ^2\Sigma^+$ state can occur by reactive quenching, leading to formation of new products, or nonreactive quenching that returns population to the ground or low-lying electronic state(s). Quenching of OH $A\ ^2\Sigma^+$ by H_2 has emerged as a benchmark system since experimental studies have been

complemented by first-principles theoretical calculations of the conical intersection (CoI) regions that couple the OH ($A\ ^2\Sigma^+$, $X\ ^2\Pi$) + H_2 potential energy surfaces[16,21-24] as well as dynamical calculations of the outcomes.[25,26] In the present study, we extend the experimental and theoretical investigation of outcomes of quenching to the deuterated OD $A\ ^2\Sigma^+ + H_2$ system.

A brief summary of previous work is given below. Collisional quenching of OH $A\ ^2\Sigma^+$ by H_2 can proceed via a nonreactive pathway, returning OH to the ground $X\ ^2\Pi$ state + H_2 ($\Delta E = -4.02$ eV), or a reactive pathway producing H + H_2O ($\Delta E = -4.66$ eV). Studies of the OH $X\ ^2\Pi$ product state distribution following nonreactive quenching reveal that the OH products are released primarily in the lowest vibrational level, $v''=0$, with decreasing population in higher vibrational levels. By contrast, the OH $X\ ^2\Pi$ products exhibit a remarkable degree of rotational excitation, peaking at $N''=15$ in $v''=0$. Branching fraction measurements reveal that the nonreactive pathway is a minor channel, comprising only $12 \pm 5\%$ of quenching events.[17] Reactive quenching is the dominant pathway for OH $A\ ^2\Sigma^+ + H_2$. The translational energy release of the H atom products shows that most of the available energy is channeled into internal excitation of the H_2O product.[12] Similar results are obtained for the D-atom products from the OH $A\ ^2\Sigma^+ + D_2 \rightarrow$ HOD + D abstraction channel, although H-atom products from a D_2O + H insertion channel are also observed.[13] Crossed molecular beam scattering experiments later showed the D-atom products to be mostly forward scattered, indicating a direct reaction mechanism.[14]

Theoretical calculations of the OH ($A\ ^2\Sigma^+$, $X\ ^2\Pi$) + H_2 potentials indicate a barrierless path to the CoI when the oxygen side of OH points towards H_2.[16,21-24] By contrast, reversing the orientation of OH $A\ ^2\Sigma^+$, such that the hydrogen side of OH points towards H_2, results in an attractive electrostatic interaction, but does not lead to a CoI.[16,21,27] Further calculations mapping the OH ($A\ ^2\Sigma^+$, $X\ ^2\Pi$) + H_2 potentials as a function of OH orientation and distance between the OH + H_2 moieties reveal steep angular gradients leading toward and, more strongly away, from the CoI region.[16] The high degree of rotational excitation of the OH $X\ ^2\Pi$ products is attributed to these angular gradients generating a large torque on the OH moiety as it passes through the CoI region. Finally, the OH $X\ ^2\Pi$ product vibrational distribution confirms theoretical predictions that indicate little change in the OH bond length as the system evolves through the CoI.[24]

A recent classical trajectory study by Bowman and coworkers has begun to explore the outcomes of collisional quenching of OH $A\ ^2\Sigma^+$ by H_2 by examining the post-quenching dynamics initiated at various points along the seams of conical intersections.[25] Their calculated electronic energies of the $1^2A'$ and $2^2A'$ states as a function of separation distance between the OH and H_2 moieties in a C_{2v} configuration, obtained using the MRCI method with the correlation-consistent augmented triple zeta (aVTZ) basis set, are illustrated in Fig. 1 (and adapted for OD + H_2). The OH $X\ ^2\Pi$ products of nonreactive quenching are predicted to have a substantial degree of rotational excitation and little vibrational excitation, in good agreement with experimental results. The predicted translational energy distribution following reactive quenching also corroborates experimental results, showing that much of the available energy is channeled into internal

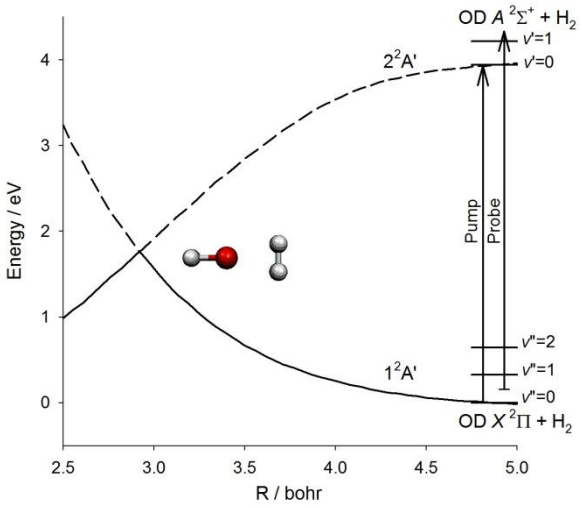

Figure 1. Schematic diagram of the 2*A*′ and 1*A*′ potentials for OD ($A\ ^2\Sigma^+$, $X\ ^2\Pi$) + H_2 as a function of separation distance (R) between OD and H_2, defined as O to H_2 center-of-mass distance, in the C_{2v} configuration. The potentials are adapted from Ref. 25. The arrows depict the experimental pump-probe scheme used to examine the outcomes of collisional quenching. The pump laser prepares electronically excited OD $A\ ^2\Sigma^+$ (v'=0, N'=0) radicals through excitation on the $P_1(1)$ line of the *A*-*X* (0,0) transition, which are subsequently quenched in collisions with H_2. The OD $X\ ^2\Pi$ (v''=0, 1) products of nonreactive quenching are detected on *A*-*X* (1,0) or (1,1) transitions via laser-induced fluorescence (LIF).

excitation of the water product. On the other hand, the branching fraction between reactive and nonreactive quenching pathways is dependent on the momenta sampling method utilized, with diabatic sampling yielding good agreement with experiment. Efforts toward a rigorous, fully coupled quantum dynamics study on the benchmark OH $A\ ^2\Sigma^+ + H_2$ system are being pursued by the Bowman group and others.[28] Very recently, a short report of such a calculation has appeared, and the calculated OH $X\ ^2\Pi$ rovibrational distributions are in good agreement with experimental and classical ones described above.[26]

In the present experiments, collisional quenching of OD radicals in the excited $A\ ^2\Sigma^+$ state by H_2 is examined to obtain a comprehensive OD $X\ ^2\Pi$ product state distribution as well as the branching fraction to the nonreactive quenching channel. Varying the isotopic composition of the collision partners, e.g. from OH to OD or H_2 to D_2, changes the nuclear motions and reduced mass of the system, yet the electronic potential energy surfaces that control quenching are unchanged. For OD $A\ ^2\Sigma^+ + H_2$, in particular, the OD products of nonreactive quenching are mapped onto a completely different grid of rovibrational quantum states than earlier studies of OH quenching. These experimental results are compared with analogous results obtained previously for quenching of OH $A\ ^2\Sigma^+$ by H_2 and D_2, and also discussed in the context of complementary trajectory studies of the quenching dynamics in these systems.

II. Experimental Methods

The experimental method for determining the OD $X\ ^2\Pi$ product state distribution and branching fraction following collisional quenching of OD $A\ ^2\Sigma^+$ is analogous to that used previously for OH quenching studies.[16,18,19] For these experiments, OD radicals are generated in the throat of a pulsed supersonic expansion by 193 nm (Lambda Physik COMPex 102) photolysis of DNO_3 (98 atom % D, 90 wt % in D_2O) entrained in 30% H_2/He carrier gas. A UV pump laser beam (1 mJ/pulse, 3 mm diameter) excites OD radicals on the $P_1(1)$ line of the OD *A*-*X* (0,0) transition at 32529 cm^{-1} in the collisional region of the expansion at a distance $x/D = 5$ in nozzle diameters *D*, where the temperature is approximately 50 K. After a 100 ns delay, a second counter-propagating and spatially overlapped UV probe laser beam (1 mJ/pulse, 3 mm diameter) intersects the expansion and probes the OD $X\ ^2\Pi$ products of nonreactive quenching on various OD *A*-*X* transitions with vibrational (v''), rotational (N''), and fine-structure resolution. The experimental pump-probe scheme is illustrated in Fig. 1.

Probe LIF signals are collected using a photomultiplier tube (PMT, EMI 9183Q) under saturated LIF conditions, processed with a digital storage oscilloscope (LeCroy WaveRunner 6050A) and transferred to a laboratory computer for further analysis. The waveform traces are fit to single exponential decays to determine fluorescence lifetimes. Waveform traces are also integrated (1μs gate) to obtain intensities, which are scaled relative to a reference line and converted to relative OD $X\ ^2\Pi$ populations using the same analysis procedure that has been described previously.[16,29] The analysis procedure accounts for the lifetime and fluorescence quantum yield (Φ_f) of the emitting state as well

as the filter transmission function. The challenge in these experiments is to measure the small LIF signals arising from probing OD $X\,^2\Pi$ products of nonreactive quenching while discriminating against the intense pump LIF signal.

Three different laser excitation and fluorescence detection schemes are utilized to probe the OD $X\,^2\Pi$ (v''=0, 1, N'') products. Various bandpass filters (10 nm breadth) and additional longpass, shortpass, or notch filters are used to collect the probe laser-induced fluorescence selectively. Products in OD $X\,^2\Pi$ (v''=1) are detected by probe laser excitation on the $A\leftarrow X$ (1,1) band at ~320 nm and collection of $A\rightarrow X$ (1,0) emission at ~290 nm. Two different probe schemes are used for detection of OD $X\,^2\Pi$ (v''=0, N'') products. The OD products in high N'', specifically $N''\geq 23$, are probed on the $A\leftarrow X$ (1,0) band at ~298 nm and fluorescence is collected on the $A\rightarrow X$ (1,1) band at ~322 nm. The OD products in low N'', specifically $N''\leq 25$, are probed on the $A\leftarrow X$ (1,0) band at ~292 nm and fluorescence is collected from the same band. In this case, the probe laser excites on P- or Q-branch lines and the resulting fluorescence is detected primarily on R- and Q-branch lines of the same band. A limited range of OD $X\,^2\Pi$ (v''=0, N'') levels, N''=23-25, could be detected with both schemes.

The experimental method for determining the branching fraction consists of measuring the relative intensities of the very intense pump LIF signal and the much weaker probe LIF signals for selected product states.[17] Different filter combinations and PMT detector gain settings are required to collect emission on the OD $A\rightarrow X$ (0, 1) transition induced by pump laser excitation and probe LIF signals on the transitions detailed above.

III. Theoretical Methods

The methods used in the present calculation of the OD product distribution and branching ratio are identical to those described in a recent Communication.[25] (A full paper describing additional calculations, in particular the H_2O product internal state distributions, and also giving details of the excited potential will be published.[30]) In brief, roughly 200 000 trajectories were run from thirteen previously identified conical intersections,[24] with microcanonical initial conditions using a "diabatic" filter of momenta which assumes direct passage through the CoIs from the excited to the ground state potential. As noted above this set of initial conditions resulted in a nonreactive to reactive product branching ratio of 1 to 8 for quenching of OH $A\ ^2\Sigma^+$ by H_2, in good agreement with experiment and so we used this sampling here. Animations of representative trajectories leading to nonreactive quenching (Fig. S1) and reactive quenching via abstraction (Fig. S2) and insertion (Fig. S3) processes are included in the online supplementary material.[31] Standard quasiclassical assignment of rovibrational states of the OD (and H_2) products was done, as described elsewhere.[25]

IV. Results

A. OD $A\ ^2\Sigma^+$ Lifetimes

The OD radicals prepared in the lowest rovibrational level (v'=0, N'=0) of the excited $A\ ^2\Sigma^+$ electronic state have a fluorescence lifetime of 145(5) ns under the current experimental conditions, which is significantly shorter than the radiative lifetime of ~700 ns.[32] The resultant collisional decay rate, 5.5(3) x 10^{-3} ns^{-1}, and fluorescence quantum

yield, $\Phi_f \sim 0.21(3)$, indicate that collisions with H_2 in the 30% H_2/He carrier gas are efficient in quenching OD $A\ ^2\Sigma^+$ (v'=0, N'=0); pure He carrier gas does not quench the fluorescence. The fluorescence lifetimes are also measured for each of the OD $A\ ^2\Sigma^+$ (v'=1, N') states accessed by the probe laser. These lifetimes increase from 260 ns at N'=9 to about 470 ns for $N' \geq 19$. Taking into account the tabulated radiative lifetimes for OD $A\ ^2\Sigma^+$ (v'=1, N') from LIFBase,[32] which are nearly constant over the range of levels probed, we can extract the collisional decay rates under typical experimental conditions. This yields pseudo-first-order collisional decay rates for OD $A\ ^2\Sigma^+$ (v'=1, N') decreasing from 2.5 x 10^{-3} ns^{-1} at N'=9 to 1.1 x 10^{-3} ns^{-1} at N'=19, where it reaches a plateau, a trend that is consistent with previous studies of quenching rates under thermal conditions.[3]

For OD $A\ ^2\Sigma^+$ (v'=0, N'=0) + H_2, the collisional decay arises exclusively from quenching. For OD $A\ ^2\Sigma^+$ (v'=1) + H_2, the collisional decay may include contributions from both quenching and vibrational energy transfer (VET). These two processes are assumed to contribute nearly equally based on prior kinetics studies under thermal conditions.[2] With the further assumption that the rate of VET from v'=1 to v'=0 is approximately equal to that of quenching from v'=0, again based on earlier kinetic studies,[33] a simple kinetic model shows that no population will build up in OD $A\ ^2\Sigma^+$ (v'=0). Thus, we analyze the data assuming that the probe laser induced emission originates solely from OD $A\ ^2\Sigma^+$ (v'=1), as validated in previous studies by dispersed fluorescence measurements.[34]

B. OD $X\ ^2\Pi$ Product State Distribution

1. Experimental Results

The OD $X\ ^2\Pi$ product state distribution (PSD) following nonreactive quenching of OD $A\ ^2\Sigma^+$ by H_2 has been measured under single collision conditions. This is evident from the rate of collisional quenching for the initially prepared OD $A\ ^2\Sigma^+$ (v'=0, N'=0) state. Within the 100 ns delay between the pump and probe laser beams, less than one quenching collision occurs on average. As an additional check, the delay between the pump and probe laser beams was doubled to 200 ns, and relative populations in select OD $X\ ^2\Pi$ product states were measured. The relative population distribution showed no change indicating that secondary collisions had not redistributed population. No evidence was found for OH $X\ ^2\Pi$ (v''=0) products arising from an exchange reaction by surveying several rotational states.

The OD $X\ ^2\Pi$ (v''=0, 1, N'') PSD arising from nonreactive collisional quenching of OD $A\ ^2\Sigma^+$ by H_2 is shown in Fig. 2. The distribution is measured using the three probe detection schemes described in the experimental section. One scheme is used to examine OD $X\ ^2\Pi$ (v''=1) products while two different schemes are employed to examine products in v''=0. The two OD (v''=0) data sets are merged into a single PSD by minimizing the root mean square deviation between the overlapping portions of the two distributions (N''=23-25). The OD $X\ ^2\Pi$ (v''=1) product distribution is scaled relative to that in v''=0 through branching fraction measurements, described in Sec. C, which indicate approximately 5-fold greater population in v''=0 than v''=1. The OD $X\ ^2\Pi$ (v''=0) products exhibit a remarkable degree of rotational excitation, peaking at N''=21 and

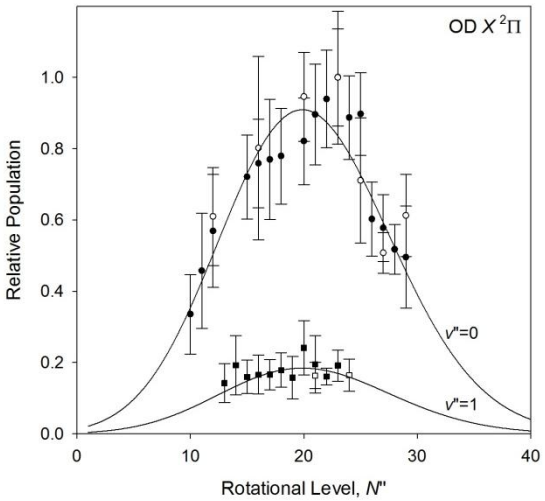

Figure 2. Experimentally measured OD $X\,^2\Pi$ quantum state distribution arising from quenching of OD $A\,^2\Sigma^+$ (v'=0, N'=0) by H_2 under single collision conditions. The relative populations in v''=0 (circles, ●) and v''=1 (squares, ■) with 1σ uncertainties are plotted as a function of rotational level, N'', with the corresponding fractional populations based on branching fraction measurements indicated on the right axis. Only the Π(A′) Λ-doublet states are shown; selectively probed Π(A″) Λ-doublet states had negligible population and are not shown for clarity. Populations in the F_1 and F_2 spin-orbit manifolds are represented by closed and open symbols, respectively. The lines through the data are fits to a three-parameter functional form described in the text.

falling off to higher and lower N''. The rotational distribution in v''=1 is qualitatively similar to that found in v''=0, but with fewer rotational states detected due to their smaller populations.

The OD $X\,^2\Pi$ (v''=0, 1) products were also examined for fine structure effects (F_n, ε), where we denote the parity, ε, or associated Λ-doublet, Π(A′) or Π(A″), and spin-orbit manifold, F_1 (J=N+1/2) or F_2 (J=N–1/2). Note that P and R lines probe the Π(A′) Λ-doublet component, while Q lines probe the Π(A″) component. All four fine structure components were measured for several OD $X\,^2\Pi$ (v''=0, N'') product rotational levels, namely N'' = 16, 20, 23, and 27. The two spin-orbit levels, F_1 and F_2, of equivalent N'' were found to have the same population within experimental uncertainty. In contrast, the OD $X\,^2\Pi$ products showed a significant Λ-doublet propensity with products of collisional quenching detected only in Π(A′) Λ-doublet levels. This indicates complete orbital alignment of the half-filled pπ orbital in the plane of the OD rotation. As a result, only the Π(A′) Λ-doublet levels are considered in the analysis that follows.

While the OD $X\,^2\Pi$ (v'', N'') PSD is extensive, it is incomplete. This is because not every product state could be probed. In some cases, overlapping transitions prevented probing product states in isolation. In other cases, specifically for low N'' levels (N''< 10), collision-induced population could not be detected above jet-cooled background OD $X\,^2\Pi$ originating from photolysis of DNO_3. A complete PSD is required to fully characterize the distribution and determine quantities such as the average vibrational and rotational energy of the OD $X\,^2\Pi$ products as well as the branching between quenching pathways.

We elected to model the OD $X\,^2\Pi$ PSD by fitting it to a three parameter Pearson Type III functional form.[35] A least squares fitting procedure is applied to fit the experimentally observed distributions to

$$P(N'') = C\frac{1}{b\,\Gamma(p)}(z)^{p-1}\exp(-z) \text{ where } z = \frac{N''-a}{b}$$

In this function, the variable N'' is the rotational quantum number; C is a scaling constant. The other parameters (a, b, and p) cooperatively define the peak ($a + pb$) and breadth ($\sqrt{pb^2}$), with p more specifically defined as a measure of the skew and kurtosis. Note that $\Gamma(p)$ is the standard gamma function at integer p. We stress that this functional form was selected for its simplicity and the goodness of fit to the experimental distribution, not for reasons of physical significance.

The three parameters characterizing the probability distribution (given in supplementary Table S1)[31] are obtained as follows. First, we assume that the v''=0 and 1 distributions have the same shape (as found previously for the OH + H_2),[18] since we have inadequate data to fit the v''=1 distribution separately. Next, the v''=0 and 1 distributions are scaled to one another by minimizing the root mean square deviation of populations between N'' levels common to both vibrational levels. Then, the combined distribution is fit to the Pearson Type III function to obtain values for the a, b, and p parameters. Finally, with a, b, and p fixed, branching fraction measurements for specific product rotational states in v''=0 and 1 (see Sec. C) are used to deduce the coefficients C for v''=0 and 1, which also provide the probability of populating the two vibrational levels. The average rotational excitation, in terms of rotational quantum number N'' and energy E_{rot},

for the most populated vibrational state (v''=0) and the overall average rotational energy $\langle E_{rot} \rangle$ of the OD $X\ ^2\Pi$ products are also determined from the fit parameters and associated uncertainties. These results are summarized in Table 1.

In a previous study on collisional quenching of OH $A\ ^2\Sigma^+$ by H_2, we used a two parameter Fisher-Tippett probability distribution to fit the experimental OH $X\ ^2\Pi$ population distribution.[18] In this work, we refit the OH $X\ ^2\Pi$ data, originally extending up to N''=19 for v''=0,[18] and include more recent data for the high N'' tail (specifically, N''=17, 19, 21, 23, and 25 for the F_1, e levels).[20] This combined data set has been refit using a three-parameter Pearson Type III functional form to extract experimental observables given in Table 1. [These results supersede the values in Table 1 of Ref. 18.] The parameters and results from the original and revised fits are compared in supplementary Table S1.[31]

2. Theoretical Results

The calculated OD product rovibrational distributions resulting from the trajectory calculations are shown in Fig. 3. The calculations capture the key trends observed experimentally: the OD products are released primarily in their ground vibrational state with extensive rotational excitation. The high degree of OD rotational excitation is readily evident in the animation of a nonreactive quenching trajectory available in supplementary material.[31] The calculated branching ratios for each vibrational state, summed over rotation states, are 49% in v''=0, 33% in v''=1, and 18% in v''=2. The rotational distributions have similar shapes in each product vibrational level. For the most populated product vibrational state, OD (v''=0), the rotational distribution increases

Table 1. Observables derived from experiment and theory on the OH/D products of nonreactive quenching from OH or OD $A\ ^2\Sigma^+$ with H_2. These include the vibrational population distribution P(v'') and average vibrational energy $<E_{vib}>$, the average rotational excitation, given in terms of rotational quantum number N″ and energy E_{rot} for the most populated vibrational state (v''=0), and the overall average rotational energy $<E_{rot}>$. The branching fraction Γ for nonreactive quenching is also listed.

	OH + H_2 Experiment[a]	OH + H_2 Theory[b]	OD + H_2 Experiment	OD + H_2 Theory
$<N''(v''=0)>$	14.7 ± 0.9	15.5	20.6 ± 0.8	23.9
$<E_{rot}(v''=0)>/cm^{-1}$	4480 ± 240	5250	4630 ± 180	6390
$P(v''=0)$	0.75 ± 0.08	0.66	0.77 ± 0.11	0.49
$P(v''=1)$	0.20 ± 0.03	0.25	0.16 ± 0.02	0.33
$P(v''=2)$	0.05 ± 0.01[c]	0.09	≤ 0.07 ± 0.01[d]	0.18
$<E_{rot}>/cm^{-1}$	4420 ± 170	5150	4580 ±160	5780
$<E_{vib}>/cm^{-1}$	1040 ± 110	1590	800 ± 50[d]	1800
Γ	12.5 ± 5.3%	11%[e]	19.6 ± 3.6%[d]	12%[e]

[a] Experimental data from Ref. 18 has been refit to include high *N* results from Ref. 20 using a three-parameter functional form to extract experimental observables (see text).
[b] Ref. 25.
[c] Population for $P(v''\geq3)$ is estimated at ≤ 0.01 from a surprisal analysis (Ref. 18).
[d] Population was not observed in v''=2; $P(v'' \geq 2)$ is estimated from a surprisal analysis. Without including this estimate, $<E_{vib}>$ = 440 ± 50 cm^{-1} and Γ = 18.3 ± 3.6% for v''=0, 1 only.
[e] Theoretically determined branching to nonreactive quenching based on diabatic sampling as discussed in Ref. 25.

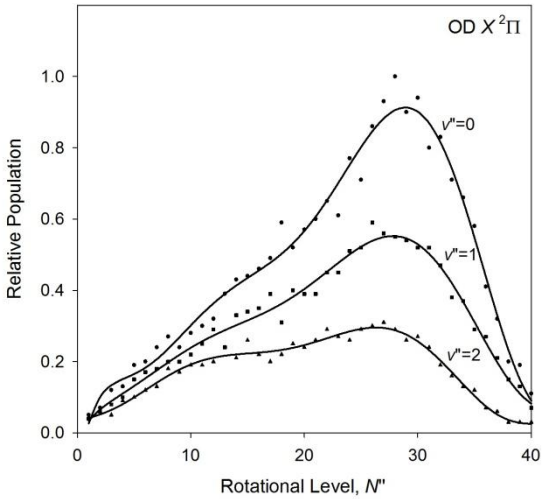

Figure 3. Theoretical OD $X\,^2\Pi$ rovibrational distribution determined from classical trajectory calculations of the post-quenching dynamics of OD $A\,^2\Sigma^+$ by H_2 as discussed in the text. Population distributions are shown for v''=0 (circles, ●), v''=1 (squares, ■), and v''=2 (triangles, ▲), and normalized to a maximum of unity in v''=0. The lines through the data are best-fit polynomial functions.

smoothly to about N''=20, then rises more rapidly to a peak at N''=29, and finally drops back to zero at N''=40. The peak occurs at slightly lower rotational levels in excited vibrational states, specifically v''=1, N''=28 and v''=2, N''=27. The OD product state distribution is compared with prior theoretical calculations for the OH + H_2 system and experimental results in Section V.

C. Branching Fraction for OD $X\ ^2\Pi$ Products

The relative intensities of the pump and probe LIF signals were measured for selected product states in order to determine the branching fractions Γ_i for nonreactive quenching into these particular OD $X\ ^2\Pi$ product states. The relative intensities of the pump and probe signals, recorded under saturated LIF conditions, are converted into the relative population of the OD $X\ ^2\Pi$ (v''=0, N''=1, e) level, labeled $P_{X,N=1}$, compared to that of the OD $X\ ^2\Pi$ (v'', N'', F_n, ε) product state i with collision-induced population $P_{Q,i}$. Furthermore, the population of the initially prepared OD $A\ ^2\Sigma^+$ (v'=0, N'=0) state can be related to $P_{X,N=1}$ through a degeneracy factor (1/3). The branching fraction Γ_i can then be defined in terms of the experimental observables as follows[17]

$$\Gamma_i = \frac{P_{Q,i}}{\frac{1}{3}P_{X,N=1}\left(1-\Phi_f\right)}$$

The denominator indicates the fraction of the initially prepared OD $A\ ^2\Sigma^+$ (v'=0, N'=0) population that is collisionally removed.

The branching fraction was measured for six specific OD $X\ ^2\Pi$ product channels, v''=0, N''=16, 18, 25, 26 and v''=1, N''=16, 17 for F_1, e levels. In v''=0, the most populated of these product states, N''=25, has a fractional population of 0.40(9)%. Taken

together with the branching fraction measured for N''=26, 0.33(9)%, gives a N''=25 / N''=26 population ratio of ~1.2, which is consistent with the relative populations from the fit of the OD $X\,^2\Pi$ PSD. Similarly, the branching fraction measurements for N''=16 in v''=0 and v''=1, 0.28(8)% and 0.07(2)%, yield a population ratio of approximately 4, which is in good accord with the more precise ratio for v''=0 to v''=1 derived below.

The branching fraction measurements enable the relative population distributions to be converted into fractional populations (see Fig. 2). This is done by scaling the amplitude of the fit for the relative population distribution based on the branching fraction measurements. This procedure is carried out separately for v''=0 and v''=1. The overall branching fraction to nonreactive quenching, Γ, is then obtained by summing the fractional populations for the $\Pi(A')$ Λ-doublet component over all OD $X\,^2\Pi$ rotational and spin-orbit states. Population in product channels not observed experimentally is estimated using the previously described fit. Production of OD $X\,^2\Pi$ (v"=0) accounts for 15.1±2.3% of the quenching products with a further 3.1±0.4% generated in v"=1 or a v''=0 to v''=1 ratio of (4.9 ± 1.0) to 1. Taken together, the OD $X\,^2\Pi$ products in v"=0 and 1 from nonreactive quenching account for 18.3±2.4% of quenching outcomes. By comparison, the trajectory calculations indicate a branching ratio for reactive to nonreactive quenching of 7:1, corresponding to 88% reactive and 12% nonreactive quenching outcomes.

V. Discussion

The OD $X\ ^2\Pi$ product state distribution and branching fraction following collisional quenching of OD $A\ ^2\Sigma^+$ by H_2 provide a new observational window on the dynamics of quenching collisions. The OD $X\ ^2\Pi$ products are generated with substantial rotational excitation and selective orbital alignment, yet little vibrational excitation. Branching fraction measurements show that nonreactive quenching is the minor pathway. These results are discussed in context of prior experimental studies on collisional quenching of OH $A\ ^2\Sigma^+$ by H_2/D_2. The results are also compared with theoretical predictions.

A. Hydroxyl Product Vibrational Distribution

The OD $X\ ^2\Pi$ products of quenching are detected in v''=0 and 1 with approximately 5 times more population in v''=0 than v''=1. A surprisal analysis was carried out to estimate population in higher vibrational levels.[36] Prior distributions for OD $X\ ^2\Pi$ and H_2 were calculated within a rigid-rotor harmonic-oscillator approximation using known term values.[37] The observed vibrational distribution is significantly colder than prior with a surprisal parameter λ_v=15.3 ± 0.7, suggesting that only a small amount (<7%) of nonreactive quenching products could be released in higher vibrational levels, $v''\geq 2$, of OD $X\ ^2\Pi$, and corresponding to less than 1.3% of all quenched products. Thus, we conclude that vibrational population distribution for OD $X\ ^2\Pi$ products has approximately 77% in v''=0 and 16% in v''=1, with an average vibrational energy of $\langle E_{vib}\rangle$ = 800 ± 50 cm^{-1} (Table 1). The observed vibrational distribution favoring Δv=0 is consistent with a Franck-Condon limit in which 'diagonal' transitions dominant due to

the small change in the OD equilibrium bond length between the $A\ ^2\Sigma^+$ and $X\ ^2\Pi$ states (from r_e = 1.0121 to 0.9697 Å).[37]

The small degree of vibrational excitation of the OD $X\ ^2\Pi$ products is similar to that observed previously for OH $X\ ^2\Pi$ products from quenching of OH $A\ ^2\Sigma^+$ by H_2. In that case, the OH $X\ ^2\Pi$ products were also released predominantly in v"=0 (75%) with decreasing population in higher vibrational levels, specifically 20% in v"=1 and 5% in v"=2 (Table 1). Approximately 4 times more population was found in v"=0 than v"=1; this combined with the higher vibrational frequency for OH results in a slightly higher average vibrational energy $<E_{vib}>$ = 1040 cm^{-1} for quenching of the $A\ ^2\Sigma^+$ state of OH than OD by H_2.[18]

The trajectory studies also indicate that the OH or OD $X\ ^2\Pi$ products of quenching have a small amount of vibrational excitation, populating mainly v''=0 and falling off to higher vibrational levels. The OH $X\ ^2\Pi$ distribution shows about 2.6 times more population in v''=0 (66%) than v''=1 (25%). The OD $X\ ^2\Pi$ distribution has about 1.5 times more population in v''=0 (49%) than v''=1 (33%), indicating a warmer distribution than found for OH $X\ ^2\Pi$ products. In both cases, the dynamical calculations predict somewhat more vibrational excitation of the OH/D products, with average vibrational energies $<E_{vib}>$ of 1590 (OH) and 1800 (OD) cm^{-1}, than observed experimentally.

B. Hydroxyl Product Rotational Distribution

The experimental (Fig. 2) and theoretical (Fig. 3) rotational distributions of the OD $X\ ^2\Pi$ products are highly nonstatistical, yet in both cases the rotational distributions

in each of the populated vibrational levels are similar to one another. As a result, we focus the discussion primarily on the rotational distribution of the most populated vibrational state (v''=0). The experimental distribution peaks at N''~21, falling off to higher and lower N'', with an average rotational energy of $\langle E_{rot}(v''=0)\rangle$ = 4630±180 cm^{-1}; this value is essentially the same as the overall average rotational energy of $\langle E_{rot}\rangle$ = 4580±160 cm^{-1} (see Table 1).

The experimental OD $X\ ^2\Pi$ (v''=0) product rotational distribution in both spin-orbit manifolds [Π(A′) only] is compared with that obtained previously for the OH $X\ ^2\Pi$ (v''=0) products from quenching of OH $A\ ^2\Sigma^+$ (v'=0, N'=0) by H_2 in Fig. 4, where the data are plotted as a function of the hydroxyl product rotational level. The OD $X\ ^2\Pi$ (v''=0) distribution is centered about a significantly higher rotational level, N''~21, than the distribution for OH products that peaks approximately 6 quanta lower at N''~15. Yet the average rotational energy of the OH products in v''=0, $\langle E_{rot}(v''=0)\rangle$ = 4480±240 cm^{-1} based on the new three-parameter fit of the data, and overall, $\langle E_{rot}\rangle$ = 4420±170 cm^{-1}, summarized in Table 1, are remarkably similar to those reported here for OD. The rotational distribution of the OD $X\ ^2\Pi$ (v''=0) products and that obtained previously for OH $X\ ^2\Pi$ (v''=0) products are replotted as a function of internal energy in Fig. 5 to emphasize the similarity of the experimental distributions. This indicates that the fraction of available energy deposited into product rotation is comparable for OH and OD, 13.6(5)% for OH and 14.1(5)% for OD, with no apparent limitation from the significant degree of rotational angular momentum that must be generated in the products. The

rotational angular momentum generated in the OD products is necessarily even larger than that for OH because of its smaller rotational constant.

Previously, Dempsey et al.[18] considered a simple kinematic model to rationalize the small increase in rotational excitation of OH $X\ ^2\Pi$ (v''=0) products from quenching of OH $A\ ^2\Sigma^+$ by D_2, peaking at N''~17 for the heavier isotope, as compared to H_2 (N''~15). Based on several assumptions detailed in Ref. 18, the rotational angular momentum, j_{OH}, generated in the quenching process was set equal to the orbital angular momentum of the products, $l = \mu v_{rel} b$, where μ is the reduced mass of the OH + H_2/D_2 system, v_{rel} is the relative velocity of the separating products, and b is the impact parameter. This led to the expectation that the D_2 collision partner would generate greater angular momentum in the OH $X\ ^2\Pi$ products (by a factor of 1.34), qualitatively but not quantitatively explaining the observed trend (factor of 1.14). Application of the same argument to the present work, where the reduced mass of OD-H_2 vs. OH-H_2 is essentially unchanged, would lead to the expectation that the rotational angular momentum of the OD or OH products would be the same. Fig. 4 clearly shows that this is not the case, indicating that the changes in the product state distribution resulting from different isotopomer combinations cannot be explained simply on kinematic grounds. Indeed, the trajectory calculations originating from the CoI region indicate a wide range of initial momenta are sampled in the microcanonical distribution.[25]

Both the OD and OH $X\ ^2\Pi$ product state distributions from nonreactive quenching by H_2 show a strong selectively for populating the $\Pi(A')$ Λ-doublet. In fact, the alignment of the half-filled $p\pi$ orbital in the product rotation plane is even stronger for

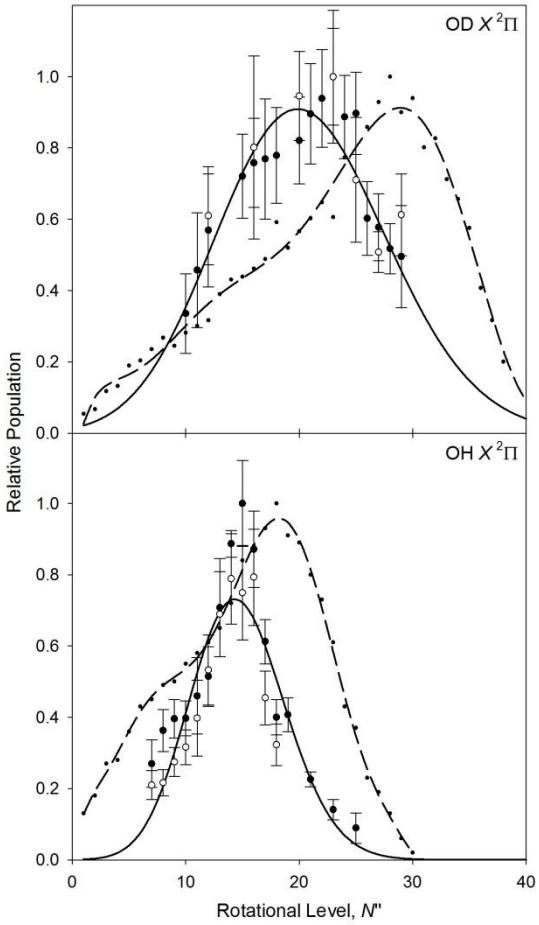

Figure 4. Experimental and theoretical OD $X\,^2\Pi$ (v''=0) product state distributions (upper panel), separately displayed in Figures 2 and 3, are compared with those for OH $X\,^2\Pi$ (v''=0) (lower panel) following quenching of OD or OH $A\,^2\Sigma^+$ by H_2. The experimental and theoretical results are plotted as a function of rotational level, N''. The OH $X\,^2\Pi$ (v''=0) experimental data is reproduced from Refs. 18, 20, although refit to a three-parameter functional form as described in the text. The theoretical OH $X\,^2\Pi$ (v''=0) distribution is reproduced from classical trajectory calculations in Ref. 25. Relative populations for experiment and theory are normalized to a maximum of unity for v''=0.

OD with essentially no products detected in the Π(A″) Λ-doublet component. As discussed previously,[18] the Λ-doublet propensity is a consequence of the symmetries of the $1^2A'$ and $2^2A'$ electronic states that form the conical intersection in planar geometries (see Fig. 1). For low rotational levels, H_2 is essentially spherical and the collision pair can be approximated as a pseudo-triatomic system on the $2^2A'$ surface. After passage through the conical intersection region, the OD or OH products emerge on the lower $1^2A'$ surface with the orbital containing the unpaired electron primarily in the plane of the collision, which is also the plane of OH/D rotation. Thus, the Π(A′) Λ-doublet selectively observed experimentally with the half-filled pπ orbital in the OH rotation plane validates the simplifying assumption that the $1^2A''$ electronic state can be neglected in the trajectory calculations. Ultimately, one will want to include a weak coupling to the $1^2A''$ electronic state to account for the smaller Π(A″) component evident in the OH $X\ ^2\Pi$ product distribution.

The OD (v''=0) product rotational distribution from trajectory calculations peaks at N''~29, although the asymmetry of the distribution (see Fig. 3), which is skewed to high N'', results in an average rotational excitation of $\langle N''\rangle$~24 and $\langle E_{rot}(v''=0)\rangle$ = 6390 cm^{-1}. When taking into account the rotational distributions in v''=0-2, the average rotational energy decreases to $\langle E_{rot}\rangle$ = 5780 cm^{-1} (see Table 1). When the OD (v''=0) product rotational distribution is binned into subsets with H_2 cofragments containing 0, 1, and 2 quanta of vibrational excitation, the peak of the OD rotational distribution is found to shift to lower N'' by 2-3 units per quantum of H_2 vibrational excitation. While both OD and OH products are predicted to have a high degree of rotational excitation, the

calculated OD rotational distribution peaks approximately 10 quanta higher than that for OH $X\,^2\Pi$ (v''=0) as shown in Fig. 4; the average N'' changes by a similar amount. The average rotational energy in v''=0 is also greater for OD than OH as depicted in Fig. 5. Overall, the trajectory calculations yield an average rotational energy for the OD products which is 12% larger than OH with $<E_{rot}>$ = 5150 cm^{-1} (Table 1), while the experimental data indicates that the average rotational energy is nearly unchanged for OD and OH products. In both cases, the dynamical calculations predict even greater rotational excitation of the OH/D products than observed experimentally. Nevertheless, the trajectory calculations clearly show that the extensive rotational excitation of the OH/OD products arises from the potential anisotropy on the lower $1^2A'$ surface as the collision partners separate. The differences between theory and experiment may well be due to the "democratic" sampling of conical intersections in the former. Full classical trajectories, which start from the reactants on the excited state potential, would eliminate this uncertainty and these calculations with non-adiabatic coupling to the ground state potential are planned.

C. Branching Fraction for Nonreactive Quenching

The branching fraction to nonreactive quenching has been independently measured for OD $A\,^2\Sigma^+ + H_2$. The branching fractions for individual OD $X\,^2\Pi$ quantum states were determined and then summed over the product state distribution to yield a branching fraction of 18.3 ± 2.3%. The branching fraction increases to 19.6% when including the estimated population in $v''\geq 2$. This compares quite well, albeit slightly larger, than the previously determined branching fraction for OH $A\,^2\Sigma^+ + H_2$ of 12 ±

5%.[17] In both cases, nonreactive quenching is found to be a minor pathway with H_2 and reactive quenching is the dominant channel. Some collision partners, such as N_2, result in predominantly nonreactive quenching[20] while others, such as O_2 and CO_2, result in a nearly equal split between reactive and nonreactive quenching.[19] In the theoretical investigation of OH $A\ ^2\Sigma^+ + H_2$, the branching to nonreactive quenching is found to be dependent on the initial momenta sampling method used. With diabatic sampling, the branching ratio for reactive to nonreactive quenching agrees well with experiment with an 8:1 ratio for OH and a 7:1 ratio for OD. Nonreactive quenching accounts for only 11% and 12% of the outcomes, respectively.

The reactive to nonreactive branching ratios for separate C_{2v}, and C_s and $C_{\infty v}$ symmetry CoI are also calculated for OD + H_2. Trajectories with initial configuration of $C_{\infty v}$ symmetry give rise to the largest branching ratio of reactive and nonreactive quenching, which is 9:1 for diabatic sampling. Those of C_s and C_{2v} symmetries result in branching ratio of 8:1 and 4:1, respectively, and thus there is some interesting sensitivity to the geometry at the conical intersection. It is gratifying that the calculated branching ratios for both OH $A\ ^2\Sigma^+$ and OD $A\ ^2\Sigma^+ + H_2$ are in good agreement with experiment; however, full dynamics calculations will be important to perform to verify whether this is fortuitous or a correct outcome of the "diabatic" sampling method. The very recent quantum dynamics calculations for OH $A\ ^2\Sigma^+ + H_2$ yield a branching ratio for reactive and nonreactive quenching of 5 to 1 at 0.06 eV and 3 to 1 at 0.4 eV collision energies.[26] The former is smaller than the 7:1 ratio observed experimentally at 50 K.[17]

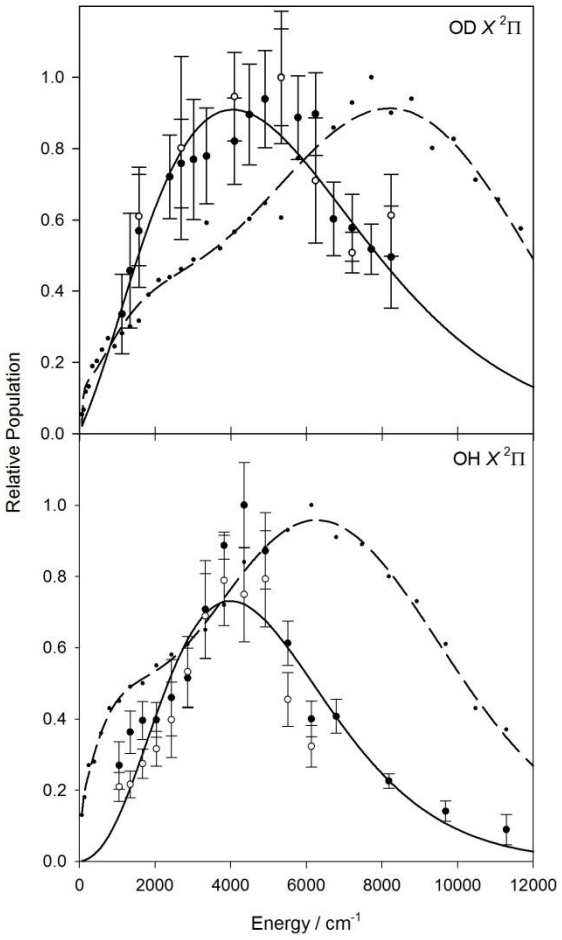

Figure 5. The experimental and theoretical results from Fig. 4, OD $X\,^2\Pi$ (v''=0) (upper panel) and OH $X\,^2\Pi$ (v''=0) (lower panel) product state distributions, are replotted as a function of OH or OD internal energy.

VI. Conclusions

The benchmark OH $A\ ^2\Sigma^+ + H_2$ system for collisional quenching has been investigated by changing the isotopic composition of the reactants to OD $A\ ^2\Sigma^+ + H_2$. This isotopic substitution changes the nuclear motions as the system evolves from reactants through the conical intersection region to products, but not the underlying electronic potential energy surfaces that give rise to reactive and nonreactive quenching. The principal findings from experiment and complementary trajectory calculations initiated in the conical intersection region are highly rotationally excited OD $X\ ^2\Pi$ products from nonreactive quenching with little vibrational excitation. Specifically, experimental results reveal a rotational distribution for the most populated v''=0 level that peaks at N''~21 with an average rotational energy of 4600 cm^{-1}. Theory shows even more rotational excitation and a slightly warmer vibrational distribution for the OD $X\ ^2\Pi$ products. Branching fraction measurements reveal that nonreactive quenching accounts for less than 20% of the quenching outcomes, while trajectory calculations within a "diabatic" model predict that 12% of the products arise from nonreactive quenching with the dominant contribution from reactive quenching. Experiments show a selectivity for the $\Pi(A')$ Λ-doublet component, indicating strong alignment of the half-filled $p\pi$ orbital in the OD rotation plane, which validates the use of only the A' surfaces in the trajectory calculations.

The OD $X\ ^2\Pi$ products from nonreactive quenching are released with an additional ~6 quanta of rotational angular momentum on average (experiment) than the OH $X\ ^2\Pi$ products from OH $A\ ^2\Sigma^+ + H_2$, which were characterized previously.[18]

Nevertheless, the rotational energy distributions observed experimentally for the hydroxyl radical products from quenching of OH $A\ ^2\Sigma^+$ and OD $A\ ^2\Sigma^+$ by H_2 are remarkably similar, both indicating that 14% of the available energy is deposited into product rotation. Theory shows a greater increase in the degree of rotational excitation of products for OD compared to OH ($\Delta N''$~8-10) and an increase in the average rotational energy of the products upon deuteration. Both experimental and theoretical results suggest a small increase in the branching fraction for nonreactive quenching upon quenching of OD compared to OH with H_2. Ongoing experimental and theoretical studies are focused on further characterization of the outcomes from reactive quenching.

Acknowledgments

The authors thank the Office of Basic Energy Sciences of the Department of Energy for support (DE-FG-87ER13782 and DE-FG02-97ER14782). M.I.L. thanks Thomas A. Stephenson (Swarthmore College) for valuable discussions.

References

1 D. R. Crosley, J. Phys. Chem. **93**, 6273 (1989).
2 K. R. German, J. Chem. Phys. **64**, 4065 (1976).
3 R. A. Copeland, M. J. Dyer, and D. R. Crosley, J. Chem. Phys. **82**, 4022 (1985).
4 B. L. Hemming and D. R. Crosley, J. Phys. Chem. A **106**, 8992 (2002).
5 B. L. Hemming, D. R. Crosley, J. E. Harrington, and V. Sick, J. Chem. Phys. **115**, 3099 (2001).
6 G. L. Vaghjiani and A. R. Ravishankara, J. Chem. Phys. **87**, 7050 (1987).
7 R. D. Kenner, F. P. Capetanakis, and F. Stuhl, J. Phys. Chem. **94**, 2441 (1990).
8 M. Asscher and Y. Haas, J. Chem. Phys. **76**, 2115 (1982).
9 P. W. Fairchild, G. P. Smith, and D. R. Crosley, J. Chem. Phys. **79**, 1795 (1983).
10 P. H. Paul, J. Quant. Spectrosc. Radiat. Transfer **51**, 511 (1994).

[11] A. E. Bailey, D. E. Heard, D. A. Henderson, and P. H. Paul, Chem. Phys. Lett. **302**, 132 (1999).
[12] D. T. Anderson, M. W. Todd, and M. I. Lester, J. Chem. Phys. **110**, 11117 (1999).
[13] M. W. Todd, D. T. Anderson, and M. I. Lester, J. Phys. Chem. A **105**, 10031 (2001).
[14] M. Ortiz-Suárez, M. F. Witinski, and H. F. Davis, J. Chem. Phys. **124**, 201106 (2006).
[15] I. B. Pollack, Y. X. Lei, T. A. Stephenson, and M. I. Lester, Chem. Phys. Lett. **421**, 324 (2006).
[16] P. A. Cleary, L. P. Dempsey, C. Murray, M. I. Lester, J. Kłos, and M. H. Alexander, J. Chem. Phys. **126**, 204316 (2007).
[17] L. P. Dempsey, C. Murray, and M. I. Lester, J. Chem. Phys. **127**, 151101 (2007).
[18] L. P. Dempsey, C. Murray, P. A. Cleary, and M. I. Lester, Phys. Chem. Chem. Phys. **10**, 1424 (2008).
[19] L. P. Dempsey, T. D. Sechler, C. Murray, and M. I. Lester, J. Phys. Chem. A **113**, 6851 (2009).
[20] L. P. Dempsey, T. D. Sechler, C. Murray, M. I. Lester, and S. Matsika, J. Chem. Phys. **130**, 104307 (2009).
[21] M. I. Lester, R. A. Loomis, R. L. Schwartz, and S. P. Walch, J. Phys. Chem. A **101**, 9195 (1997).
[22] D. R. Yarkony, J. Phys. Chem. **100**, 18612 (1996).
[23] D. R. Yarkony, J. Chem. Phys. **111**, 6661 (1999).
[24] B. C. Hoffman and D. R. Yarkony, J. Chem. Phys. **113**, 10091 (2000).
[25] E. Kamarchik, B. N. Fu, and J. M. Bowman, J. Chem. Phys. **132**, 091102 (2010).
[26] P.-Y. Zhang, R.-F. Lu, T.-S. Chu, and K.-L. Han, J. Phys. Chem. A **114**, 6565 (2010).
[27] S. M. Miller, D. C. Clary, A. Kliesch, and H. J. Werner, Mol. Phys. **83**, 405 (1994).
[28] M. A. Collins, personal communication (2008).
[29] I. M. Konen, E. X. J. Li, T. A. Stephenson, and M. I. Lester, J. Chem. Phys. **123**, 204318 (2005).
[30] B. Fu, E. Kamarchik, and J. M. Bowman, J. Chem. Phys., submitted for publication (2010).
[31] See supplementary material at http://dx.doi.org/10.1063/1.3487734 for animations of trajectories for nonreactive (Fig. S1) and reactive quenching (Figs. S2 and S3), and Table S1 with parameters derived from fits of experimental product state distributions.
[32] J. Luque and D. R. Crosley, SRI International Report MP 99-009 (1999).
[33] R. K. Lengel and D. R. Crosley, J. Chem. Phys. **68**, 5309 (1978).
[34] T. D. Sechler, L. P. Dempsey, and M. I. Lester, J. Phys. Chem. A **113**, 8845 (2009).
[35] *Handbook of Mathematical Functions with Formulas, Graphs and Mathematical Tables*, edited by M. Abramowitz and I. Stegun (Dover Publications, New York, 1972).
[36] R. D. Levine and R. B. Bernstein, *Molecular Reaction Dynamics and Chemical Reactivity*. (Oxford University Press, New York, 1987).

[37] K. P. Huber and G. Herzberg, *"Constants of Diatomic Molecules" (data prepared by J.W. Gallagher and R.D. Johnson, III) in NIST Chemistry WebBook, NIST Standard Reference Database Number 69*. (National Institute of Standards and Technology, Gaithersburg MD, 20899, http://webbook.nist.gov, 2008).

CHAPTER 3
Reactive quenching of OD $A\ ^2\Sigma^+$ by H_2: Translational energy distributions for H- and D-atom product channels

The experimental research presented in this chapter was performed at the University of Pennsylvania. This research has been published as a paper in the *Journal of Chemical Physics*.

Reference: J. H. Lehman, J. L. Bertrand, T. A. Stephenson, M. I. Lester, *J. Chem. Phys.*, **135**, 144303 (2011).

I. Introduction

The hydroxyl radical is an important species in atmospheric and combustion environments, where it is often detected using laser-induced fluorescence (LIF) on the OH $A\,^2\Sigma^+$ - $X\,^2\Pi$ band system.[1] However, collisions with molecular partners abundant in these environments are known to efficiently remove OH from the excited $A\,^2\Sigma^+$ state, resulting in reduced fluorescence lifetimes and quantum yields. The rate of this collisional quenching process has been studied for a variety of molecular partners over a wide range of temperatures and initial OH $A\,^2\Sigma^+$ rotational states.[2-7] In general, the rates were found to decrease with increasing temperature and OH $A\,^2\Sigma^+$ rotational excitation, indicating that quenching is controlled by an attractive interaction with a significant OH orientation dependence.[4-7] Several empirical models have been proposed to explain the quenching phenomena,[2,8-11] yet only recently has the mechanism for quenching of OH $A\,^2\Sigma^+$ by even simple molecular partners (H_2, N_2) become evident from experiment and first-principles theory.[12-24]

In order to elucidate new information about the mechanism, recent experimental studies have focused on the outcomes of collisional quenching. Two possible outcomes for quenching of OH $A\,^2\Sigma^+$ by H_2 have been examined in this laboratory: nonreactive quenching that returns OH to its ground $X\,^2\Pi$ electronic state,

$$\text{OH}\ A\,^2\Sigma^+ + \text{H}_2 \rightarrow \text{OH}\ X\,^2\Pi\ (v'', N'') + \text{H}_2$$

and reactive quenching, which yields new products

$$\text{OH}\ A\,^2\Sigma^+ + \text{H}_2 \rightarrow \text{H} + \text{H}_2\text{O}.$$

There is insufficient energy released upon quenching to access higher-energy three-body breakup channels. Previous investigations focused on the quantum state distribution of the OH $X\ ^2\Pi$ products from nonreactive quenching under single collision conditions for several isotopic variants of this system,[13-15,21] with the most recent study focused on nonreactive quenching of OD $A\ ^2\Sigma^+$ by H_2.[19] The OH/D $X\ ^2\Pi$ products were found to exhibit extensive rotational excitation and strong Λ-doublet selectivity with minimal vibrational excitation. From product branching studies, the nonreactive pathway was shown to be a minor channel, accounting for less than 20% of quenching outcomes.[15,19] Reactive quenching was found to be the dominant channel, accounting for more than 80% of quenching events.

In this paper, we extend our recent study of the partially deuterated OD $A\ ^2\Sigma^+ + H_2$ system by examining the dominant reactive quenching outcome. Previously, the translational energy release associated with reactive quenching of OH $A\ ^2\Sigma^+ + H_2$ was measured by probing the H-atom products using Doppler spectroscopy on the 2s←←1s transition, as initially demonstrated by Anderson et al.[12] The Doppler profile exhibited a prominent peak near line center, corresponding to minimal kinetic energy release, and a smaller broad component extending out to the maximum possible shift. The minimal kinetic energy release for the H-atom products implied that most of the available energy resulted in internal excitation of water, producing extremely 'hot' water with internal excitation approaching its dissociation limit. Analogous studies were carried out for the OH $A\ ^2\Sigma^+ + D_2$ isotopic variant,[22] with a surprising finding of both D + HOD and H + D_2O products. The translational energy distributions arising from reactive quenching of

OH $A\ ^2\Sigma^+ + H_2/D_2$ are revisited in the present work using an improved analysis procedure. New results are also presented for OD $A\ ^2\Sigma^+ + H_2$, where again there is the possibility of distinguishing reactive quenching that occurs via H- and D-atom channels.

The D-atom products from reactive quenching of OH $A\ ^2\Sigma^+$ by D_2 have also been probed using a high-*n* Rydberg tagging method in a crossed molecular beam experiment by Davis and coworkers.[20] A fixed-source, rotatable detector crossed molecular beams apparatus was used to determine the center-of-mass (COM) frame angular scattering of the D-atom products. The D atom products were found to be predominantly forward scattered with a minor backward component relative to incident D_2. The COM angular scattering distribution indicated that reactive quenching occurs primarily by a direct reaction mechanism in which the incoming OH $A\ ^2\Sigma^+$ abstracts a D-atom from D_2 at relatively large impact parameters and the heavy HOD product continues in nearly the same direction as the incident OH $A\ ^2\Sigma^+$. They also determined the kinetic energy distribution of the D-atom products, which will be compared with related experimental and theoretical results later, again showing that most of the available energy (~88%) is channeled into internal excitation of the HOD product. They were unable to examine the H-atom products due to experimental limitations.

The nonadiabatic dynamics of the OH ($A\ ^2\Sigma^+$, $X\ ^2\Pi$) + H_2 system has been the focus of numerous theoretical studies.[13,17,18,23-27] As illustrated in Figure 1, ab initio calculations have identified seams of conical intersection that couple the upper and lower adiabatic surfaces for configurations in which the oxygen side of the hydroxyl radical points toward the H_2 molecule, giving rise to barrierless pathways from OH $A\ ^2\Sigma^+ + H_2$ to

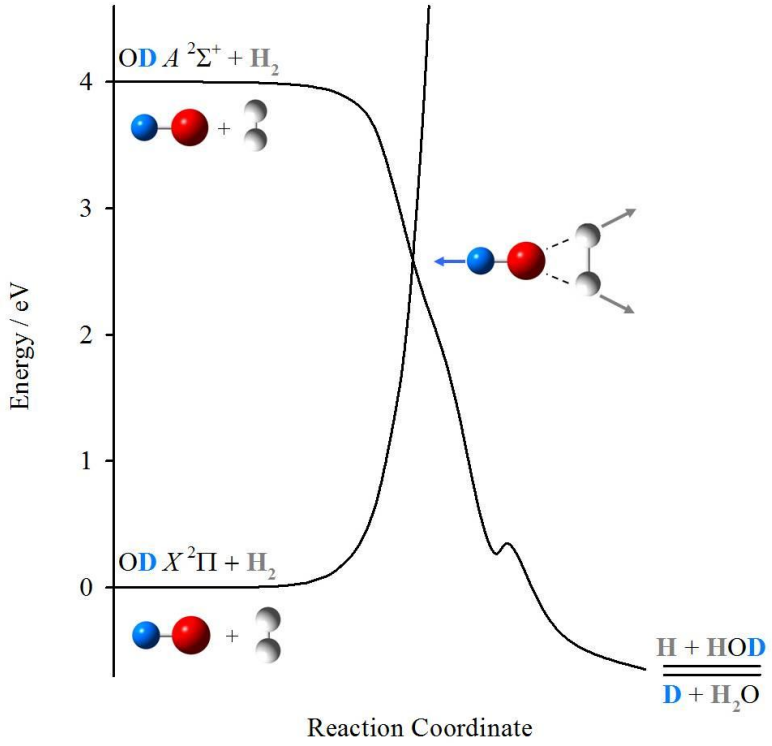

Figure 1. Simplified reaction coordinate for quenching of OD $A\ ^2\Sigma^+$ by H_2 (adapted from Ref. 27) via the C_{2v} DO-H_2 conical intersection (from Ref. 25). Both nonreactive quenching producing OD $X\ ^2\Pi + H_2$ and reactive quenching pathways to H + HOD or D + H_2O products are illustrated.

nonreactive OH $X\ ^2\Pi$ + H_2 and reactive H + H_2O products, releasing 4.02 and 4.72 eV of energy, respectively.[25,26] Such calculations have been extended to map out the upper and lower adiabatic surfaces of $^2A'$ symmetry as a function of OH orientation and interfragment distance, the former revealing the steep angular gradient leading toward and away from the HO-H_2 conical intersection region.[13] This feature of the topography has been used to explain, at least qualitatively, the high degree of rotational excitation observed for the OH $X\ ^2\Pi$ fragments. Further insights on the nonadiabatic quenching process can be elucidated from recent classical trajectory studies of the post-quenching dynamics[17,18] and nonadiabatic quantum reactive scattering calculations.[23,24] These dynamical approaches have been used to predict experimental observables, including the quantum state distributions of OH $X\ ^2\Pi$ products, translational energy distributions of the H-atom products of reaction, and the branching ratio between nonreactive and reactive pathways, as well as unobserved properties that may reflect the evolution of the system through the conical intersection region.

Han and coworkers used a time-dependent quantum wavepacket method to compute the integral cross sections for reactive and nonreactive quenching of electronically excited OH $A\ ^2\Sigma^+$ by H_2 and D_2 as a function of collision energy based on newly developed 1A′ and 2A′ CASSCF/MRCI potentials for OH ($A\ ^2\Sigma^+$, $X\ ^2\Pi$) + H_2 in planar configurations.[23,24] In addition, they predict the vibrational and rotational state distributions of the OH $X\ ^2\Pi$ products, the vibrational distribution of the H_2/D_2 products, and the average internal and translational energies of the products of nonreactive quenching at different collision energies. These calculations are in accord with

experimental observation of highly rotationally excited OH $X\ ^2\Pi$ products,[13-15] and predict that even greater proportions of the available energy will flow into product translation and H_2 vibrational excitation. They have not yet predicted the corresponding properties for the reactive quenching channel, which is the primary focus of the present experimental study.

Bowman and coworkers carried out classical trajectory calculations of the postquenching dynamics of OH $A\ ^2\Sigma^+$ by H_2 and its isotopic variants,[17-19,28] starting from previously identified representative points along the seams of conical intersections.[25] The dynamical calculations were performed on a new adiabatic, full-dimensional, global potential energy surface (1A′) for OH $X\ ^2\Pi + H_2$ computed using the MRCI+Q/aVTZ method. They find that the branching between reactive and nonreactive quenching channels is sensitive to the initial momenta sampling method utilized, with prompt 'directed' dynamics through the seams in a diabatic model predicting that reactive quenching will dominate as observed experimentally.[17,18] These authors indicate that an abstraction mechanism is strongly favored for reactive quenching, but nevertheless find evidence of a minor insertion pathway; the latter is far more significant in experimental studies[22] as further demonstrated in the current work.

Bowman and coworkers also predict the rovibrational state distributions for the OH $X\ ^2\Pi$ and H_2 products of nonreactive quenching, with high rotational and minimal vibrational excitation of OH $X\ ^2\Pi$ products as seen experimentally. In addition, they predict high vibrational excitation of the experimentally unobserved H_2 products that result from the extended H-H bond in the conical intersection region. Furthermore, they

compute the internal energy distribution of the H_2O product and the corresponding translational energy release for the reactive quenching channel, the latter of which is examined in the present work. The trajectory calculations predict that reactive quenching leads to 'hot' water, which is overwhelmingly bending (v_b) excitation with a distribution peaked at v_b=13 (~2.5 eV). They yield a significantly smaller degree of excitation for stretches and much lower probability per quantum state with only modest rotational excitation.

This paper focuses on reactive quenching outcomes for the partially deuterated OD $A\ ^2\Sigma^+ + H_2$ system. The mixed isotope system permits the H + HOD and D + H_2O pathways for reactive quenching to be separated from one another. Varying the isotopic composition of the system also allows a new set of observables to be measured, while keeping the electronic potential energy surfaces that control quenching unchanged. These new experimental results are compared with previous studies of OH $A\ ^2\Sigma^+ + H_2/D_2$ reactive quenching,[12,20,22] and discussed in the context of recent theoretical studies of the quenching dynamics.

II. Experimental Methods

The experimental methods are similar to those used previously in this laboratory for studies of reactive quenching of OH $A\ ^2\Sigma^+$ by H_2/D_2.[12,22] In the present study, OD $X\ ^2\Pi$ radicals are generated in the throat of a pulsed supersonic jet expansion by photolysis at 193 nm (Coherent COMPex 102) of DNO_3 (98 at. % D, 90 wt % in D_2O) entrained in 30% H_2/He carrier gas with a backing pressure of 110 psi. In some experiments, OH X

$^2\Pi$ radicals were generated in a similar fashion using HNO_3 (98% fuming). The UV pump laser excites the OD radicals on the $A\ ^2\Sigma^+$ - $X\ ^2\Pi$ (0,0) $P_1(1)$ transition at 307 nm in the collisional region of the expansion at a distance x/D = 2, where D is the nozzle diameter. The pump beam is generated by frequency doubling (KDP) the output of a Nd:YAG (532 nm) pumped dye laser (Rhodamine 640, 4-8 mJ, 7 ns, 0.08 cm^{-1}). A photomultiplier tube (PMT, ET Enterprises 9813Q) with a 308 nm bandpass filter collects the pump laser-induced fluorescence (LIF).

After a 50 ns delay, a second spatially overlapped and counter-propagating UV probe laser beam intersects the expansion; both lasers are gently focused with 50 cm f.l. lenses. The probe beam at 243 nm is generated by frequency doubling (BBO) the output of a Nd:YAG (355 nm) pumped dye laser (Coumarin 480, 2-3 mJ, 7 ns) with an effective two-photon line width of 0.5 cm^{-1}. The probe laser monitors the production of H/D atoms on a two-photon ($2\ ^2S \leftarrow\leftarrow 1\ ^2S$) transition. A solar blind PMT (ET Enterprises 9403B) with a notch filter centered at 121.5 nm collects the resulting Lyman-α fluorescence.[29,30] Signals from the PMTs are preamplified, processed with a digital storage oscilloscope (LeCroy WaveRunner 6050A) and transferred to a laboratory computer for further analysis.

For the collection and integration of the H/D atom signals, an active background subtraction is utilized in order to distinguish between H/D atoms produced from the reactive quenching process and other sources of H/D atoms (background). The background subtraction scheme is implemented by operating the pump laser (5 Hz) at half the repetition rate of the probe laser (10 Hz). On alternating laser shots, the H/D

atom signal arising from the probe laser only (PROBE) is subtracted from the combination of the pump and probe lasers (PUMP+PROBE), yielding the desired signal [(PUMP + PROBE) – PROBE] from reactive quenching.

There are two primary sources of background H/D atoms: photolysis of DNO_3 produces background D atoms (also seen in pure He as the carrier gas)[31] and reaction of OD $X\ ^2\Pi$ with H_2 generates background H atoms.[32] The background H/D atoms are cooled significantly in the expansion, resulting in narrow Gaussian line profiles with typical Doppler linewidths of less than 1 cm^{-1} under these experimental conditions. The Gaussian linewidth is used to estimate the collision energy, $E_{coll} \sim 0.005$ eV, under the present experimental conditions.

Numerous tests were performed to determine the sensitivity of the H/D atom signals from quenching and background to various experimental parameters. Both signals are very sensitive to probe laser power, as expected for a two-photon transition, with a quadratic power dependence observed over the 1-3 mJ range. The H/D atom signals from quenching are unchanged with variations in photolysis laser power (40-120 mJ) and pump laser power (1-10 mJ). The H/D Doppler line shapes from quenching are unchanged over a 150 ns pump-probe timescale indicating that secondary collisions with the H_2/He carrier gas mixture do not change the velocity distribution of the H/D products. The best H/D signal from quenching was found at the highest backing pressure of 110 psi. These collision conditions are analogous to those used previously for detecting H/D atom products of quenching in this laboratory.[12,22]

III. Results

A. Doppler profiles of H- and D-atom products

OD radicals are prepared in the lowest rovibronic level of the excited $A\ ^2\Sigma^+$ electronic state with the pump laser and quenched by H_2 in the collisional region of a pulsed supersonic expansion. Typically, the OD $A\ ^2\Sigma^+$ fluorescence lifetime is ~75 ns under the present experimental conditions as determined by fitting waveform traces of the pump LIF signal to a single exponential decay. This is significantly shorter than the OD $A\ ^2\Sigma^+$ radiative lifetime of ~700 ns,[33] indicating a quenching rate of $(84\ \text{ns})^{-1}$.

The H/D atom products from reactive quenching of OD $A\ ^2\Sigma^+$ by H_2 are then probed using two-photon excitation (2s←←1s). The Doppler profiles of the H- and D-atom products are recorded by scanning the probe laser while using active background subtraction to collect the data. The resultant Doppler profiles, summed from multiple scans to improve the signal to noise ratio, are plotted as a function of two-photon energy in Figure 2. The Doppler profiles of the H- and D-atom products are centered about their respective two-photon transitions at 82259.2 and 82281.5 cm^{-1}. The quality of the active background subtraction procedure used to record the data can be seen near line center with the pump laser blocked as shown by representative traces in Figure 2. The H/D signals arising from quenching [(PUMP + PROBE) – PROBE] are on the order of 7-10 times smaller than the background signals (PROBE only; not shown) at line center, yet larger than background in the wings.

The integrated areas of the Doppler profiles are proportional to the H or D product number density.[34] Therefore, the branching between the two reactive channels for

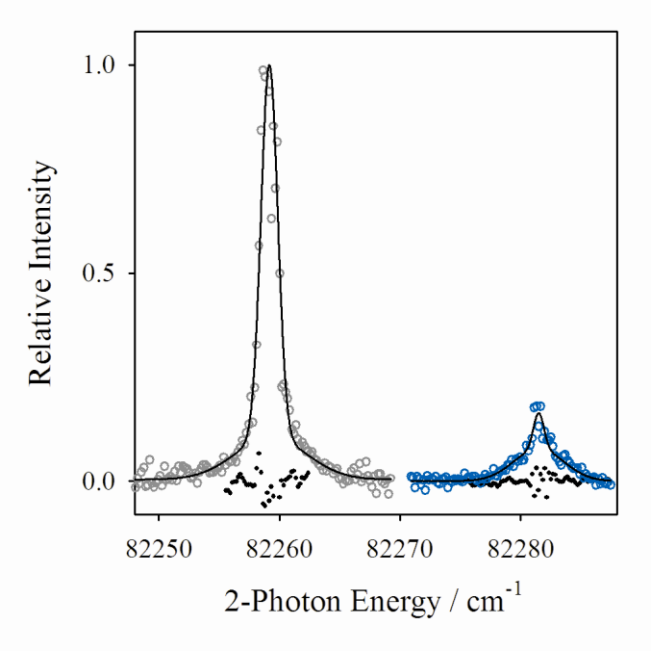

Figure 2. Doppler profiles (○) of H (grey) and D (blue) atom products from reactive quenching of OD $A\ ^2\Sigma^+$ by H_2, centered about their respective two-photon transitions at 82259.2 and 82281.5 cm^{-1}, and acquired using active background subtraction of probe laser only signals. The smooth curves through the data are added to guide the eye. Also shown are pump laser-blocked signals (●), illustrating the quality of the active background subtraction procedure near line center.

quenching of OD $A\ ^2\Sigma^+$ by H_2 can be directly determined by integrating the experimental data yielding an H:D ratio of 3:1. This shows that reactive quenching primarily forms H + HOD products that accounts for 75% of the reactive quenching outcomes. Nevertheless, the D+ H_2O channel is significant, accounting for 25% of outcomes.

The H/D-atom line profiles resulting from reactive quenching of OD $A\ ^2\Sigma^+ + H_2$ are replotted as Doppler shifts relative to line center in Figure 3. The H-atom profile is strongly peaked about line center with smaller broad contributions extending out to the maximum shift. By comparison, the D atom profile has a smaller contribution near line center, with a larger component seen in the wings spanning out to the maximum shift.

The maximum Doppler shift can be determined from the total energy available E_{avail} to the reaction products

$$E_{avail} = E_{h\upsilon} - \Delta H_{rxn} + E_{coll}\,.$$

where E_{hv} = 4.033 eV for the OD *A*-*X* (0,0) $P_1(1)$ transition, ΔH_{rxn} is the energy released in the ground state OD $X\ ^2\Pi + H_2$ reaction (taking into account changes in enthalpy of formation for the different isotopes),[35] and E_{coll} ~ 0.005 eV. Using conservation of energy and linear momentum, the maximum H-atom velocity is readily determined

$$v_H^{\max} = \sqrt{\frac{2E_{avail}}{m_H\left(1+m_H/m_{HOD}\right)}}\,.$$

From the above equations, and analogous ones for D atoms, the maximum velocities are $v_H^{\max} = 2.94\times10^4$ m/s and $v_D^{\max} = 2.01\times10^4$ m/s, corresponding to maximum Doppler shifts

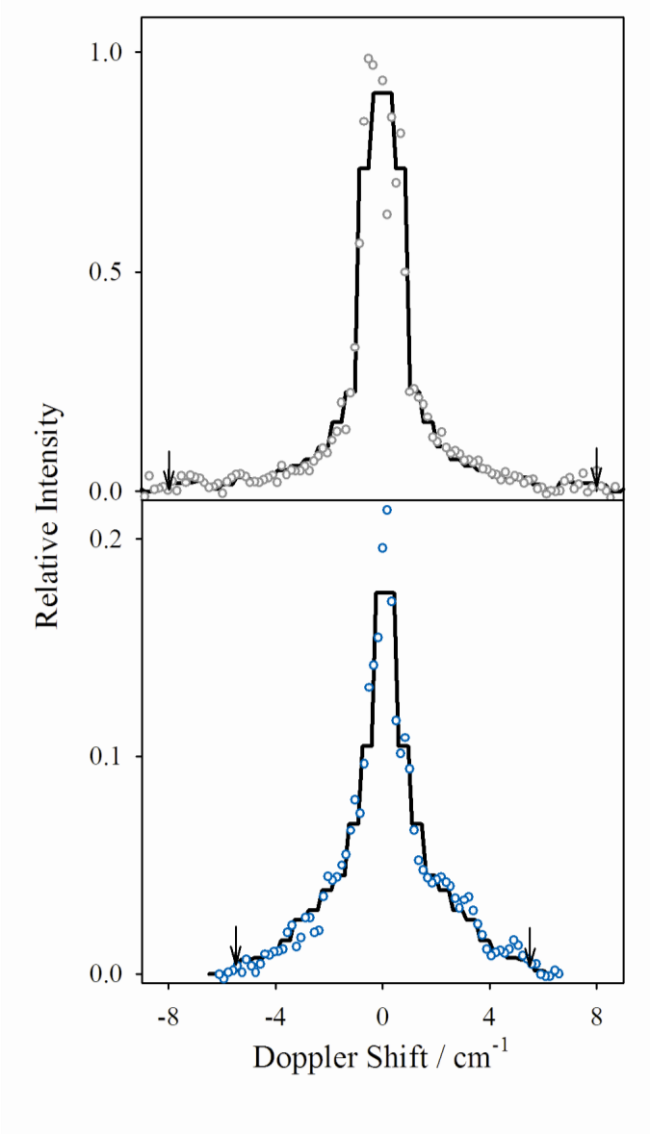

Figure 3. Doppler profiles (○) for H (grey) and D (blue) atom products arising from quenching of OD $A\ ^2\Sigma^+$ by H_2, which is replotted from Figure 2 as Doppler shifts from line center of the respective two-photon transitions. Note the scale change in relative intensity for the lower panel. The summed discrete step functions representing the best fits to the H/D Doppler profiles (solid line) is also illustrated. The arrows indicate the maximum Doppler shifts assuming all of the available energy from reaction goes into translational energy of the H (or D) atom products.

of ±8.06 cm^{-1} and ±5.54 cm^{-1}. The maximum Doppler shift is indicated in each panel of Figure 3 by a set of arrows.

B. Analysis of Doppler profiles

The Doppler profile is a one-dimensional projection of a three-dimensional velocity distribution along the laser propagation axis. If all of the H or D atoms were to move at the same velocity v in an isotropic spatial distribution, the Doppler profile would appear as a flat-topped box, or step function, convolved with the laser bandwidth. The experimentally observed Doppler profiles reflect a distribution of velocities, assumed to be spatially isotropic, with varying probabilities. In order to characterize this distribution, the Doppler line shapes are fit to a series of step functions, which can be viewed as a set of discrete basis functions. The step functions have a form factor proportional to 1/v to give each box equal weighting.[36] Each basis function differs from the next by ~1800 m/s, corresponding to the 0.5 cm^{-1} effective two-photon laser linewidth. The Doppler profile is fit to the basis set in a chi-squared minimization routine by adjusting the amplitudes of the step functions using singular value decomposition. [The fitting procedure is illustrated for a simple Gaussian line profile in Appendix I.[37]] The summed discrete step functions representing the best fits to the H/D Doppler profiles are superimposed on the experimental data in Figure 3. The best fit yields a velocity probability distribution, P(v), normalized to the relative integrated areas of the H/D Doppler profiles, which can be readily converted to a product translational energy distribution, $P(E_T)$.

The resultant $P(E_T)$ distributions obtained from the H/D Doppler profiles recorded for reactive quenching of OD $A\ ^2\Sigma^+$ by H_2 are plotted in Figure 4. Also shown are the $P(E_T)$ distributions obtained by reanalyzing the H/D-atom Doppler profiles previously reported for OH $A\ ^2\Sigma^+ + D_2$.[12,22] The original data and revised fit showing the summed discrete step functions are given in Figure 2 of Appendix I.[37] The H-atom Doppler profile resulting from reactive quenching OH $A\ ^2\Sigma^+$ of H_2 was repeated in the present study, shown in Figure 3 of Appendix I[37] with the basis functions yielding the best fit, which gives the same $P(E_T)$ distribution (Figure 4) as that derived from reanalysis of previously reported data.[12] The smooth curves through the $P(E_T)$ points are a fit to the sum of two lognormal distribution functions that minimizes chi-squared, which is intended as a guide to the eye; this functional form has no inherent physical significance. Two lognormal functions were required to obtain a statistically acceptable fit for the $P(E_T)$ distributions shown in top panel for OH $A\ ^2\Sigma^+ + H_2$ and the D-atom channel from OD $A\ ^2\Sigma^+ + H_2$ (right panel) in Figure 4. For the H-atom channel from OH $A\ ^2\Sigma^+ + D_2$ (right panel), two lognormal functions give a much better fit than one, but the uncertainty at low E_T limits the quality of the fit. A single lognormal distribution was adequate to obtain a good fit for the $P(E_T)$ distributions shown in the left-hand panels for the mixed isotopes; only marginal improvement to the fit was obtained with the sum of two lognormal functions. (Two lognormal functions are depicted in Figure 4.)

Earlier analysis of the H/D Doppler profiles from OH $A\ ^2\Sigma^+ + H_2/D_2$ reactive quenching was based on fitting the profiles to the sum of two Gaussian functions. The

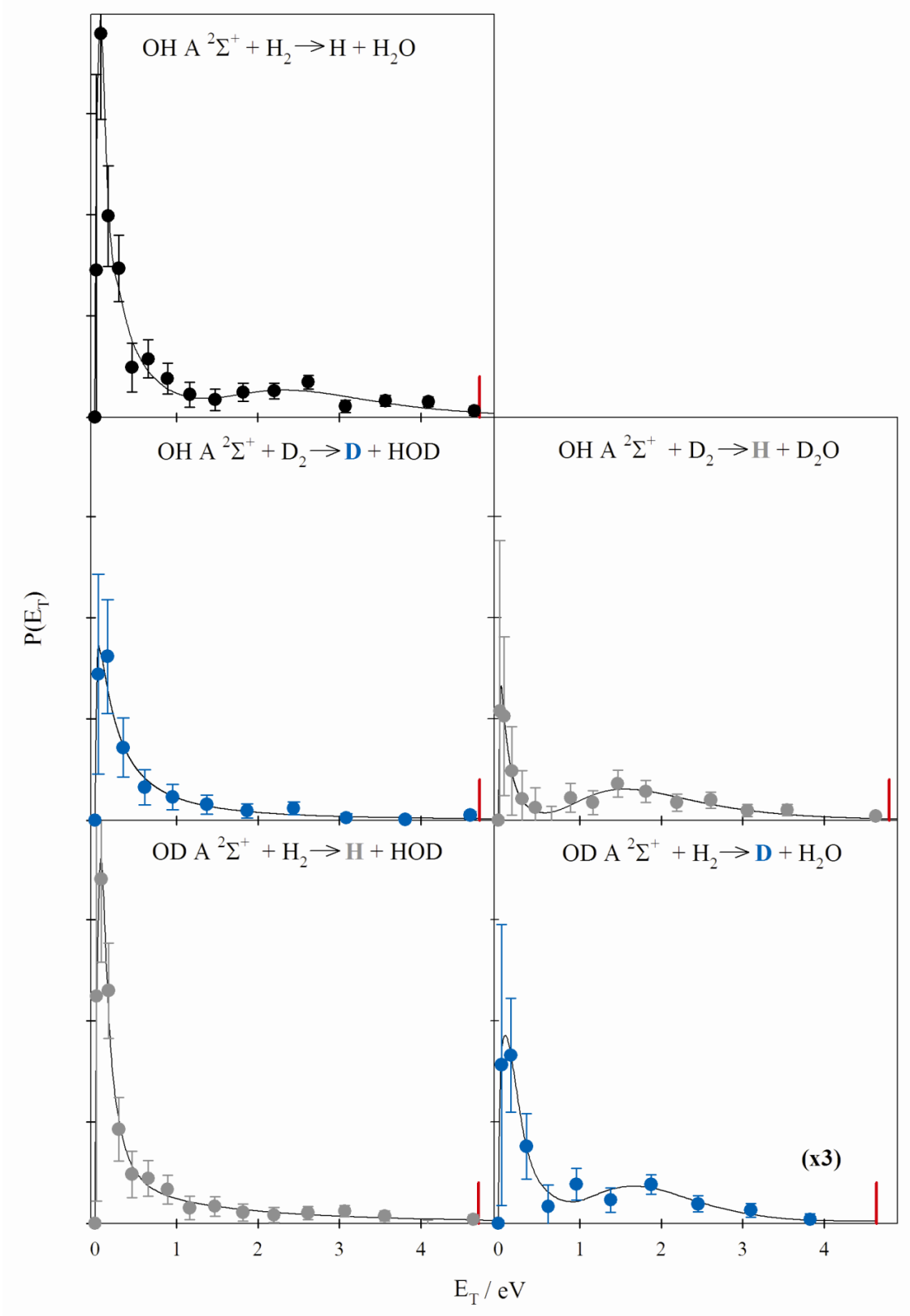
OH A $^2\Sigma^+ + H_2 \rightarrow H + H_2O$
OH A $^2\Sigma^+ + D_2 \rightarrow$ **D** + HOD
OH A $^2\Sigma^+ + D_2 \rightarrow$ **H** + D_2O
OD A $^2\Sigma^+ + H_2 \rightarrow$ **H** + HOD
OD A $^2\Sigma^+ + H_2 \rightarrow$ **D** + H_2O
(x3)
$P(E_T)$
0
1
2
3
4
E_T / eV

Figure 4. Translational energy distributions, $P(E_T)$, derived for the H- and D-atom products from reactive quenching of OH $A\ ^2\Sigma^+ + H_2$ (top), OH $A\ ^2\Sigma^+ + D_2$ (middle), and OD $A\ ^2\Sigma^+ + H_2$ (bottom) with discrete points from best fits to Doppler profiles and smooth curves based on lognormal distribution functions to guide the eye. The $P(E_T)$ distributions are normalized to the relative integrated areas of the H/D Doppler profiles; note the scale change for the OD $A\ ^2\Sigma^+ + H_2 \rightarrow D + H_2O$ channel. Reactions yielding H- and D-atom products are color coded as grey and blue, respectively. Vertical red lines indicate available energies, which differ slightly due to changes in OH/OD transition frequency and zero-point energy for the various isotopes of water.

bimodal form of the Doppler profiles suggested that two different velocity distributions resulted from quenching, and each component was separately converted to a Boltzmann translational energy distribution. The present analysis makes no assumptions about the functional form of the Doppler profile, which was previously constrained to a Gaussian functional form, or resultant $P(E_T)$ distribution, and thus is strongly preferred over the earlier analysis.

C. Translational energy distributions

In reactive quenching of OD $A\ ^2\Sigma^+$ by H_2, the two product channels, H + HOD (75%) and D + H_2O (25%), exhibit distinctly different $P(E_T)$ distributions (Figure 4, bottom panels). The $P(E_T)$ distribution for H + HOD products exhibits a strong peak at low translational energy with approximately 2/3 of the $P(E_T)$ distribution below 0.5 eV. A long tail accounts for the remaining ~1/3 of the $P(E_T)$ distribution for H + HOD products, which extends to the energetic limit. The H + HOD products have an average translational energy of 0.48 eV, which corresponds to 10% of the 4.71 eV of available energy. By contrast, the pathway producing D + H_2O has a small peak at low translational energy (below 0.5 eV) accounting for about half of the distribution. The balance of the $P(E_T)$ distribution for D + H_2O products lies at higher translational energy with a distinctive secondary peak at approximately 1.8 eV and falling off toward the energetic limit. In this case, the average translational energy of the D + H_2O products is 0.82 eV, corresponding to 18% of the 4.64 eV of available energy (see Table S1).[37]

Reactive quenching of OH $A\ ^2\Sigma^+$ by D_2 also yields different $P(E_T)$ distributions for its two channels (Figure 4, middle panels). In the primary D + HOD (60%) product

channel, a peak (~2/3) dominates the $P(E_T)$ distribution at low translational energy (below 0.5 eV). A long tail (~1/3) stretches out to the energetic limit. In the alternate H + D_2O (40%) channel, a small peak (~1/3) seems to be evident at low translational energy (below 0.5 eV). Most (~2/3) of the $P(E_T)$ distribution for the H + D_2O channel is found in a broader secondary feature at higher translational energy peaking at 1.6 eV and extending to the energetic limit.

Finally, the product $P(E_T)$ distribution from reactive quenching of OH $A\ ^2\Sigma^+$ by H_2 (Figure 4, top panel) shows a prominent peak at low translational energies (below 0.5 eV), accounting for approximately 60% of the products. This is followed by a secondary broader peak (40%) at approximately 2.6 eV with a tail that extends to the energetic limit. A discussion of the original (Gaussian) and revised fits, and the resultant $P(E_T)$ distributions for OH $A\ ^2\Sigma^+ + H_2/D_2$ is given in Appendix I.[37]

IV. Discussion

A previous study of reactive quenching in the OH $A\ ^2\Sigma^+ + D_2$ system from this laboratory in 2001 presented a simple interpretation of the H/D translational energy distributions derived from Doppler profiles, which had been fit using the sum of two Gaussian functions that separates the $P(E_T)$ distribution into two distinct components.[22] The narrow component observed at low E_T in the D-atom channel was attributed to a direct abstraction mechanism, while the broader component seen in both D- and H-atom channels was ascribed to an insertion-like process. The broader component looked strikingly similar to a statistical distribution, although the relative intensity of the broad

components in the H- and D-atom channels was not in accord with a statistical breakup (from a trigonal planar configuration). While physically intuitive, this simple picture is not adequate to explain the more comprehensive data set now available for reactive quenching that encompasses three isotopic variants: OH $A\ ^2\Sigma^+ + H_2$, OH $A\ ^2\Sigma^+ + D_2$, and OD $A\ ^2\Sigma^+ + H_2$. A somewhat different picture emerges as detailed below.

We start by comparing the H/D product translational energy distributions from reactive quenching in the OD $A\ ^2\Sigma^+ + H_2$ system with those reported previously and reanalyzed here for OH $A\ ^2\Sigma^+ + D_2$ (Figure 4). The H- and D-atom product channels, with the departing atomic product originating from OH/D or H_2/D_2, can be separately characterized in these partially deuterated systems, but are not distinguishable from one another for the fully hydrogenated (or deuterated) system. In both systems, the dominant reactive quenching pathway is identified as the H/D products originating from H_2/D_2 with a HOD co-product, accounting for 75% of the reactive quenching products from OD $A\ ^2\Sigma^+ + H_2$ and 60% of the products from OH $A\ ^2\Sigma^+ + D_2$. These H/D products have very similar translational energy distributions, as seen in the left panels of Figure 4. In both cases, the H/D products exhibit a highly peaked distribution at low translational energy (below 0.5 eV) with a long tail extending to the energetic limit. These $P(E_T)$ distributions can be represented essentially equally well by either one or the sum of two lognormal distributions, indicating that these $P(E_T)$ distributions cannot be separated into two distinct components. In addition, both release about 10% of the available energy as translation of the products.

The alternate pathways for quenching, OD $A\ ^2\Sigma^+ + H_2 \rightarrow D + H_2O$ and OH $A\ ^2\Sigma^+ + D_2 \rightarrow H + D_2O$, with the H/D product originating from OH/D accounts for 25% and 40% of reactive quenching events, respectively, also give rise to $P(E_T)$ distributions that are similar to one another as shown in the right panels of Figure 4. The $P(E_T)$ distributions for these alternate pathways suggest a small peak at low translation energy (below 0.5 eV) with a distinctive secondary peak at higher translational energy (approximately 1.6-1.8 eV) in both systems. In both cases, about 20% of the available energy is deposited into product translational energy.

These alternative pathways for quenching are attributed to an insertion-like mechanism since the O from OD (or OH) appears to insert into the H_2 (or D_2) bond to form $D + H_2O$ (or $H + D_2O$) products. A distinctive peak at higher E_T is seen in both cases for the insertion-like mechanism. This secondary peak is not evident in the dominant product channel, although a broad tail is observed. We are unable to determine whether or not the $P(E_T)$ distribution for the dominant product channel has a contribution from an insertion-like mechanism. We note that Davis and coworkers attributed the D-atom products detected upon quenching OH $A\ ^2\Sigma^+ + D_2$ at higher collision energy to a direct abstraction mechanism, suggesting that the dominant product channel in the present experiments is also due to abstraction.

Adding together the $P(E_T)$ distributions for H- and D-atom products arising from OD $A\ ^2\Sigma^+ + H_2$ or OH $A\ ^2\Sigma^+ + D_2$ yield total $P(E_T)$ distributions which are similar to that found for the OH $A\ ^2\Sigma^+ + H_2$ distribution (Figure 4). In OH $A\ ^2\Sigma^+ + H_2$, there is a narrow peak at low E_T (below 0.5 eV), which is also seen for the isotopic variants studied. A

higher energy secondary peak is also evident at 2.6 eV in the $P(E_T)$ distribution for OH $A\ ^2\Sigma^+ + H_2$, which is similar to that found for the insertion-like pathways of the isotopically substituted systems. For OH $A\ ^2\Sigma^+ + H_2$, however, the secondary peak is shifted by ~0.8 eV to higher energy than observed for the partially deuterated variants.

For comparison, the product translational energy distributions for the OD $A\ ^2\Sigma^+ + H_2$ system are also computed for a statistical model.[38] This model assumes complete randomization of vibrational energy in the OD-H_2 reactant pair and that the probability of forming product pairs with a particular translational energy $P(E_T)$ is proportional to the total density of states. The density of vibrational states, $N(E_v)$, is evaluated from a direct count of the HOD or H_2O product vibrational states including anharmonicity.[39] The total density of product states is then obtained by multiplying by the three-dimensional translational density of states for the recoiling products $E_T^{1/2}$, where $E_T + E_v = E_{avail}$, giving $P(E_T) = N(E_v)E_T^{1/2}$. The resultant statistical $P(E_T)$ distributions for the H and D-atom product channels are quite similar to one another because the $E_T^{1/2}$ term dominates at higher energy where the $N(E_v)$ distributions for HOD and H_2O differ most significantly from one another. The statistical $P(E_T)$ distributions, normalized to a peak of unity, are shown in Figure 5. (Similar results for the OH $A\ ^2\Sigma^+ + H_2/D_2$ systems were presented in Ref. 22.) Neither the peak position (0.8 eV) nor the broad spread of the statistical $P(E_T)$ distribution are in good accord with the $P(E_T)$ distributions obtained from H- and D-atom Doppler profiles, indicating that reactive quenching is a nonstatistical process.[40]

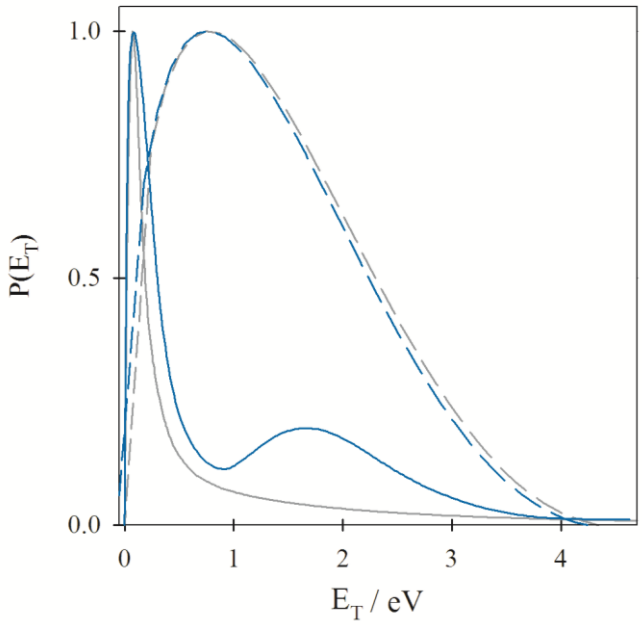

Figure 5. Product translational energy distributions $P(E_T)$ for OD $A\ ^2\Sigma^+ + H_2 \rightarrow$ H (gray) + HOD and OD $A\ ^2\Sigma^+ + H_2 \rightarrow$ D (blue) + H_2O channels derived from experiment represented as smooth curves based on lognormal distribution functions. Statistical distributions (dashed) are computed using the density of vibrational states for the HOD or H_2O products. The distributions are normalized to a peak of unity.

Given the similarities noted above in the $P(E_T)$ distributions for the systems studied by Doppler spectroscopy (Figure 4) and the limited availability of other experimental measurements and theory, we focus our comparisons on one isotopic variant, namely OH $A\ ^2\Sigma^+ + D_2$. Davis and coworkers obtained the $P(E_T)$ distribution shown in Figure 6 for the D + HOD products from a direct abstraction reaction based on their crossed-molecular beam scattering experiments at an average collision energy of 0.16 eV.[20] Their $P(E_T)$ distribution is peaked at higher energy, 0.55 eV, and is relatively broad compared to that deduced from Doppler spectroscopy. Note that the latter experiments were carried out at a much lower collision energy of ~0.005 eV in the collisional region of a supersonic expansion.

There is already abundant evidence showing that quenching of OH $A\ ^2\Sigma^+$ by H_2 and other collision partners is strongly dependent on collision energy. Early kinetics studies identified a trend of decreasing cross section with increasing temperature for many molecular quenchers, which was attributed to an attractive interaction between OH $A\ ^2\Sigma^+$ and the molecular collision partner.[2-7] More recently, Han and coworkers obtained this same trend in their nonadiabatic quantum reactive scattering calculations for OH $A\ ^2\Sigma^+ + H_2/D_2$.[23,24] They found reactive quenching to be the dominant process, yet the calculated integral cross section for reactive quenching decreased with increasing collision energy in the 0.06 to 0.40 eV range examined. The cross section for nonreactive quenching was essentially unchanged over this range, although one should note that the OH $X\ ^2\Pi$ product state distribution changes, the former indicating that the branching to reactive quenching will decrease with increasing collision energy. They have not yet

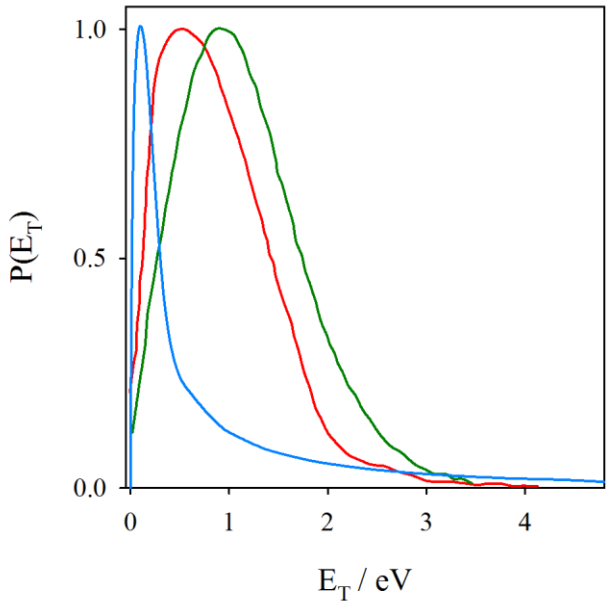

Figure 6. Product translational energy distributions $P(E_T)$ for the dominant OH $A\ ^2\Sigma^+$ + $D_2 \rightarrow D + HOD$ channel. The reanalyzed $P(E_T)$ distribution from Doppler profiles (blue, Ref. 22) is compared with that from crossed molecular beam experiments (red, Ref. 20). The theoretical $P(E_T)$ distribution from trajectory calculations (green, Ref. 17) initiated at representative points along the seams of conical intersection is also shown. The distributions are normalized to a peak of unity.

reported the product translational energy distribution resulting from reactive quenching or its collision energy dependence. Clearly, there is a complicated relationship between the quenching cross section, branching fraction, and the collision energy. We speculate that the change in the $P(E_T)$ distributions obtained at 0.005 and 0.16 eV in experimental studies (Figure 6) may be related to the same phenomenon; alternatively, the different $P(E_T)$ distributions may arise from some as yet unknown experimental source.

Bowman and coworkers have predicted $P(E_T)$ distributions resulting from reactive quenching of OH $A\ ^2\Sigma^+$ by H_2 and D_2 based on quasiclassical trajectory calculations.[17,18] The trajectories were initiated at equally weighted representative points along the seams of conical intersection, rather than the OH $A\ ^2\Sigma^+ + D_2$ reactant asymptote, with an energy of 4.46 eV for zero total angular momentum. The initial momenta were sampled both fully and partially microcanonically, corresponding to models for the postquenching dynamics termed 'adiabatic' and 'diabatic' (with the additional constraint that $\dot{R}(0)$ is negative), with the latter in better accord with the experimental branching ratios. The resultant $P(E_T)$ distribution for the D + HOD abstraction channel is reproduced in Figure 6.[17] The computed translational energy distribution peaks at 0.8 eV, which is somewhat higher in energy but similar in breadth to that observed experimentally by Davis and coworkers. Both peak at higher energy and are broader than the $P(E_T)$ distribution obtained from Doppler spectroscopy. The calculated $P(E_T)$ distribution for full trajectories originating from the OH $A\ ^2\Sigma^+ + D_2$ reactant asymptote and its dependence on collision energy has not yet been explored.

The predicted $P(E_T)$ distribution from trajectory calculations for the minor OH $A\ ^2\Sigma^+ + D_2 \rightarrow H + D_2O$ channel (insertion) is peaked at slightly higher energy (1.2 eV) than that for the dominant channel producing D + HOD (abstraction) (see Fig. 15 of Ref. 17). In the case of OH $A\ ^2\Sigma^+ + H_2$, the calculations indicate an even larger shift in the peak of the $P(E_T)$ distribution for insertion vs. abstraction (see Fig. 10 of Ref. 17). One can anticipate similar results from trajectory calculations for OD $A\ ^2\Sigma^+ + H_2$. Experimentally, the secondary peak in the $P(E_T)$ distribution attributed to an insertion-like process is shifted to higher energy for OH $A\ ^2\Sigma^+ + H_2$ compared to OH $A\ ^2\Sigma^+ + D_2$, consistent with the trend seen in trajectory calculations. The secondary peak observed for OD $A\ ^2\Sigma^+ + H_2$ is similar to that for OH $A\ ^2\Sigma^+ + D_2$.

In the experimental studies, a large percentage of the reactive quenching events occur through an insertion-like process. In the quasiclassical trajectory calculations, the insertion channel accounts for only 1-2% of the reactive quenching outcomes. The origin of this discrepancy is not known. It is interesting to note, however, that the branching ratio for the abstraction to insertion pathways differs for trajectories initiated from T-shaped HO-H_2 vs. linear HO-HH configurations at the CI. Specifically, C_{2v} configurations yield 97.7% abstraction, while $C_{\infty v}$ configurations result overwhelmingly in abstraction (99%).[17] This suggests that insertion is more likely to occur from T-shaped HO-H_2 configurations than other orientations of the reactants at the CI. Furthermore, it is difficult to envision how a linear HO-HH configuration at the CI might lead directly to insertion products. Thus, we speculate that quenching dynamics originating from the OH

$A\ ^2\Sigma^+ + H_2$ asymptote may sample C_{2v} CI configurations more heavily than suggested by equal weighting of representative points along the seams of conical intersection.

Trajectory calculations also indicate that the water products from reactive quenching of OH $A\ ^2\Sigma^+$ by H_2 will be produced primarily with high bend excitation (up to v_b=19) and a much smaller degree of asymmetric and/or symmetric stretch excitation.[17,18] Similar results were predicted for HOD produced from OH $A\ ^2\Sigma^+ + D_2$.[17] Experimentally, collisional quenching of OH $A\ ^2\Sigma^+$ by H_2 and its isotopic variants yield products with low translational energy on average (see Table S1).[37] This corresponds to a very high degree of internal excitation of the water products, but not sufficient energy to lead to dissociation of the water products.

A simple comparison of HO-H_2 configurations at representative points along the seams of conical intersections[25] with the equilibrium geometry of water provides a qualitative explanation for the high degree of internal excitation of the water products. In a direct reactive quenching process, linear $C_{\infty v}$ or near-linear configurations at the CI would lead to H-atom abstraction, but likely not insertion. Water products would emerge from the CI with highly extended H-O-H bond angles, far from the equilibrium angle, resulting in a large degree of bending excitation. Similarly, C_{2v} HO-H_2 configurations at the CI would lead to water products from an abstraction process with extended H-O-H bond angles (159-165°), again resulting in a large degree of bending excitation. In both of these abstraction processes, the one newly formed O-H bond (1.47-1.64 Å) is elongated at the CI compared to its equilibrium bond length, possibly leading to excitation of the asymmetric stretching mode. For HO-H_2 C_{2v} configurations leading to

insertion, the water product would emerge from the CI with a highly compressed bond angle (29-42°), once again resulting in large bending excitation. In this case, both of the newly formed O-H bonds would be significantly longer than their equilibrium bond lengths, which could lead to symmetric stretching excitation. These simple geometric based arguments are consistent with the large internal excitation found experimentally and the large amount of bending excitation predicted in trajectory calculations.[17,18]

V. Conclusions

This paper extends the investigation of outcomes following collisional quenching of OH $A\ ^2\Sigma^+ + H_2$ and its isotopic variants in this laboratory.[12, 13-15,21, 22] A recent study of nonreactive quenching for OD $A\ ^2\Sigma^+ + H_2$ characterized the quantum state distribution of the OD $X\ ^2\Pi$ (v=0,1) products, yielding extensive rotational excitation and a strong $\Pi(A')$ Λ-doublet selectivity, and deduced the branching fraction for OD $X\ ^2\Pi$ products of 19.6 ± 3.6%.[19] This work focuses on the dominant reactive quenching process for OD $A\ ^2\Sigma^+ + H_2$, which results in H + HOD and D + H_2O products with an H:D ratio of 3:1 based on the integrated areas of the Doppler profiles. Combining these results yields the following as the most significant outcomes following collisional quenching:

$$\begin{aligned} \text{OD } A\ ^2\Sigma^+ + H_2 &\rightarrow \text{OD } X\ ^2\Pi + H_2 \ (20\%) \\ &\rightarrow H + HOD \ (60\%) \\ &\rightarrow D + H_2O \ (20\%) \end{aligned}$$

Transformation of the Doppler profiles into product translational energy distributions reveals substantial differences between the $P(E_T)$ distributions for the H- and D-atom channels. The H-atom channel is strongly peaked at low translational energy

(below 0.5 eV) with a long tail extending to the energetic limit. By contrast, the D-atom channel has only a small peak at low translational energy with a relatively broad, yet distinctive secondary peak at 1.8 eV before falling off to higher energy. Reanalysis of earlier data obtained for quenching of OH $A\ ^2\Sigma^+$ by D_2 shows remarkably similar product ratios and $P(E_T)$ distributions for the D + HOD and H + D_2O channels as those obtained for OD $A\ ^2\Sigma^+ + H_2$. Further, reanalysis of Doppler profiles for quenching of OH $A\ ^2\Sigma^+$ by H_2 gives a $P(E_T)$ distribution that resembles the sum of those obtained for the H- and D-atom channels, although with a clearly noticeable secondary peak at somewhat higher energy (2.6 eV) compared to the partially deuterated systems where it is ascribed to an insertion-like process. For all isotopic variants, product translation accounts for only a small amount of the available energy. The balance of the available energy is funneled into the internal excitation of the water product. Simple geometric arguments and trajectory calculations suggest a high degree of water bend excitation.

There is now an extensive experimental data set on the reactive and nonreactive outcomes of collisional quenching for OH $A\ ^2\Sigma^+ + H_2$ and two of its isotopic variants. Full dimensional coupled dynamics on the relevant potential energy surfaces are still needed to fully understand the nonadiabatic dynamics. Ongoing work in this laboratory is focused on exploring reactive quenching outcomes from collisions of OH $A\ ^2\Sigma^+$ with molecular partners of importance in atmospheric and combustion environments.

Acknowledgements

The research was conducted at the University of Pennsylvania and supported by the Office of Basic Science of the Department of Energy. J.H.L and M.I.L. thank Joe Beames (UPenn) and Craig Murray (Glasgow) for helpful discussions.

Acknowledgement is made to the Donors of the American Chemical Society Petroleum Research Fund for partial support of this research (J.L.B. and T.A.S).

References

1 D. R. Crosley, Advanced Series in Physical Chemistry **3**, 256 (1995).
2 R. A. Copeland, M. J. Dyer, and D. R. Crosley, J. Chem. Phys. **82**, 4022 (1985).
3 D. R. Crosley, J. Phys. Chem. **93**, 6273 (1989).
4 D. J. Creasey, D. E. Heard, M. J. Pilling, B. J. Whitaker, M. Berzins, and R. Fairlie, Appl. Phys. B: Lasers Opt. **65**, 375 (1997).
5 D. E. Heard and D. A. Henderson, Phys. Chem. Chem. Phys. **2**, 67 (2000).
6 B. L. Hemming, D. R. Crosley, J. E. Harrington, and V. Sick, J. Chem. Phys. **115**, 3099 (2001).
7 B. L. Hemming and D. R. Crosley, J. Phys. Chem. A **106**, 8992 (2002).
8 P. W. Fairchild, G. P. Smith, and D. R. Crosley, J. Chem. Phys. **79**, 1795 (1983).
9 H. M. Lin, M. Seaver, K. Y. Tang, A. E. W. Knight, and C. S. Parmenter, J. Chem. Phys. **70**, 5442 (1979).
10 P. H. Paul, J. Quant. Spectrosc. Radiat. Transfer **51**, 511 (1994).
11 A. E. Bailey, D. E. Heard, D. A. Henderson, and P. H. Paul, Chem. Phys. Lett. **302**, 132 (1999).
12 D. T. Anderson, M. W. Todd, and M. I. Lester, J. Chem. Phys. **110**, 11117 (1999).
13 P. A. Cleary, L. P. Dempsey, C. Murray, M. I. Lester, J. Kłos, and M. H. Alexander, J. Chem. Phys. **126**, 204316 (2007).
14 L. P. Dempsey, C. Murray, P. A. Cleary, and M. I. Lester, Phys. Chem. Chem. Phys. **10**, 1424 (2008).
15 L. P. Dempsey, C. Murray, and M. I. Lester, J. Chem. Phys. **127**, 151101 (2007).
16 L. P. Dempsey, T. D. Sechler, C. Murray, M. I. Lester, and S. Matsika, J. Chem. Phys. **130**, 104307 (2009).
17 B. Fu, E. Kamarchik, and J. M. Bowman, J. Chem. Phys. **133**, 164306 (2010).
18 E. Kamarchik, B. N. Fu, and J. M. Bowman, J. Chem. Phys. **132**, 091102 (2010).
19 J. H. Lehman, L. P. Dempsey, M. I. Lester, B. Fu, E. Kamarchik, and J. M. Bowman, J. Chem. Phys. **133**, 164307 (2010).

[20] M. Ortiz-Suárez, M. F. Witinski, and H. F. Davis, J. Chem. Phys. **124**, 201106 (2006).
[21] I. B. Pollack, Y. X. Lei, T. A. Stephenson, and M. I. Lester, Chem. Phys. Lett. **421**, 324 (2006).
[22] M. W. Todd, D. T. Anderson, and M. I. Lester, J. Phys. Chem. A **105**, 10031 (2001).
[23] P. Y. Zhang, R. F. Lu, T. S. Chu, and K. L. Han, J. Chem. Phys. **133**, 174316 (2010).
[24] P. Y. Zhang, R. F. Lu, T. S. Chu, and K. L. Han, J. Phys. Chem. A **114**, 6565 (2010).
[25] B. C. Hoffman and D. R. Yarkony, J. Chem. Phys. **113**, 10091 (2000).
[26] D. R. Yarkony, J. Chem. Phys. **111**, 6661 (1999).
[27] M. I. Lester, R. A. Loomis, R. L. Schwartz, and S. P. Walch, J. Phys. Chem. A **101**, 9195 (1997).
[28] J. M. Bowman, G. Czako, and B. Fu, Phys. Chem. Chem. Phys. **13**, 8094 (2011).
[29] C. L. Cesar, D. G. Fried, T. C. Killian, A. D. Polcyn, J. C. Sandberg, I. A. Yu, T. J. Greytak, D. Kleppner, and J. M. Doyle, Phys. Rev. Lett. **77**, 255 (1996).
[30] T. W. Hansch, S. A. Lee, R. Wallenstein, and C. Wieman, Phys. Rev. Lett. **34**, 307 (1975).
[31] A. A. Turnipseed, G. L. Vaghjiani, J. E. Thompson, and A. R. Ravishankara, J. Chem. Phys. **96**, 5887 (1992).
[32] M. Alagia, N. Balucani, P. Casavecchia, D. Stranges, G. G. Volpi, D. C. Clary, A. Kliesch, and H. J. Werner, Chem. Phys. **207**, 389 (1996).
[33] J. Luque and D. R. Crosley, SRI International Report MP 99-009 (1999).
[34] G. W. Johnston, H. Kornweitz, I. Schechter, A. Persky, B. Katz, R. Bersohn, and R. D. Levine, J. Chem. Phys. **94**, 2749 (1991).
[35] M. W. Chase, J. L. Curnutt, J. R. Downey, R. A. McDonald, A. N. Syverud, and E. A. Valenzuela, J. Phys. Chem. Ref. Data **11**, 695 (1982).
[36] R. N. Zare and D. R. Herschbach, Proc. IEEE **51**, 173 (1963).
[37] See supplementary information at http://dx.doi.org/10.1063/1.3644763for additional information on the analysis procedure and a table compiling experimental and theoretical results. This is also included in Appendix I of this thesis.
[38] M. N. R. Ashfold, R. N. Dixon, M. Kono, D. H. Mordaunt, and C. L. Reed, Philos. Trans. R. Soc. Lond. Ser. A-Math. Phys. Eng. Sci. **355**, 1659 (1997).
[39] N. Gailar and E. K. Plyler, J. Chem. Phys. **24**, 1139 (1956).
[40] This differs from the prior analysis for OH A $^2\Sigma^+$ + D_2, where the broad components of the H/D P(E_T) distributions were interpreted as being similar to statistical distributions.[22]

CHAPTER 4
Reactive quenching of OH $A\ ^2\Sigma^+$ by O_2 and CO: Experimental and nonadiabatic theoretical studies of H- and O-atom product channels

The experimental research presented in this chapter was performed at the University of Pennsylvania, and the theoretical calculations were performed at Johns Hopkins University. This research has been published as a paper in the *Journal of Chemical Physics*.

Reference: J. H. Lehman, M. I. Lester, D.R. Yarkony, *J. Chem. Phys.*, **137**, 094312 (2012).

I. Introduction

Extensive kinetics studies have shown that electronically excited OH $A\ ^2\Sigma^+$ radicals are efficiently quenched in collisions with molecular partners. Quenching of OH $A\ ^2\Sigma^+$ can cause OH to be returned to its ground $X\ ^2\Pi$ electronic state (nonreactive quenching) or result in formation of new products (reactive quenching). Previous experiments in this laboratory have focused on characterizing aspects of the nonreactive quenching pathway for OH $A\ ^2\Sigma^+$ with molecular partners such as H_2, N_2, O_2, and CO_2.[1-5] For each of these partners, the OH $X\ ^2\Pi$ product state distribution was mapped out and the branching fraction to nonreactive quenching was determined. The branching fraction varied substantially across these molecular partners. Specifically, the nonreactive pathway was found to be the dominant quenching outcome with N_2 as a collision partner, accounting for 88(5)% of products. However, in collisions with H_2, OH $X\ ^2\Pi$ ($v'' = 0, 1, 2$) population accounts for only 12(5)% of products, indicating that nonreactive quenching is the minor pathway. With O_2 and CO_2 as collision partners, the quenching outcomes were split fairly evenly between nonreactive and reactive pathways.

For collisions of OH $A\ ^2\Sigma^+$ with H_2 and its isotopic variants, reactive quenching is the dominant pathway, 88(5)%, yielding H + H_2O products; the H-atom branching fraction will be utilized in the present study. In this laboratory, the H/D-atom products have been probed directly via Doppler spectroscopy, revealing that most of the available energy results in internal excitation of the water products.[6-8] In partially deuterated systems, OD $A\ ^2\Sigma^+ + H_2$ and OH $A\ ^2\Sigma^+ + D_2$, both H- and D-atom products are observed, with some notable differences in their translational energy distributions. The

translational and angular distributions of the D-atom products from OH $A\ ^2\Sigma^+ + D_2$ were also obtained under crossed molecular beam conditions by Davis and coworkers, which indicated a direct reaction.[9]

For quenching of OH $A\ ^2\Sigma^+$ by O_2, previous kinetics studies determined a cross section of $\sigma_Q \sim 12$ Å^2 at 298K, which increases at lower temperatures.[10] As shown in Figure 1, several possible product channels are energetically accessible:

$$\begin{aligned}
\text{OH } A\ ^2\Sigma^+ + O_2\ X\ ^3\Sigma_g^- &\rightarrow \quad \text{OH } X\ ^2\Pi + O_2\ X\ ^3\Sigma_g^- && \Delta E = -4.02 \text{ eV} \\
&\rightarrow \quad H\ ^2S + O_3\ X\ ^1A_1 && \Delta E = -0.68 \text{ eV} \\
&\rightarrow \quad O\ ^3P + HO_2\ X\ ^2A'' && \Delta E = -1.69 \text{ eV} \\
&\rightarrow \quad O\ ^3P + HO_2\ A\ ^2A' && \Delta E = -0.82 \text{ eV}
\end{aligned}$$

Note that excited electronic states of O_2 ($a\ ^1\Delta_g$, $b\ ^1\Sigma_g^+$) may be produced, but cannot be distinguished in this (or prior) work.

The quantum state distribution and branching fraction for OH $X\ ^2\Pi$ products following nonreactive quenching with O_2 were previously reported.[3] The OH $X\ ^2\Pi$ products were generated with a substantial amount of rotational excitation, peaking at N'' = 17 with $\langle E_{rot} \rangle$ = 4780(190) cm^{-1}. Products were found predominantly in v'' = 0 with less population in v'' = 1. The branching fraction measurement showed that 40(1)% of quenching results in OH $X\ ^2\Pi$ (v'' = 0,1) products. This indicates that one or more of the reactive channels above are likely to be significant outcomes. We probe both the H- and O-atom product channels in this work without, however, distinguishing between $HO_2\ X\ ^2A''$ and $A\ ^2A'$ co-products. Note that normal (bent) $O_3\ X\ ^1A_1$ is the co-product in the other reactive quenching channel; cyclic ozone would not be energetically accessible.[11]

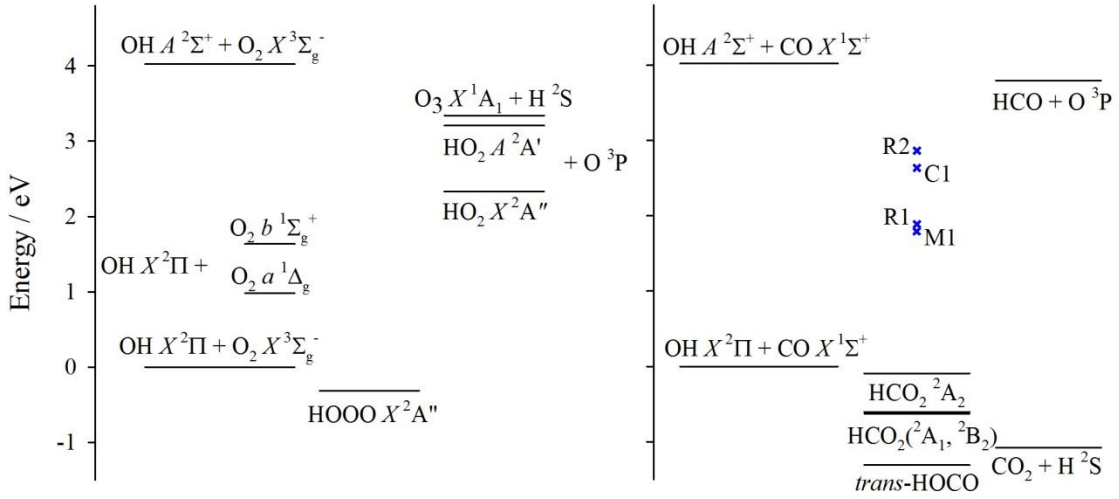

Figure 1. Schematic energy level diagrams for quenching of initially prepared OH $A\,^2\Sigma^+$ in collisions with O_2 (left panel) and CO (right panel). Nonreactive quenching collisions with either partner returns OH to its ground $X\,^2\Pi$ state. For O_2, reactive quenching could generate HO_2 + O and O_3 + H products, whereas in collisions with CO, reactive quenching could produce CO_2 + H and HCO + O products. The energy minimized crossings for four conical intersections characterized in this study are indicated (×). Possible intermediates are also shown.

For quenching of OH $A\,^2\Sigma^+$ by CO, prior kinetics studies indicate σ_Q is ~35 Å^2 at 298 K, twice that for O_2, which increases with decreasing temperature as well.[10,12] This system also has multiple energetically accessible product channels, shown in Figure 1:

$$\text{OH } A\,^2\Sigma^+ + \text{CO } X\,^1\Sigma^+ \rightarrow \quad \text{OH } X\,^2\Pi + \text{CO } X\,^1\Sigma^+ \qquad \Delta E = -4.02 \text{ eV}$$

$$\rightarrow \quad \text{H } ^2S + \text{CO}_2\, X\,^1\Sigma_g^+ \qquad \Delta E = -5.07 \text{ eV}$$

$$\rightarrow \quad \text{O } ^3P + \text{HCO } X\,^2A' \qquad \Delta E = -0.23 \text{ eV}$$

We examine the reactive quenching channels yielding H- and O-atom products as well as the nonreactive quenching to OH $X\,^2\Pi$ ($v'' = 0,1$) products in this study.

No theoretical work has been reported to date on quenching of OH $A\,^2\Sigma^+$ by O_2; the experimental results reported here will hopefully stimulate such studies. There is an extensive body of literature on important atmospheric reactions connecting H + O_3 and O + HO_2 to OH products in their ground $X\,^2\Pi$ electronic state.[13-17] The hydrogen trioxide (HOOO) radical has been inferred as an important intermediate in many of these processes, prompting much experimental and theoretical work.[18,19] The possible role of the ground and/or excited electronic states of the HOOO radical in the quenching of OH $A\,^2\Sigma^+$ by O_2 is unknown.

Some prior theoretical information is available on quenching of OH $A\,^2\Sigma^+$ by CO. Vegiri and Farantos carried out electronic structure calculations and classical trajectory studies over twenty years ago to try to shed some light on the mechanism for the efficient quenching of OH $A\,^2\Sigma^+$ by CO.[20,21] This earlier work mapped out regions of the excited state surface, in most cases constraining the OH and CO bond lengths to their ground electronic state equilibrium values, while varying the distance and angles between the

partners. Derivative coupling matrix elements obtained from configuration interaction wave functions provided the coupling between surfaces. They identified four regions of strong nonadiabatic interaction, which are further investigated in this work using modern algorithms to search for conical intersections; we adopt the same labeling scheme as that used previously. Region C1 has a conical intersection (CI) between the OH ($A\,^2\Sigma^+$, $X\,^2\Pi$) + CO potential energy surfaces in a linear HO – CO configuration (at an energy ~1.3 eV below the excited state asymptote and OH to CO center-of-mass separation of ~2.6 Å). An avoided crossing was found in region M1 and identified as having the deepest minimum (1.89 eV below the excited state asymptote). Region M1 is similar to the linear C1, but has the H-atom rotated from the linear O – CO by 70° and a center-of-mass separation of 2.0 Å. Region R1, another region identified with strong nonadiabatic coupling, was characterized as having both OH and CO rotated from a linear configuration, in a cis-like geometry, with a center-of-mass separation of 1.7 Å. These three regions have a common theme of the O-atom of OH pointing toward the CO moiety.

A final region (R2) identified with strong nonadiabatic coupling has the H-atom of OH pointing toward CO with a center-of-mass distance of 2.3 Å. This region was proposed as the most important pathway for quenching based on classical trajectory calculations of quenching cross sections, possibly leading to a C_{2v} configuration of the formyloxyl radical (HCO_2). Presumably, if the HCO_2 radical is formed, it would undergo predissociation, since HCO_2 is unstable with respect to dissociation to H + CO_2 by 0.52 eV as determined by anion photodetachment studies.[22,23] New theoretical work presented

here on the OH + CO system identifies energy minimized conical intersections within all four regions of strong nonadiabatic coupling and connects characteristics of the CIs in these regions to experimental observables.

The linear OH – CO configuration was also found to have a CI, although it is located 0.4 eV above the OH $A\ ^2\Sigma^+$ + CO asymptote, which is too high to be relevant in the experimental studies in this work. Nevertheless, to provide a comprehensive view of prior work, we note that theory predicts an attractive long range interaction between OH $A\ ^2\Sigma^+$ and CO in the linear OH – CO configuration,[21] which has been accessed via electronic spectroscopy in the OH *A*-*X* (1,0) region starting from a linear OH-CO complex prepared in its ground electronic state.[24] The electronically excited OH-CO complex [correlating with OH $A\ ^2\Sigma^+$ ($v' = 1$) + CO] rapidly decayed via vibrational predissociation or possibly quenching.

More extensive theoretical calculations have been performed on the benchmark OH ($A\ ^2\Sigma^+$, $X\ ^2\Pi$) + H_2 system, where ab initio methods have been used to identify seams of conical intersection that couple the upper and lower adiabatic surfaces of A′ symmetry when the oxygen side of OH points toward H_2.[25,26] For these configurations, there is a barrierless pathway from OH $A\ ^2\Sigma^+$ + H_2 to OH $X\ ^2\Pi$ + H_2 or H + H_2O products. The strong OH angular anisotropy of the surfaces has been linked qualitatively to experimental observables.[1] Recently, classical trajectory studies of the post-quenching dynamics[5,27,28] and nonadiabatic quantum reactive scattering studies[29,30] have provided the first dynamical studies of the outcomes. The predicted OH $X\ ^2\Pi$ product state distribution following nonreactive quenching compares favorably to experiment.

Reactive quenching is predicted to be the dominant pathway, in accord with experiment, while the calculated branching fraction depends on the sampling method (and initial kinetic energy) and differs to some extent from that experimentally determined. Most recently, a more rigorous theoretical treatment that includes fully coupled quantum dynamics on diabatic surfaces is being applied to this system.[31,32] The large ensemble of literature available on the OH + H_2 system enables experiment and theory to gain insight into the quenching mechanism.

This paper focuses on identifying the major product channels following reactive quenching of OH $A\ ^2\Sigma^+$ by O_2 and CO. In addition, this study examines the kinetic energy release and/or quantum state distributions of the products, providing some insight on the nonadiabatic dynamics. The branching between nonreactive and multiple reactive quenching channels gives significant new information on the mechanism. New theoretical work is also presented on concial intersection regions that give rise to quenching of OH $A\ ^2\Sigma^+$ by CO, building on the earlier work by Vegiri and Farantos and complementing the experimental study.

II. Experimental Methods

The experimental methods are similar to those previously reported in studies of reactive quenching of OH/D $A\ ^2\Sigma^+$ by H_2/D_2.[6-8] Briefly, OH $X\ ^2\Pi$ radicals are generated in the throat of a pulsed supersonic jet expansion by photolyzing nitric acid (98% fuming) at 193 nm. The nitric acid vapor is entrained in a gas mixture of the quenching partner and helium, specifically 20% O_2/He, 20% CO/He, or 30% H_2/He, with a backing pressure

between 40 and 60 psi. The OH radicals are excited on the $P_1(1)$ line of the $A\ ^2\Sigma^+$ - $X\ ^2\Pi$ (0,0) transition with the UV pump laser operating at 308 nm. The pump laser induced fluorescence (LIF) is collected with a photomultiplier tube (PMT, ET Enterprises 9813Q) using a 308 nm bandpass filter.

Several probe laser schemes are used for these experiments. In the first, the probe laser at 243 nm is generated by frequency doubling (BBO) the output of a Nd:YAG (355 nm) pumped dye laser (Coumarin 480, 2-3 mJ, 7 ns). This scheme is used to monitor the production of H-atoms via a 2-photon transition ($2\ ^2S \leftarrow\leftarrow 1\ ^2S$), as previously reported.[6-8] The effective two-photon laser linewidth is 0.5 cm^{-1}. A solar blind PMT (ET Enterprises 9403B) with a notch filter centered at 121.5 nm collects the resulting Lyman-α fluorescence. In the second scheme, the probe laser at 226 nm is generated by frequency doubling (BBO) the output of a Nd:YAG (355 nm) pumped dye laser (Coumarin 450, 1-2 mJ, 7 ns). This setup is used to monitor the production of O (^3P_J) atoms via a 2-photon transition ($3p\ ^3P \leftarrow\leftarrow 2p\ ^3P$). A red-sensitive PMT (Hamamatsu R955) with two longpass filters collects the resulting fluorescence from $3p\ ^3P$ to $3s\ ^3S$ (~845 nm) as well as any O-atoms that undergo intersystem crossing from $3p\ ^3P$ to $3p\ ^5P$ and fluoresce to $3s\ ^5S$ (~778 nm).[33] The PMT signals were preamplified, processed with a digital storage oscilloscope (LeCroy WaveRunner 6050A) and transferred to a laboratory computer for further analysis.

The counter propagating pump and probe UV lasers are spatially overlapped and gently focused with 50 cm f.l. lenses. The laser beams intersect the collisional region of

the expansion at a distance x/D = 2, where D is the nozzle diameter. The probe UV laser is typically delayed by 50 ns with respect to the pump laser.

Background H- and O-atoms arise from the 193 nm photolysis of nitric acid[34,35] and possibly other sources. The background H- and O-atom signals seen in the O_2/He and CO/He gas mixtures are comparable in magnitude to those in pure helium carrier gas, indicating that photodissociation of nitric acid is the primary source. The ground state OH $X\,^2\Pi$ + O_2 and CO reactions do not contribute significantly to the H- or O-atom background signals due to the significant endothermicity and/or barrier along these reaction paths.

The background H-atoms are cooled significantly in the expansion and have typical Doppler widths of less than 1 cm^{-1} in the laser interaction region. Background O-atoms are observed primarily in their lowest fine-structure state (O 2p $^3P_2$), which accounts for approximately 90% of background O-atoms, with decreasing population in the higher energy O 2p $^3P_1$ and O 2p $^3P_0$ states. The background O-atom 2p ^3P_J fine structure distribution can be fit to a Boltzmann temperature of approximately 120 K.

An active background subtraction scheme, as described previously,[8] was used in data collection. Briefly, the pump laser (5 Hz) is operated at half the repetition rate of the probe laser (10 Hz). The background signal arising from the probe laser only is subtracted from the combined pump and probe laser induced signal. This scheme enables one to distinguish between the desired H- or O-atom signal arising from the combination of pump and probe lasers, and background signals originating from the probe laser only.

For a few experiments, the OH $X\ ^2\Pi$ products from nonreactive quenching are probed following quenching collisions of OH $A\ ^2\Sigma^+$ by CO. Similar studies have been reported previously with O_2 as the quenching partner.[3] In the present case, the OH $X\ ^2\Pi$ products are probed on various *A*-*X* transitions with vibrational (v''), rotational (N''), and fine-structure resolution using experimental methods similar to those previously reported.[1-4] Specifically, OH $X\ ^2\Pi$ ($v'' = 0,1$, $N'' \leq 20$) products are detected by probe laser excitation on the *A*-*X* (1,0) or (1,1) bands, with fluorescence from OH $A\ ^2\Sigma^+$ ($v' = 1$) collected on the *A*-*X* (1,0) band. OH $X\ ^2\Pi$ ($v'' = 0$, $N'' \geq 17$) products are excited and fluorescence is collected on the *A*-*X* (0,0) band.

III. Experimental Results

A. Quenching of OH $A\ ^2\Sigma^+$ by O_2 and CO

OH radicals prepared in the lowest rovibrational level (v'=0, N'=0) of the excited $A\ ^2\Sigma^+$ electronic state are quenched, albeit with somewhat different efficiencies, in collisions with O_2, CO, and H_2. The experimental conditions are adjusted slightly (using different backing pressures and gas mixtures in He, the latter being ineffective in quenching OH $A\ ^2\Sigma^+$) to achieve similar OH $A\ ^2\Sigma^+$ fluorescence lifetimes at the same x/D distance downstream. Collisions with O_2 in a 20% mixture at a total backing pressure of 50 psi reduce the OH $A\ ^2\Sigma^+$ fluorescence lifetime to approximately 150 ns. The OH $A\ ^2\Sigma^+$ fluorescence lifetime is similarly shortened to ~150 ns as a result of collisions with CO in a 20% mixture at a backing pressure of 40 psi. Finally, a 30% H_2 gas mixture at a backing pressure of 60 psi is used to reduce the OH $A\ ^2\Sigma^+$ lifetime to approximately 150

ns. In each case, the fluorescence lifetime is significantly shorter than the OH $A\ ^2\Sigma^+$ radiative lifetime of ~700 ns.[36]

A previous study in this laboratory on the nonreactive quenching of OH $A\ ^2\Sigma^+$ by O_2 determined the OH $X\ ^2\Pi$ (v''=0,1, N'') product state distribution and the branching fraction to OH $X\ ^2\Pi$ (v''=0,1). The nonreactive quenching pathway was found to account for 40(5)% of the outcomes, with the balance assumed to result in reaction.[3] An analogous study has since been carried out to identify OH $X\ ^2\Pi$ products following quenching of OH $A\ ^2\Sigma^+$ by CO. Despite clear evidence of quenching based on the shortened OH $A\ ^2\Sigma^+$ fluorescence lifetime, no OH $X\ ^2\Pi$ (v''=0,1, N'') products could be detected in the rovibrational levels probed. Specifically, the four fine structure components [$\Pi(A')$ and $\Pi(A'')$ Λ-doublet components of each rotational level in the F_1 and F_2 spin-orbit manifolds] of the OH $X\ ^2\Pi$ (v''=0, N''= 9, 12, 15, 18, 20, 24, 26) and (v''=1, N''=4, 6, 8, 12) rovibrational levels were probed. This indicates a negligible branching fraction to these OH $X\ ^2\Pi$ product states (less than 0.1% per product state) and suggests that quenching strongly favors reactive outcomes. While the possibility that quenching populates higher OH $X\ ^2\Pi$ ($v''\geq2$, N'') product states cannot be ruled out, such a result would be surprising given that the OH bondlength is essentially the same in the $A\ ^2\Sigma^+$ (1.01 Å) and $X\ ^2\Pi$ (0.97 Å) electronic states, and other quenching partners (H_2, N_2, O_2, and CO_2) yield minimal vibrational excitation of the OH $X\ ^2\Pi$ products.[2-4] Evidence presented below supports the assertion that reactive quenching is the dominant outcome.

B. H-atom Products of Reactive Quenching

Hydrogen atoms are detected following reactive quenching of OH $A\ ^2\Sigma^+$ by O_2 and CO, indicating that the H + O_3 and H + CO_2 product channels are open. The velocity distributions of the nascent H-atoms resulting from these reactive quenching channels are ascertained from Doppler profiles obtained by scanning the frequency of the probe laser. The Doppler profiles are recorded using the active background subtraction scheme previously described and averaged over several scans to improve the signal to noise ratio. The resulting Doppler profiles shown in Figure 2 are centered about the two photon transition at 82259.2 cm^{-1}. The active background subtraction procedure is highly effective in removing background H-atom signals, as evident from the minimal residual noise at the baseline with the pump laser blocked (Figure 2).

The energy available, E_{avail}, to the reaction products is given by $E_{avail} = E_{h\upsilon} - \Delta H_{rxn} + E_{coll}$, where $E_{h\upsilon}$ = 4.02 eV for the OH *A*-*X* (0,0) $P_1(1)$ transition, ΔH_{rxn} is the enthalpy associated with in the ground state OH $X\ ^2\Pi$ + O_2 or CO reaction,[37] and E_{coll}, the average collision energy, is ~ 0.025 eV.[38] Using conservation of energy and linear momentum, the maximum H-atom velocity is readily determined for the OH + O_2 system by

$$v_H^{\max} = \sqrt{\frac{2E_{avail}}{m_H\left(1+m_H/m_{O_3}\right)}}.$$

A similar equation is obtained for the OH + CO system. From the above equations, the maximum H-atom velocities are $v_H^{\max} = 1.14\times10^4$ m/s and $v_H^{\max} = 3.10\times10^4$ m/s, corresponding to maximum Doppler shifts of ±3.12 cm^{-1} and ±8.49 cm^{-1}, for the OH *A*

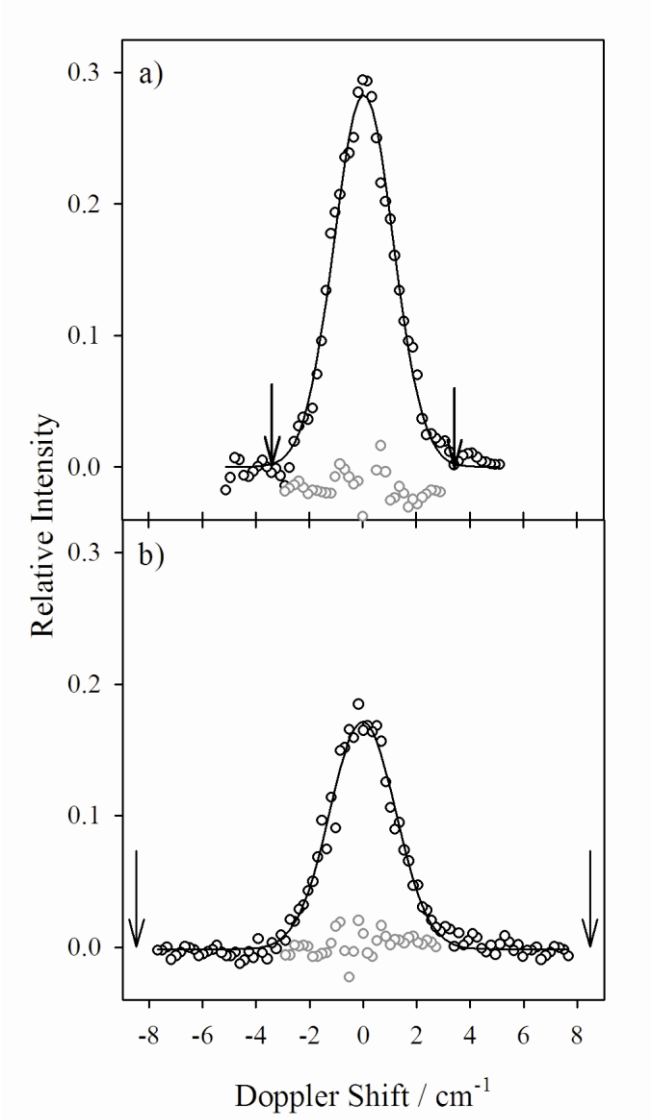

Figure 2. H-atom Doppler profiles of signals (○) produced in reactive quenching of OH $A\,^2\Sigma^+$ with (a) O_2 and (b) CO acquired with the active background subtraction scheme. The Doppler profiles are fit with a Gaussian function (solid line). The arrows indicate the maximum Doppler shifts assuming all of the available energy from the reaction going into the translational energy of the H-atom products. Also shown are the pump-laser blocked signals (○), illustrating the quality of the background subtraction.

$^2\Sigma^+ + O_2$ and OH $A\ ^2\Sigma^+$ + CO systems, respectively. The maximum Doppler shift is indicated in each panel of Figure 2 by a set of arrows.

The Doppler profiles are well-modeled by a Gaussian distribution as shown by the fit through the data in Figure 2. H-atom signal extends out to the maximum Doppler shift for the OH $A\ ^2\Sigma^+ + O_2$ system (±3.12 cm^{-1}), with a *fwhm* of 2.59(9) cm^{-1} derived from the Gaussian fit. For quenching of OH $A\ ^2\Sigma^+$ by CO, the H-atom signal, with a *fwhm* of 2.75(8) cm^{-1}, extends to Doppler shifts of approximately ±3.5 cm^{-1}. This is significantly less than the maximum Doppler shift associated with the energetic limit.

A Doppler profile is a one dimensional projection of a three dimensional distribution of velocities along the laser propagation axis. Only hydrogen atoms with zero velocity component along the laser propagation axis will absorb at the two-photon transition frequency, ν_0, of 82259.2 cm^{-1}. The Doppler shift from this central frequency is described by $\nu = \nu_0\left(1 \pm \frac{v}{c}\right)$, where v is the velocity, c is the speed of light, and ν is the Doppler shifted frequency. A Gaussian Doppler profile can be directly related to a translational temperature, T,[39] assuming a Boltzmann distribution

$$T = \frac{\left(\frac{fwhm}{2\nu_0}\right)^2 m_H c^2}{2k \ln 2}$$

where the *fwhm* (cm^{-1}) is the breadth of the Gaussian Doppler profile, m_H is the mass of the H-atom, and k is the Boltzmann constant. The *fwhm* and temperature of the fitted H-atom distributions are listed in Table 1. The H-atom distributions are assumed to be spatially isotropic because of the Gaussian form of the Doppler profile.[39] The quenching

Table 1. Parameters derived from the H-atom Doppler profiles obtained from the quenching of OH $A\ ^2\Sigma^+$ by O_2 and CO. The breadth of the profiles (*fwhm*), translational temperature (T), average H-atom translational energy ($\langle E_{T,H} \rangle$), average product translational energy ($\langle E_T \rangle$), and the fraction of available energy going into product translation ($\langle f_T \rangle$) are listed.

fwhm / cm^{-1}	T / K	$\langle E_{T,H} \rangle$ / eV	$\langle E_T \rangle$ / eV	$\langle f_T \rangle$
	OH $A\ ^2\Sigma^+ + O_2 \rightarrow$ **H** + O_3	E_{avail} = 0.685 eV		
2.59(9)	$1.9(1) \times 10^3$	0.25(20	0.25(2)	0.35(3)
	OH $A\ ^2\Sigma^+ + CO \rightarrow$ **H** + CO_2	E_{avail} = 5.08 eV		
2.75(8)	$2.2(1) \times 10^3$	0.28(2)	0.29(2)	0.057(3)

events are observed over a relatively long timescale (50 ns) compared to the rotational period of OH $A\ ^2\Sigma^+$ (v'=0, N'=0), which is on the order of picoseconds. The product translational energy distribution, $P(E_T)$, can be derived from a Maxwell-Boltzmann distribution based on the temperature determined above:

$$P(E_T)dE_T = \frac{2}{\pi^{1/2}(kT)^{3/2}} E_T^{1/2} e^{-E_T/(kT)} dE_T .$$

The translational energy distributions derived using the above procedure and normalized to a peak of unity are shown in Figure 3.[40] For the OH $A\ ^2\Sigma^+$ + O_2 system, the P(E_T) distribution peaks at ~0.08 eV with a tail that extends to the energetic limit (0.68 eV). The P(E_T) distribution for the OH $A\ ^2\Sigma^+$ + CO system peaks at similarly low translational energy (~0.1 eV) with a tail extending to ~1 eV, falling significantly short of the 5.01 eV of available energy.

The average translational energy of the H-atom, $\langle E_{T,H} \rangle = 3kT/2$, is listed in Table 1. This can be converted from the lab frame to the center-of-mass frame to yield the average translational energy release to the products, $\langle E_T \rangle = \langle E_{T,H} \rangle m_{HOO_2} / m_{O_3}$, for the OH $A\ ^2\Sigma^+$ + O_2 system giving $\langle E_T \rangle = 0.25$ eV. An analogous equation for the H + CO_2 products from OH $A\ ^2\Sigma^+$ + CO yields $\langle E_T \rangle = 0.29$ eV. While the average translational energy is similar between the two systems, the fraction of the available energy that goes into translation of the products, $\langle f_T \rangle$, is quite different. The OH + O_2 system has only 0.685 eV of available energy with 35% released as translation on average. By contrast, the OH + CO system has only 5.7% of the 5.08 eV of available energy going into

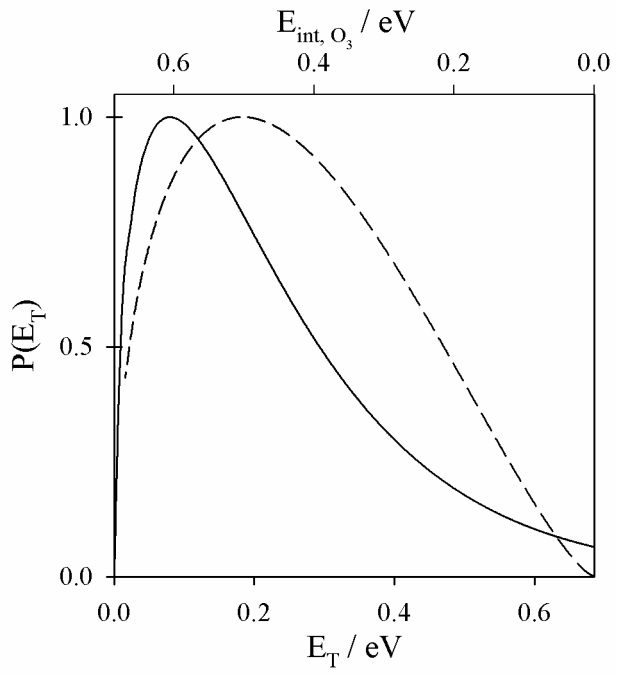

Figure 3. Product translational energy distribution (solid line) arising from reactive quenching of OH $A\ ^2\Sigma^+$ with O_2, producing H + O_3. The statistical distribution (dashed line) is computed using the density of vibrational states for the O_3 product. The graph extends to the available energy for the system. The upper axis shows the balance of available energy after product translation as the internal excitation of the molecular product, O_3.

translation of the products, leaving nearly 4.8 eV on average as internal excitation of CO_2. Note that this is less than the dissociation energy of CO_2 (5.45 eV).[41] The parameters derived from the H-atom Doppler profiles are summarized in Table 1.

The product translational energy distributions for the OH $A\,^2\Sigma^+$ + O_2 and CO systems are also computed for a statistical model for comparison.[42] The model assumes complete randomization of vibrational energy in the OH-O_2 (or OH-CO) reactant pair and that the probability of forming product pairs with a particular translational energy $P(E_T)$ is proportional to the total density of states. The density of vibrational states, $N(E_v)$, is evaluated from a direct count of the O_3 or CO_2 product vibrational states including anharmonicity.[43,44] The total density of product states is then obtained by multiplying by the three-dimensional translational density of states for the recoiling products $E_T^{1/2}$, where $E_T + E_v = E_{avail}$, giving $P(E_T) = N(E_v)E_T^{1/2}$. The statistical $P(E_T)$ distributions, normalized to a peak of unity, are shown in Figures 3 and 4.

For quenching of OH $A\,^2\Sigma^+$ by O_2, the H-atom translational energy distribution is similar to the computed statistical distribution. The average translational energy in both experiment and statistical calculation is 0.25 eV. However, the statistical distribution is peaked to slightly higher translational energy, at ~0.19 eV, meaning the shapes of the distributions are different. The statistical distribution for the OH + CO system is broader and peaked to higher energy than the experimentally observed product translational energy distribution. The statistical $P(E_T)$ peaks at ~1 eV with an average $\langle E_T \rangle = 1.65$ eV

.

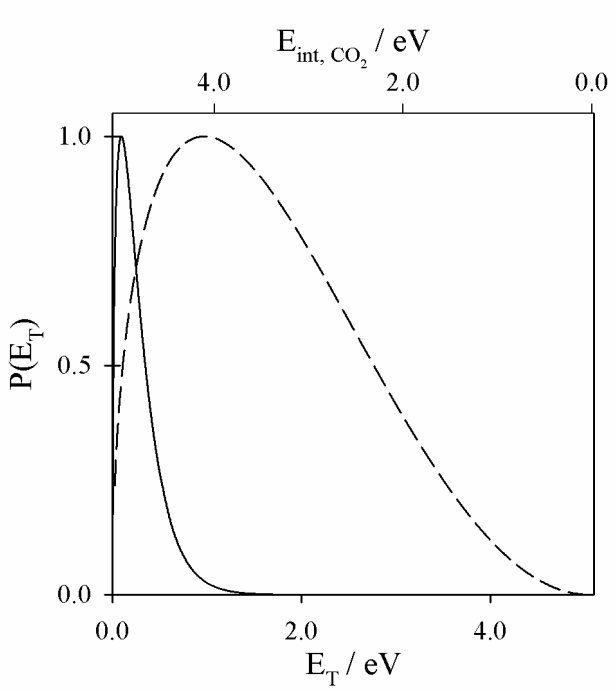

F**igure 4.** Product translational energy distribution (solid line) arising from reactive quenching of OH $A\ ^2\Sigma^+$ with CO, producing H + CO_2. The statistical distribution (dashed line) is computed using the density of vibrational states for the CO_2 product. The graph extends to the available energy for the system. The upper axis shows the balance of available energy after product translation as the internal excitation of the molecular product, CO_2.

The formation of H-atom products in the OH $A\ ^2\Sigma^+$ + CO quenching process likely arises from a highly non-statistical event.

C. O-atom Products of Reactive Quenching

Oxygen atoms are also detected following reactive quenching of OH $A\ ^2\Sigma^+$ by O_2 and CO, indicating that the O + HO_2 and O+ HCO product channels are open. The nascent O 2p ^3P_J fine structure distributions following reactive quenching of OH $A\ ^2\Sigma^+$ with O_2 and CO are also obtained by scanning the probe laser over 3p ^3P_J - 2p ^3P_J transitions. The resulting signals are shown in Figure 5, averaged over several scans to improve the signal to noise ratio and plotted as a function of two-photon energy. For both systems studied, the largest signal is seen for transitions originating from the ground O 2p $^3P_2$ state. The O 2p $^3P_1$ and O 2p $^3P_0$ states, which lie higher in energy than the O 2p $^3P_2$ state by ~158 and ~227 cm^{-1}, respectively, had successively lower intensity in 3p-2p transitions.

While the lower 2p $^3P_0$, $^3P_1$ and $^3P_2$ fine-structure states are well resolved in the 3p-2p transitions shown in Figure 4, the upper 3p ^3P_J states are separated by less than 1 cm^{-1} and cannot be resolved at the effective two-photon probe laser linewidth. The upper state fine structure components results in some inhomogeneous broadening and/or asymmetry of the lines ascribed to the O 3p $^3P_J \leftarrow\leftarrow$ 2p $^3P_0$, $^3P_1$ and $^3P_2$ transitions. The allowed fine structure transitions that give rise to this broadening are marked as sticks in Figure 5. The relative intensities of the stick spectra are predicted using the two-photon absorption cross sections of individual 3p $^3P_{J'} \leftarrow\leftarrow$ 2p $^3P_{J''}$ transitions.[45,46] This inhomogeneous broadening is greater than the O-atom Doppler shifts anticipated,

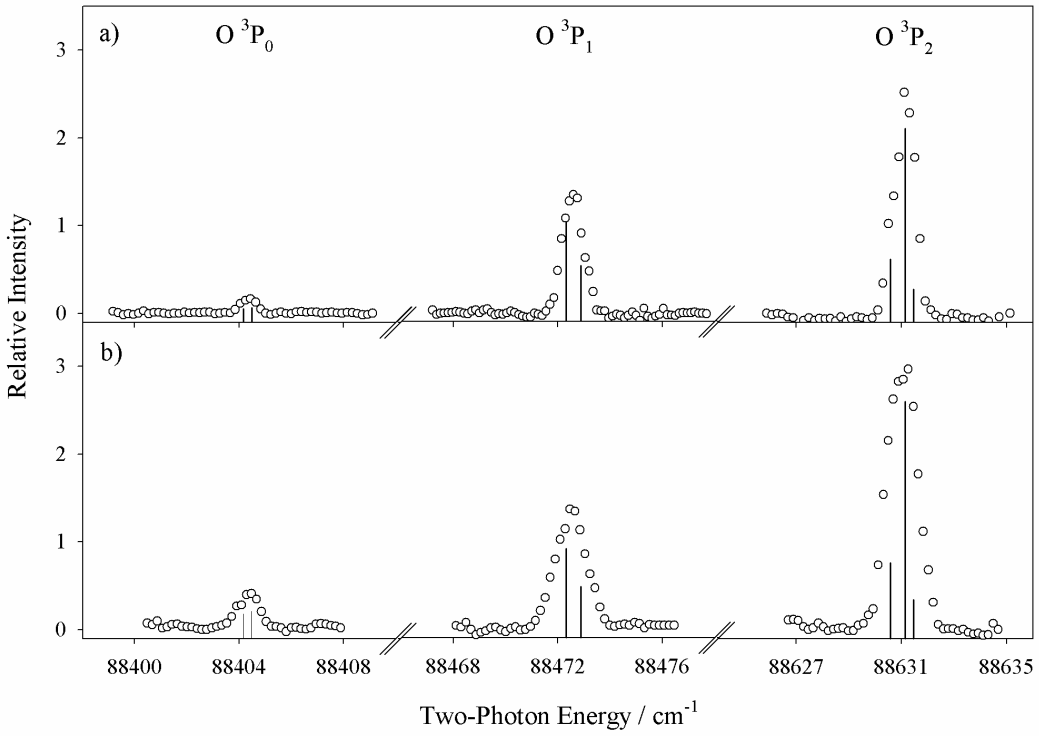

Figure 5. O 2p $^3P_{J=0,1,2}$ fine-structure population distribution arising from reactive quenching of OH $A\ ^2\Sigma^+$ with (a) O_2 and (b) CO. The sticks indicate the expected positions of the upper state components with the relative intensities from Refs. 45,46.

predicted to be less than ± 1 cm^{-1} based on E_{avail}, thereby implying that Doppler profiles and the associated translational energy distributions cannot be extracted from the O-atom 3p – 2p spectral lines.

The total two-photon absorption cross sections are equal for the three O 2p ^{3}P$_J$ fine structure states.[46] As a result, the integrated intensities of the $\sum_{J'=0}^{J'=2} 3p\,^3P_{J'} \leftarrow\leftarrow 2p\,^3P_J$ transitions can be combined directly to give the relative population of the O 2p ^{3}P$_J$ fine structure states. The resulting population distribution of the O 2p ^{3}P$_J$ fine structure states following reactive quenching of OH $A\,^2\Sigma^+$ by O_2 and CO is summarized in Table 2, with uncertainty estimates derived from repeated measurements. The fine structure distributions are similar to a statistical distribution based on degeneracy, with O 2p $^3P_2$:$^3P_1$:$^3P_0$ = 5:3:1.

D. Branching to Reactive Quenching

A primary goal of this work is to determine the branching between various reactive and nonreactive quenching channels. The total branching to quenching products, Γ_Q, can be separated into nonreactive products, Γ_{NRQ}, and reactive products, Γ_{RQ}, such that $\Gamma_Q = \Gamma_{NRQ} + \Gamma_{RQ}$ sums to unity. The branching to nonreactive quenching was previously measured for OH $A\,^2\Sigma^+$ + H_2 and O_2.[3,47] OH $X\,^2\Pi$ (v''=0,1) products are not observed with CO as the quenching partner in this work, suggesting a negligibly small branching to nonreactive products. The branching to reactive quenching is the sum over all reactive quenching product channels. For OH $A\,^2\Sigma^+$ + H_2, reactive quenching produces exclusively H-atoms. However, for OH $A\,^2\Sigma^+$ + O_2 and CO, there are both H-

Table 2. Experimentally determined O 2p $^3P_{J=0,1,2}$ fine-structure population distribution after quenching of OH $A\ ^2\Sigma^+$ by O_2 or CO as well as the statistical fine-structure distribution based on degeneracy.

O $^3P_2$	O $^3P_1$	O $^3P_0$
OH $A\ ^2\Sigma^+ + O_2 \rightarrow$ **O** + HO_2 ($X\ ^2A''$, $A\ ^2A'$) E_{avail} = 1.69, 0.82 eV		
56(8)%	37(6)%	7(2)%
OH $A\ ^2\Sigma^+ + CO \rightarrow$ **O** + HCO E_{avail} = 0.23 eV		
60(6)%	28(5)%	12(4)%
Statistical Distribution		
56%	33%	11%

and O-atom product channels, with O-atom population further partitioned over its fine structure states. The branching to quenching products can then be written as $\Gamma_Q = \Gamma_{NRQ} + \Gamma_{RQ,H} + \sum_{J=0}^{J=2} \Gamma_{RQ,O\,^3P_J}$. The branching to H- and O-atom pathways are directly related to the relative population, P_i, in those product channels.

Assuming that the initially prepared OH $A\,^2\Sigma^+$ (v'=0, N'=0) population and its quenching rate can be set equal for the three quenching partners (H_2, O_2, CO), then the integrated intensities of the H- or O-atom product signals will give the relative yield for reactive quenching to that product channel. As discussed earlier, our experimental conditions (gas composition, backing pressure) are adjusted slightly to result in the same OH $A\,^2\Sigma^+$ fluorescence lifetime of ~150 ns, corresponding to an effective quenching rate of $(190\text{ ns})^{-1}$ and fluorescence quantum yield Φ_f of 0.21 for these three quenchers. The initially prepared OH $A\,^2\Sigma^+$ (v'=0, N'=0) population arises from the OH $X\,^2\Pi$ quantum state distribution from photolysis of HNO_3, cooling in the early phase of expansion, and pump laser saturation of the OH *A*-*X* (0,0) $P_1(1)$ transition. The slightly different experimental conditions (gas composition, backing pressure) likely affects the cooling and gives rise to initial OH $A\,^2\Sigma^+$ (v'=0, N'=0) populations, P_{OH}, as measured from integrated fluorescence signals, that differ for the three quenching partners by a factor on the order of two. This factor is taken into account before comparing H- or O-atom product signals from reactive quenching.

The branching to the H-atom reactive quenching channel can be expressed as

$$\Gamma_{RQ,H} \propto \frac{P_{RQ,H}}{P_{OH}(1-\Phi_f)}$$

where $P_{RQ,H}$ is the integrated intensity of the H-atom Doppler profile and other terms are defined above. A similar expression can be generated for the branching to the O-atom reactive product channels.

The relative amount of H-atoms produced upon quenching of OH $A\ ^2\Sigma^+$ by H_2 is then compared with those from reactive quenching of OH $A\ ^2\Sigma^+$ by O_2 and CO, after accounting for small changes in the initial OH $A\ ^2\Sigma^+$ excited. The H-atoms produced from H_2 quenching ($\Gamma_{RQ} \sim 0.88$) is ~7.5 times greater than that from OH $A\ ^2\Sigma^+ + O_2$. Similarly, the relative amount of H-atoms from quenching by H_2 is ~3.4 times greater than that from quenching by CO. The O-atoms generated in the reactive quenching of OH $A\ ^2\Sigma^+$ by O_2 and CO are also compared, again taking into account the initial OH $A\ ^2\Sigma^+$ excited. Approximately 1.5 times as many O-atoms are generated in quenching of OH $A\ ^2\Sigma^+$ by CO than by O_2. These H- and O-atom product ratios, combined with previously determined branching fractions to nonreactive quenching, are used to determine reactive quenching branching fractions for specific product channels. This will be discussed in Section VIA.

IV. Theoretical Methods

The OH ($X\ ^2\Pi$, $A\ ^2\Sigma^+$) + CO system is also investigated using ab initio calculations to identify conical intersections of states of $^2A'$ symmetry. The theoretical studies take advantage of significant advances in algorithms that can locate CIs between

Table 3. Summary of experimentally determined product branching ratios following the quenching of OH $A\ ^2\Sigma^+$ by H_2, O_2, and CO.

		Product Channel	Branching
OH $A\ ^2\Sigma^+ + H_2$	→	OH $X\ ^2\Pi + H_2$	12(5)%[a]
	→	$H + H_2O$	88(5)%[a]
OH $A\ ^2\Sigma^+ + O_2$	→	OH $X\ ^2\Pi + O_2$	40(1)%[b]
	→	$H + O_3$	12(3)%
	→	$O + HO_2$	48(3)%
OH $A\ ^2\Sigma^+ + CO$	→	OH $X\ ^2\Pi + CO$	--[c]
	→	$H + CO_2$	26(5)%
	→	O + HCO	76(5)%

[a] From Ref. 47
[b] From Ref. 3
[c] Despite an extensive search, products were not found in the OH $X\ ^2\Pi$ (v''=0,1, N'') states probed, as discussed in the main text.

electronic states of the same symmetry,[48,49] which were not available when Vegiri and Farantos carried out their work on this system.[20,21] Multireference configuration interaction (MRCI) wave functions based on molecular orbitals determined from a complete active space (CAS) state averaged multiconfiguration self consistent field (SA-MCSCF) procedure are used throughout this work. The calculations were done in C_s symmetry with cc-pvtz basis set for all atoms (cc-pvtz(10s,5p,2d,1f)→[4s,3p,2d,1f] for C- and O-atoms and cc-pvtz(5s,2p,1d)→[3s,2p,1d] for H-atoms). The molecular orbitals were partitioned into three core orbitals: the 1s orbitals on carbon and oxygen, which were held doubly occupied in all calculations; two a' doubly occupied orbitals, which were held doubly occupied in the SA-MCSCF procedure; and an active space that consisted of 13 electrons in six a′ and three a″ orbitals. The remaining orbitals form the virtual space. In the SA-MCSCF procedure, two states of ^{2}A' and one state of ^{2}A" symmetry were averaged with equal weights, which is appropriate for the regions of the nuclear coordinate space considered here. Dynamic correlation was included at the MRCI level by including single and double excitations from the doubly occupied and active spaces to all virtual orbitals and resulted in MRCI expansions of ~145 x10^6 configuration state functions with ^{2}A' and ^{2}A" symmetry. All electronic structure calculations were carried out using the COLUMBUS suite of programs.[50,51] The use of C_s symmetry provides conceptual as well as computational simplifications, since it separates the effects of one of the two ^{3}A" components of O(^{3}P), which is expected become accessible only in the product channel. This point will be the subject of future investigations. This level of treatment is similar to previous studies of OH quenching.[4,25]

Preliminary calculations using larger and smaller bases for both OH + CO and the well-studied OH + H_2 system served to validate the cc-pvtz treatment for the mechanistic studies reported herein. For example, using the present treatment, the key reactant channel attribute, T_e (OH $A\ ^2\Sigma^+$) is found to be 4.10 eV (4.05 eV), in good accord with the experimental value[52] given parenthetically.

V. Theoretical Results

A. Locus of Points of Conical Intersection

Four regions of strong nonadiabatic coupling were identified in previous work by Vegiri and Farantos.[20,21] In the present study, conical intersection searches were conducted within these regions to identify the energy minimized crossings. The four energy minimized CIs shown in Figure 6 are the focus of this work. A fifth CI was also found that has a linear configuration with the H- side of OH pointing toward CO. However, this CI lies above the OH $A\ ^2\Sigma^+$ + CO asymptote, as indicated previously,[20,21] which is outside the energetic range of the experiment.

The energy minimized CI found in region C1 is linear with an OH to CO center-of-mass separation of 2.46 Å, which is shorter than found previously.[20,21] The OH (1.04 Å) and CO (1.12 Å) bonds are close to their equilibrium bond lengths in their ground electronic states (0.97 Å and 1.13 Å for OH and CO, respectively). This CI is located 1.39 eV (11200 cm^{-1}) below the OH $A\ ^2\Sigma^+$ + CO asymptote. Region M1 has the lowest energy crossing, hence a true minimum energy crossing (MEX) at 2.23 eV (18000 cm^{-1}) below the OH $A\ ^2\Sigma^+$ + CO asymptote, as suggested in the prior work.[20,21] The M1 MEX

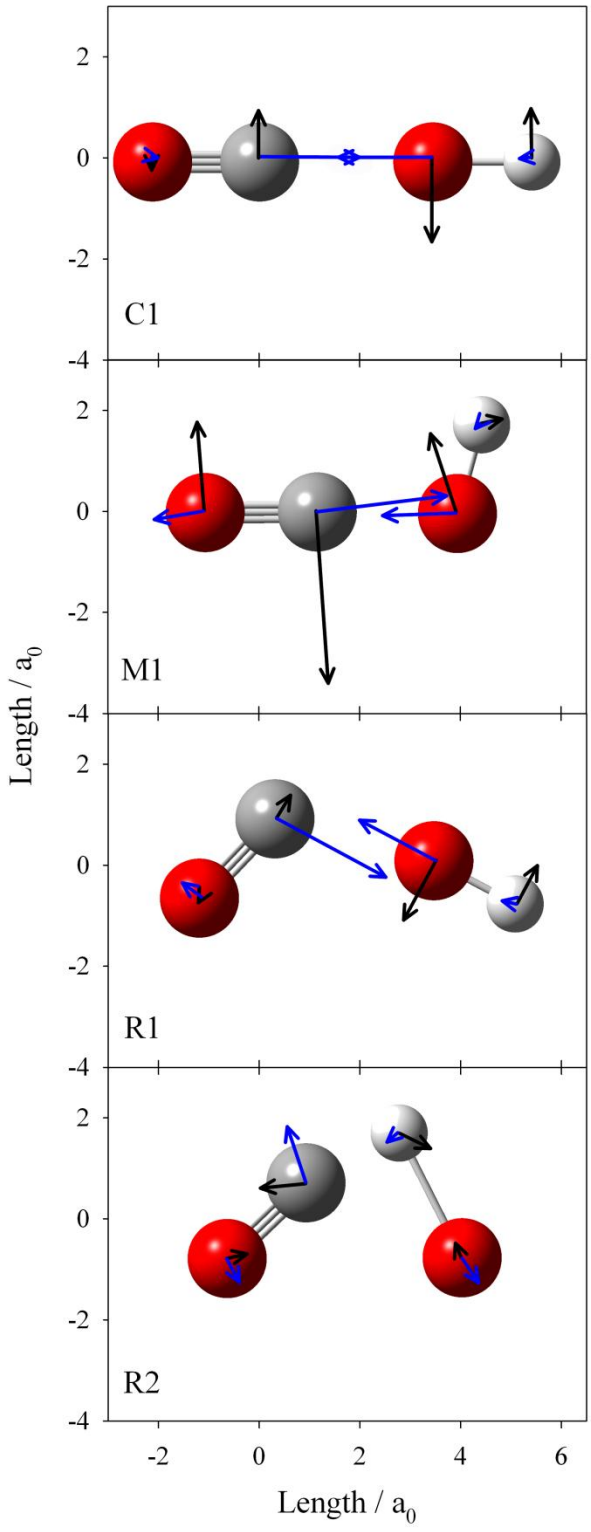
C1
M1
R1
R2
Length / a0
Length / a0

Figure 6. Cartesian representations of the **g** (energy difference, blue arrow) and **h** (interstate coupling, black arrow) vectors for the four main conical intersections identified for the OH + CO system. In all cases, the lengths of the **g** and **h** vectors are scaled by a factor of 20.

has the H-atom rotated off the O-CO axis by 75.4° and a closer OH to CO center-of-mass separation of 2.15 Å. The OH (0.96 Å) and CO (1.18 Å) bond lengths are again close to their equilibrium values. The R1 energy minimized crossing has the oxygen of OH closest to CO with a OH to CO center-of-mass separation of 2.12 Å and similar OH (0.97 Å) and CO (1.15 Å) bond lengths. This CI lies 2.13 eV (17200 cm^{-1}) below the OH $A\ ^2\Sigma^+$ + CO asymptote.

The CI in region R2 is the only energy minimized crossing studied that has the H of OH pointing toward CO. Located 1.16 eV (9400 cm^{-1}) below the OH $A\ ^2\Sigma^+$ + CO asymptote, this CI lies almost 1000 cm^{-1} higher in energy than the other energetically accessible CIs identified. The R2 crossing has a very extended OH bond length of 1.47 Å, while the CO bond length (1.15 Å) remains close to its equilibrium value. The OH to CO center-of-mass separation is 2.14 Å, similar to the CIs in the other three regions, while the H-C distance, 1.11 Å, is close to the H-CO bond length of the formyl radical (1.08 Å).[41] A summary of the properties of the energy minimized CIs in regions C1, M1, R1, and R2 can be found in Table 4.

A seam of CI was also mapped out by stepping the O-H bond length from the elongated bond length (1.47 Å) at the R2 energy minimized crossing to the OH $A\ ^2\Sigma^+$ equilibrium bond length (1.01 Å), while minimizing the energy with respect to the remaining coordinates. The geometric parameters and energies for several CI points along the seam are given in Table 5. The H-C distance along the seam varies from 1.08 to 0.95 Å, remaining close to the H-CO bond length in HCO (1.08 Å). As shown in Figure 7, as the OH bond length is shortened from its value at the R2 crossing, the O side

Table 4. Geometric parameters, conical intersection parameters (a.u.), and energies (eV) relative to the OH $A\ ^2\Sigma^+$ + CO asymptote for the four energy minimized crossings. Geometric parameters include the OH to CO center-of-mass separation (R) and OH and CO bond lengths (r). The angles represent the orientations of CO (θ_1) or OH (θ_2) relative to the line connecting the OH to CO center-of-mass, with 0° defined as the linear OC-OH orientation. The magnitude of the **g** (energy difference) and **h** (interstate coupling) vectors are given by conical intersection parameters G_x and H_y. The tilt of the cone of intersection along these directions is described by S_x and S_y.

	C1	M1	R1	R2
Energy / eV	-1.3859	-2.2289	-2.1329	-1.1584
r(OH) / Å	1.04	0.96	0.97	1.47
r(CO) / Å	1.12	1.18	1.15	1.15
R / Å	2.46	2.15	2.12	2.14
θ_1 / °	0	0.1	45.4	52.6
θ_2 / °	0	75.4	41.9	125.6
G_x	0.1371	0.1579	0.1521	0.0711
H_y	0.1076	0.2101	0.0835	0.0628
S_x	-0.0759	0.0195	0.0140	0.0453
S_y	0.0000	-0.0014	-0.0097	-0.0162

Table 5. Geometric parameters for the OH-CO system at points along the seam of intersection identified leading to the R2 energy minimized crossing. The unconstrained R2 conical intersection and the OH $A\,^2\Sigma^+$ + CO asymptotic values are also given (italics). Parameters include the OH to CO center-of-mass separation (R), OH and CO bond lengths (r), and the internuclear distance between H and C. The angles represent the orientations of CO (θ_1) or OH (θ_2) relative to the line connecting the OH to CO center-of-mass, with 0° defined as the linear OC-OH orientation. Energies relative to the OH $A\,^2\Sigma^+$ + CO asymptote are also given.

r(OH) / Å	r(CO) / Å	R / Å	r(HC) / Å	θ_1 / °	θ_2 / °	θ(CHO) / °	Energy / eV
1.47	*1.15*	*2.14*	*1.11*	*52.6*	*125.6*	*88.8*	*-1.1584*
1.43	1.15	2.14	1.08	51.9	126.9	91.6	-1.1395
1.32	1.17	2.32	1.01	44.6	135.5	108.4	-0.82003
1.22	1.18	2.41	0.95	38.6	143.8	125.4	-0.20663
1.11	1.17	2.52	0.95	28.3	155.6	146.6	-0.05187
1.01	*1.13*	--	--	*0*	*0*	--	*0*

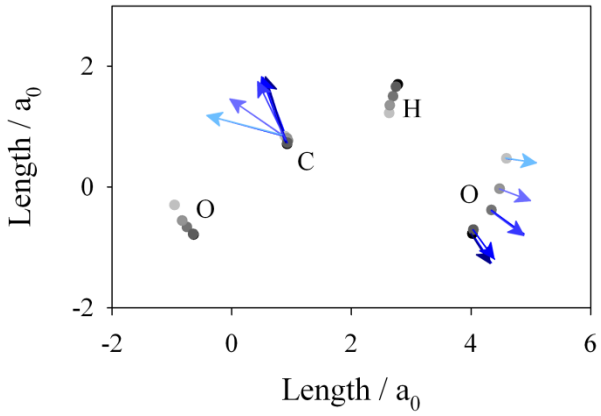

Figure 7. Cartesian representation of the **g** (energy difference, blue arrows) vectors on the C and O atoms and the atomic positions along the seam of intersection from the R2 energy minimized crossing (black circles, darkest blue arrows) to a slightly bent configuration at the OH $A\,^2\Sigma^+$ + CO asymptote (lightest grey circles, lightest blue arrows). In all cases, the lengths of the **g** vectors are scaled by a factor of 20.

of OH swings away from CO and the CHO angle increases from ~90° to 150°, leading to a slightly bent configuration for the CI at the OH $A\ ^2\Sigma^+$ + CO asymptote. This portion of the seam of intersection is energetically accessible from the OH $A\ ^2\Sigma^+$ + CO asymptote. Furthermore, the O + HCO product channel, which lies 0.23 eV below the OH $A\ ^2\Sigma^+$ + CO asymptote, is also energetically accessible along the seam. (As mentioned earlier, a CI in the linear OH-CO configuration lies above this asymptote.)

B. Local Topography of Conical Intersection

This theoretical work also provides new detail on the **g**-**h** branching plane, often used to characterize properties of a CI. The **g** (energy difference) and **h** (interstate coupling) vectors define a plane in which the degeneracy of the electronic states at the CI is lifted linearly. The **g** and **h** vectors for the energy minimized CIs in each region are shown in Figure 6. These vectors illustrate the forces on the nuclei as the system passes through the CI region. Four CI parameters, S_x, S_y, G_x and H_y, listed in Table 4, are used to describe the energetics in this branching plane. Taking the **x** and **y** axes along the orthogonal[53] **g**/||**g**|| and **h**/||**h**|| directions and defining polar coordinates by $x = r\cos\theta$ and $y = r\sin\theta$, the energies of the upper and lower states in the region of the CI can be evaluated directly from these parameters:

$$E_{1,2} = S_x x + S_y y \pm \sqrt{G_x^2 x^2 + H_y^2 y^2} = \rho\left(S_x \cos\theta + S_y \sin\theta \pm \sqrt{G_x^2 \left(\cos\theta\right)^2 + H_y^2 \left(\sin\theta\right)^2}\right)$$

where G_x and H_y define the slope of the cone, and S_x and S_y give the tilt of the cone along the **g** and **h** directions, respectively. Together, the **g** and **h** vectors describe the slope (or pitch) and the asymmetry of the CI. The topography of the CI can be mapped out by

varying the angle θ, which defines a loop around the CI cone at a distance ρ as shown in Figure 8.

In terms of the impact on dynamics, the system will have a propensity to move along the more facile routes, which is the direction of steepest pitch. For the CIs in regions C1 and R1, the steepest gradient, corresponding to the largest change in energy as ρ is increased, occurs by moving along the ±**g** directions (0° and 180°). This is similar to the trend seen for R2, which also shows a propensity for the ±**g** directions. The topography for the M1 MEX displays different trends than seen for the other CIs. For the M1 MEX, moving along the ±**h** directions (90 and -90/270°) results in a large energy change, which indicates a steep pitch.

The tilt of the cone indicates a preference for motion from + to – (or – to +) along the **g** or **h** directions. The tilt is most easily seen by the 3D plot of the cone of intersection, shown in Figure 9, but can also be seen by the vertical symmetry (or asymmetry) of the plots in Figure 8. Regions M1 and R1 both have vertical cones. This indicates that there is little or no preference between + and – **g** (or **h**) directions. By contrast, regions C1 and R2 show a strong tilt and preference for movement from + to – (R2) or – to + (C1) **g**, while the cones are vertical in the ±**h** direction. Movement along **g** is primarily associated with changes in the separation between the OH and CO moieties (denoted R in Tables 4 and 5), while the dominant contribution along **h** corresponds to changes in the OCO (C1, M1, R1) or OCH (R2) bending angle.

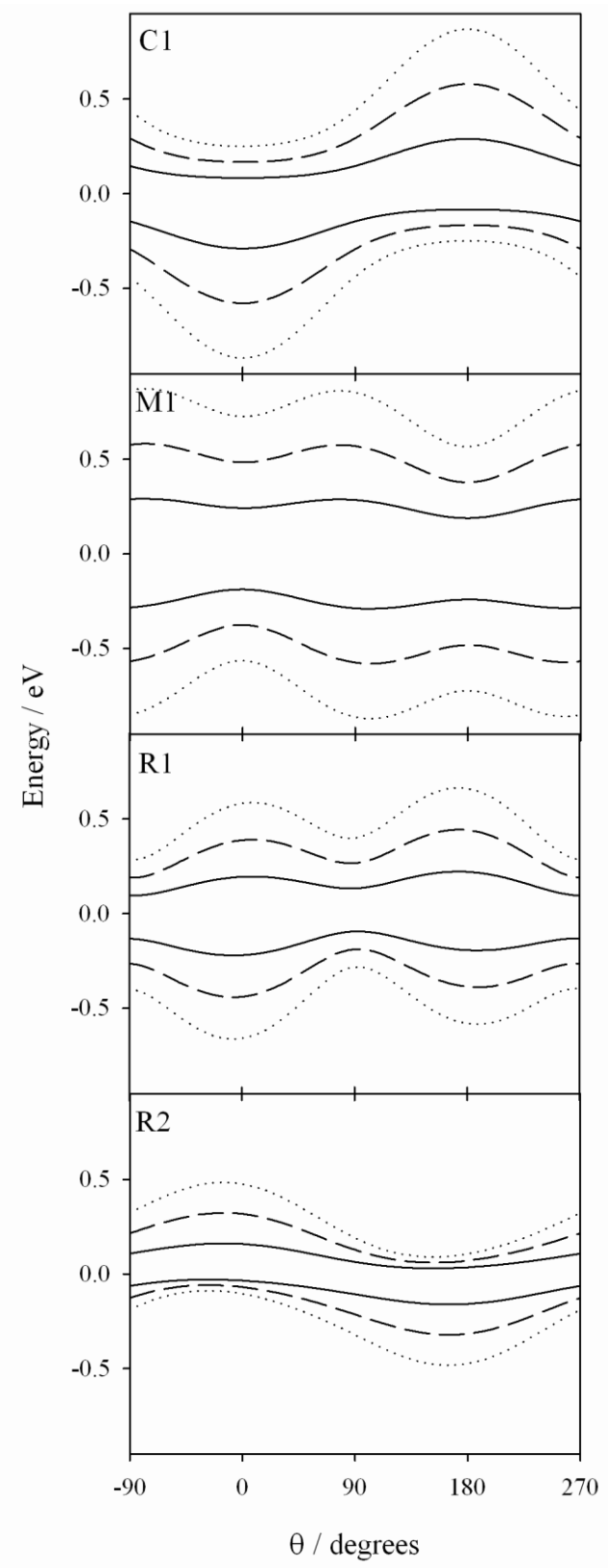
C1
M1
R1
R2
0.5
0.0
-0.5
Energy / eV
-90
0
90
180
270
θ / degrees

Figure 8. Topography of the cone of conical intersection in the vicinity of the four identified conical intersections for the OH + CO system: Regions C1, M1, R1, and R2. Energies of the $1\ ^2A'$ and $2\ ^2A'$ states are shown as a function of θ relative to the energy at the conical intersection (zero). The angle θ defines a loop around the cone at distances of ρ = 0.05 (solid), 0.1 (dashed), and 0.15 (dotted) bohr from the intersection.

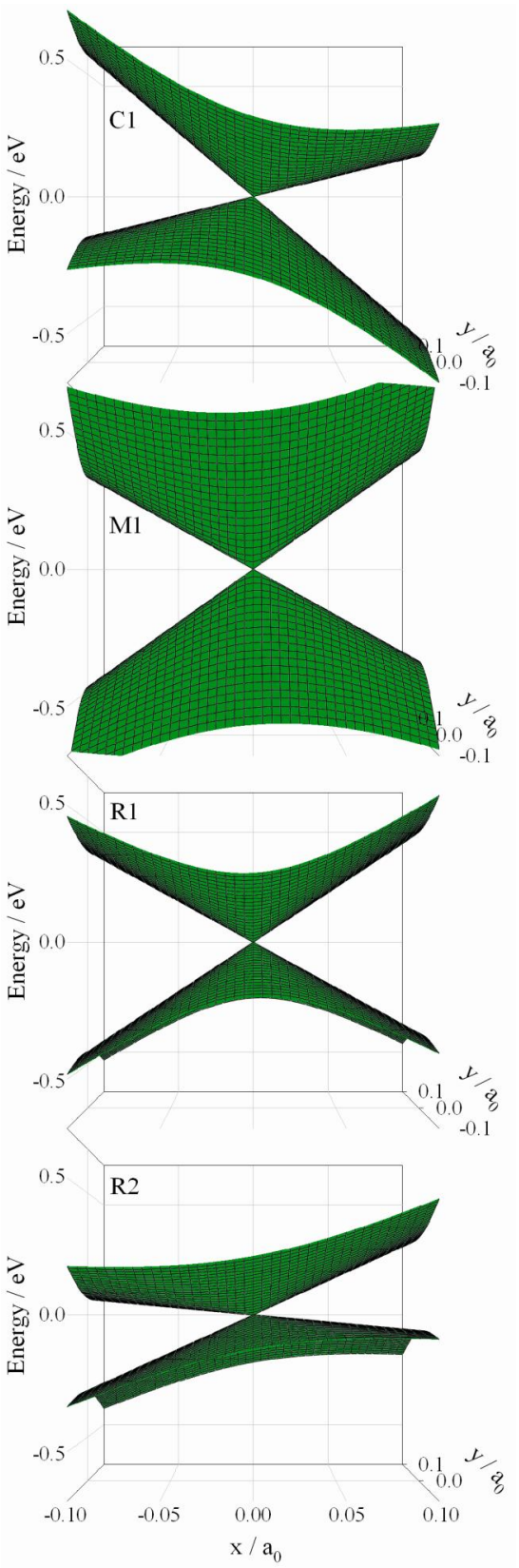
C1
M1
R1
R2
Energy / eV
0.5
0.0
-0.5
y / a0
0.1
0.0
-0.1
-0.10
-0.05
0.00
0.05
0.10
x / a0

Figure 9. Three dimensional plots of the cone of intersections in the OH + CO system for regions C1, M1, R1, and R2, which are characterized by the conical intersection parameters given in Table 4. Energies of the $1\ ^2A'$ and $2\ ^2A'$ states are shown as a function of θ relative to the energy at the intersection (zero). The **g** and **h** vectors lie along the x and y coordinates, respectively. Movement along **g** (x) primarily indicates changes in the OH to CO separation (denoted R in Tables 4 and 5), while the dominant contribution to **h** (y) corresponds to OCO (C1, M1, R1) or OCH (R2) bend.

VI. Discussion

A. Branching to Quenching Product Channels

The branching to reactive quenching channels in the OH $A\ ^2\Sigma^+ + O_2$ system was ascertained using the procedure in Section III D, specifically by making comparisons with the OH $A\ ^2\Sigma^+ + H_2$ system. There are far more H-atoms, 7.5(1.6) times, produced via reactive quenching of OH $A\ ^2\Sigma^+$ by H_2 than O_2. With a previous branching fraction measurement indicating 88(5)% reactive quenching to H-atom products in the OH $A\ ^2\Sigma^+ + H_2$ system,[47] it follows that H-atoms account for only 11(3)% of quenching outcomes in the OH $A\ ^2\Sigma^+ + O_2$ system. Furthermore, adding this H-atom branching fraction of 11(3)% to the previously determined branching fraction for nonreactive quenching of 40(1)%,[3] yields a balance of 48(3)% that occurs via another reactive quenching channel, namely OH $A\ ^2\Sigma^+ + O_2 \rightarrow O + HO_2$ ($X\ ^2A''$, $A\ ^2A'$). Thus, quenching of OH $A\ ^2\Sigma^+$ by O_2 results primarily in production of OH $X\ ^2\Pi + O_2$ (40(1)%) and $O + HO_2$ (48(3)%), with a minor channel producing $H + O_3$ (11(3)%).

A similar procedure and logic is applied to the OH $A\ ^2\Sigma^+ + CO$ system to determine branching fractions. In this case, there are again more H-atoms arising from reactive quenching of OH $A\ ^2\Sigma^+$ by H_2 than CO, specifically 3.4(6) to 1. Again using the branching fraction of 88(5)% for reactive quenching to H-atom products in the OH $A\ ^2\Sigma^+ + H_2$ system, one finds that the H-atom channel accounts for 26(5)% of OH $A\ ^2\Sigma^+ + CO$ quenching. Assuming negligible branching to nonreactive quenching, the remaining 74(5)% would result in O + HCO products. The dominance of O-atom products can be independently corroborated by comparing the O-atom yields from reactive quenching of

OH $A\ ^2\Sigma^+$ by O_2 and CO. There are ~50% more O-atoms produced, specifically 1.6(9) times, upon quenching of OH $A\ ^2\Sigma^+$ by CO than O_2. With a branching fraction for OH $A\ ^2\Sigma^+ + O_2 \rightarrow O + HO_2$ ($X\ ^2A''$, $A\ ^2A'$) of 48(3)%, the larger O-atom yield with CO as the quencher would correspond to 77(8)% of quenching outcomes in the OH $A\ ^2\Sigma^+$ + CO system. Thus, the branching to quenching product channels in the OH $A\ ^2\Sigma^+$ + CO system (with or without the assumption of a negligible branching to nonreactive quenching) is H + CO_2 26(5)% and O + HCO 76(5)%. For CO, the dominant quenching channel is production of O + HCO, with the minor channel, approximately three times smaller, producing H + CO_2. The branching results are summarized in Table 3.

B. Connections to Regions of Conical Intersection

Geometrically, CIs found in regions C1, M1, and R1 are all oriented with the O side of OH pointing toward CO, similar to what was seen previously in the OH + H_2 and N_2 systems.[4,25] This is also the preferred orientation for quenching of OH $A\ ^2\Sigma^+$ by Kr.[54] Given this O-side approach of OH $A\ ^2\Sigma^+$ to CO, these CI regions are most likely to lead to H + CO_2 products (reactive quenching) or possibly separated OH $X\ ^2\Pi$ + CO products (nonreactive quenching), with the latter unobserved experimentally, but not O + HCO product (reactive quenching). Linear interpolation paths have been mapped out connecting the OH $A\ ^2\Sigma^+$ + CO asymptote to the energy minimized crossings in each region. A linear interpolation of coordinates (LIC) path is not a minimum energy path, which would be directed by the gradient of the potential energy surface, but rather simply a direct route from one configuration to another over an arbitrary number of steps. Nevertheless, the LIC paths show a barrierless path leading from OH $A\ ^2\Sigma^+$ + CO to

energy minimized conical intersections in regions C1, M1, and R1, establishing their accessibility. Earlier work also indicated a barrierless path connecting regions R1 to M1, but found a barrier (0.4 eV) separating regions C1 from M1.[20,21]

Additional information can be extracted about the forces in the vicinity of these CIs using the **g** (energy difference) and **h** (interstate coupling) vectors plotted in Figure 6 as well as the topography of the CIs plotted in Figures 8 and 9. The largest gradients for the CIs in regions C1, M1, and R1 suggest the formation of H + CO_2 (reactive) and/or OH $X\,^2\Pi$ + CO (nonreactive) products. The CI in region C1 shows a strong propensity for the energy difference gradient direction (Figure 8), which is related to the movement of H-O and C-O towards or away from each other (**g** vectors in Figure 6). For reactive products originating from region C1, the CO_2 products would likely have some degree of asymmetric stretch excitation due to the extended O-C bond that would be formed (1.84 Å at the CI). The MEX in region M1 shows a propensity for directing the system along the interstate coupling gradient (Figure 8). From Figure 6, this gradient forces both O-atoms in the opposite direction of the C-atom. The CO_2 products formed from passage through this CI would be generated with some degree of bending excitation. The CI in region R1 shows a propensity for direction along the energy difference gradient (Figure 8). The energy difference gradient for the CI in R1 shows the O of OH and the C atom moving towards each other, indicating the possibility of some asymmetric stretch in any CO_2 that might be formed. In addition, from the geometry at the CI, R1 shows a strongly bent CO_2 (OCO angle of 118°) that could result in bending excitation. These three regions (C1, M1, and R1) indicate a propensity for the atoms to move in directions which

could generate vibrationally excited CO_2 products with either asymmetric stretch and/or bend excitation. This is consistent with the experimental observation of minimal kinetic energy release to products and the associated internal excitation of CO_2.

The forces on the nuclei during passage through these three intersections also indicate the possibility of forming nonreactive products. If C1, M1, or R1 leads to nonreactive products, the torque on the OH and CO moieties from the interstate coupling gradient (C1, R1) or energy difference gradient (M1) might result in some rotational excitation of the OH $X\ ^2\Pi$ products from nonreactive quenching. Any OH $X\ ^2\Pi$ products formed would be expected to have very little vibrational excitation since the OH bond length at the CIs are very similar to the OH ground and excited state bond lengths. The absence of experimentally detectable OH $X\ ^2\Pi$ (v''=0,1) products therefore implies that nonreactive quenching is a minor channel (via C1, M1, or R1).

The reactive quenching process that produces O + HCO was found to be the dominant pathway experimentally, accounting for 75% of quenched products. Passage through regions C1, M1, and R1 would not likely generate O + HCO products. However, passage through the seam of conical intersection running from the OH $A\ ^2\Sigma^+$ + CO asymptote to the energy minimized CI in region R2 has the possibility of forming O + HCO products based on the geometric configurations along the seam. The topography of the energy minimized crossing in R2 (Figure 8) shows the largest change along the energy difference gradient (**±g)**. The **±g** vector (Figure 6) primarily pushes the C-atom and O-atom of the elongated O-H in opposite directions. The C-H distance at the CI is already similar to the equilibrium C-H bond length in HCO. As the O-atom of OH is

pushed away from the HCO moiety, the C-atom is also displaced, decreasing the HCO angle from near linear towards the bent HCO equilibrium angle (119.5°). This suggests that HCO products could be formed with bend excitation. The **g**/**h** vectors along the seam of intersection are analogous to those at the energy minimized CI in R2, as shown in Figure 7, with the **g** vectors on the C-atom and O-atom of O-H being the predominant forces.

Region R2 is likely to be the most important region of nonadiabatic coupling leading to quenching based on the properties of the R2 seam and energy minimized CI given above and the dominance of the O + HCO product channel observed experimentally. Prior classical trajectory calculations also point to region R2 as making the most significant contribution to the total quenching cross section. Specifically, the quenching cross section for OH $A\ ^2\Sigma^+$ (v'=0, N'=0) + CO at 300K was calculated to be 41.2 $Å^2$, with 31.1 $Å^2$ from R2 alone, corresponding to 75% of the total cross section for quenching.[21] These calculations compare favorably with the experimental total quenching cross section, which was determined to be 49.6 $Å^2$ for OH $A\ ^2\Sigma^+$ (v'=0, N'=0) + CO at 298K.[55] The large quenching cross section for R2 is also supported by the present calculations, which reveal an extended region of conical intersection along a seam from the OH $A\ ^2\Sigma^+$ + CO asymptote to the energy minimized CI in R2.

Interestingly, the OH + CO system is the first instance of a CI where the H-side of OH $A\ ^2\Sigma^+$ adjacent to its quenching partner provides the dominant pathway for quenching. In the OH + H_2, N_2, and Kr systems,[4,25,54] the conical intersection(s) that leads to quenching occur when the O-side of OH $A\ ^2\Sigma^+$ points toward the collision

partner. While there is an attractive well when the H-side of OH $A\ ^2\Sigma^+$ points towards these collision partners, it does not lead to quenching. For OH-CO, there is also an attractive well on the excited state surface for linear OH-CO, but the seam of conical interaction (R2) leading to reactive quenching only becomes energetically accessible with a bent CHO angle and/or elongated OH bond length.

As a final note, the CI geometry in region R2 has an extended O-H bond length (1.4 Å) compared to the equilibrium bond lengths in the $X\ ^2\Pi$ (0.97 Å) and $A\ ^2\Sigma^+$ (1.01 Å) states. This leaves open the possibility that some of the OH $X\ ^2\Pi$ products could be produced in vibrationally excited levels that are not detected. Based on the experimental branching fractions, however, we estimate that this would be a small contribution (less than 10%).

VII. Conclusions

Collisional quenching of OH $A\ ^2\Sigma^+$ by O_2 proceeds primarily through reactive processes, generating H- and O-atom products that are detected by two-photon laser-induced fluorescence. The translational energy distribution of the H-atom products derived from Doppler spectroscopy reveals a nearly statistical distribution over the available energy in the H + O_3 channel. The fine structure distribution of the O (^3P_J) products in the O + HO_2 channel also appears to be statistical. The relative yield of H-atom products upon quenching of OH $A\ ^2\Sigma^+$ by O_2 and H_2 under similar conditions indicates that the OH $A\ ^2\Sigma^+ + O_2 \rightarrow H + O_3$ channel accounts for only 12(3)% of products. When combined with a prior measurement of the branching fraction [40(1)%]

for OH $X\ ^2\Pi$ ($v'' = 0,1$) products from nonreactive quenching,[3] it is evident that the OH $A\ ^2\Sigma^+ + O_2 \rightarrow O + HO_2$ reaction channel is dominant with 48(3)% of quenched products; the latter is confirmed by comparison of the relative yield of O-atom products upon quenching of OH $A\ ^2\Sigma^+$ by O_2 and CO. Theoretical calculations of the nonadiabatic interactions that give rise to quenching in the OH-O_2 system are challenging because of multiple low-lying electronic surfaces and beyond the scope of this work. Nevertheless, it would be interesting to examine the configuration(s) of the OH and O_2 partners as well as the forces between them in the region(s) of strong nonadiabatic coupling.

Collisional quenching of OH $A\ ^2\Sigma^+$ by CO occurs overwhelmingly via reactive channels, yielding H- and O-atom products that are both detected in the present study. In this system, the Doppler profile of the H-atom products reveals that little of the available energy is released as translational energy and most is accommodated as internal excitation of CO_2. Again, a statistical distribution of the O (^3P_J) fine structure states is found for the O + HCO channel. The relative yield of H- and/or O-atom products upon quenching of OH $A\ ^2\Sigma^+$ by H_2, O_2, and CO under similar conditions shows that the O + HCO reaction channel dominates with 76(5)% of the products; reaction forming H + CO_2 accounts for 26(5)% of products. Nonreactive quenching is at most a minor channel: OH $X\ ^2\Pi$ ($v'' = 0,1$) products from nonreactive quenching are not detected.

Theoretical studies of four regions of strong nonadiabatic coupling accessible from the OH $A\ ^2\Sigma^+$ + CO asymptote have identified the geometric configurations, energy difference gradients, and interstate couplings for conical intersections at energy minimized crossings. For three of the conical intersections (C1, M1, and R1), the O-side

of OH points toward CO and likely leads to H + CO_2 reaction products and/or nonreactive quenching. The forces that linearly lift the degeneracy at the conical intersections suggest that the CO_2 products will be vibrationally excited, consistent with the minimal translational energy observed experimentally. An interesting future direction would be to explore the connectivity of these energy minimized intersections (C1, M1, and R1). A seam of intersection originating at the OH $A\ ^2\Sigma^+$ + CO asymptote and running along a barrierless path to a fourth energy minimized crossing (R2) has a very different nuclear configuration. In this case, the H-side of an elongated OH points toward CO in a bent configuration, and is likely the origin of the dominant O + HCO product channel. The theoretical calculations indicate the pitch and tilt of the cone, suggesting the most facile route(s) for passage to products. Nevertheless, dynamical calculations are still needed to evaluate the branching between multiple reactive and nonreactive product channels as well as other experimental observables which may reflect properties of the conical intersection region(s) that give rise to quenching of OH $A\ ^2\Sigma^+$ by CO. Given that OH ($X\ ^2\Pi$, $A\ ^2\Sigma^+$) + CO is a theoretically tractable system, it would also be desirable to conduct quenching experiments under crossed-molecular beam or velocity map imaging conditions.[9,56]

Acknowledgements

This research was supported by the Office of Basic Science of the Department of Energy. The authors thank Joseph J. Dillon (JHU) and Xiaolei Zhu (JHU) for useful discussions and contributions to the theoretical work. J.H.L and M.I.L. thank Logan P. Dempsey

(Wisconsin) for his assistance on the nonreactive quenching of OH $A\,^2\Sigma^+$ by CO portion of this work.

References

1 P. A. Cleary, L. P. Dempsey, C. Murray, M. I. Lester, J. Kłos, and M. H. Alexander, J. Chem. Phys. **126**, 204316 (2007).

2 L. P. Dempsey, C. Murray, P. A. Cleary, and M. I. Lester, Phys. Chem. Chem. Phys. **10**, 1424 (2008).

3 L. P. Dempsey, T. D. Sechler, C. Murray, and M. I. Lester, J. Phys. Chem. A **113**, 6851 (2009).

4 L. P. Dempsey, T. D. Sechler, C. Murray, M. I. Lester, and S. Matsika, J. Chem. Phys. **130**, 104307 (2009).

5 J. H. Lehman, L. P. Dempsey, M. I. Lester, B. Fu, E. Kamarchik, and J. M. Bowman, J. Chem. Phys. **133**, 164307 (2010).

6 D. T. Anderson, M. W. Todd, and M. I. Lester, J. Chem. Phys. **110**, 11117 (1999).

7 M. W. Todd, D. T. Anderson, and M. I. Lester, J. Phys. Chem. A **105**, 10031 (2001).

8 J. H. Lehman, J. L. Bertrand, T. A. Stephenson, and M. I. Lester, J. Chem. Phys. **135**, 144303 (2011).

9 M. Ortiz-Suárez, M. F. Witinski, and H. F. Davis, J. Chem. Phys. **124**, 201106 (2006).

10 R. D. Kenner, F. P. Capetanakis, and F. Stuhl, J. Phys. Chem. **94**, 2441 (1990).

11 S. S. Xantheas, G. J. Atchity, S. T. Elbert, and K. Ruedenberg, J. Chem. Phys. **94**, 8054 (1991).

12 D. E. Heard and D. A. Henderson, Phys. Chem. Chem. Phys. **2**, 67 (2000).

13 P. E. Charters, R. G. Macdonald, and J. C. Polanyi, Appl. Opt. **10**, 1747 (1971).

14 D. Klenerman and I. W. M. Smith, J. Chem. Soc., Faraday Trans. 2 **83**, 229 (1987).

15 S. D. Le Picard, M. Tizniti, A. Canosa, I. R. Sims, and I. W. M. Smith, Science **328**, 1258 (2010).

16 D. C. McCabe, I. W. M. Smith, B. Rajakumar, and A. R. Ravishankara, Chem. Phys. Lett. **421**, 111 (2006).

17 U. C. Sridharan, F. S. Klein, and F. Kaufman, J. Chem. Phys. **82**, 592 (1985).

18 J. M. Beames, M. I. Lester, C. Murray, M. E. Varner, and J. F. Stanton, J. Chem. Phys. **134** (2010).

19 C. Murray, E. L. Derro, T. D. Sechler, and M. I. Lester, Acc. Chem. Res. **42**, 419 (2009).

20 A. Vegiri and S. C. Farantos, in *Selectivity in Chemical Reactions*, edited by J. C. Whitehead (Kluwer Academic Publishers, 1988), pp. 393.

21 A. Vegiri and S. C. Farantos, Mol. Phys. **69**, 129 (1990).

[22] T. G. Clements and R. E. Continetti, J. Chem. Phys. **115**, 5345 (2001).
[23] E. Garand, K. Klein, J. F. Stanton, J. Zhou, T. I. Yacovitch, and D. M. Neumark, J. Phys. Chem. A **114**, 1374 (2010).
[24] M. E. Greenslade, M. Tsiouris, R. T. Bonn, and M. I. Lester, Chem. Phys. Lett. **354**, 203 (2002).
[25] B. C. Hoffman and D. R. Yarkony, J. Chem. Phys. **113**, 10091 (2000).
[26] D. R. Yarkony, J. Chem. Phys. **111**, 6661 (1999).
[27] B. Fu, E. Kamarchik, and J. M. Bowman, J. Chem. Phys. **133**, 164306 (2010).
[28] E. Kamarchik, B. N. Fu, and J. M. Bowman, J. Chem. Phys. **132**, 091102 (2010).
[29] P. Y. Zhang, R. F. Lu, T. S. Chu, and K. L. Han, J. Chem. Phys. **133**, 174316 (2010).
[30] P. Y. Zhang, R. F. Lu, T. S. Chu, and K. L. Han, J. Phys. Chem. A **114**, 6565 (2010).
[31] M. A. Collins, O. Godsi, S. Liu, and D. H. Zhang, J. Chem. Phys. **135**, 234307 (2011).
[32] D. G. Truhlar, presented at the American Chemical Society, San Diego, 2012 (unpublished).
[33] P. J. Dagdigian, B. E. Forch, and A. W. Miziolek, Chem. Phys. Lett. **148**, 299 (1988).
[34] Q. Li, R. T. Carter, and J. R. Huber, Chem. Phys. Lett. **334**, 39 (2001).
[35] A. A. Turnipseed, G. L. Vaghjiani, J. E. Thompson, and A. R. Ravishankara, J. Chem. Phys. **96**, 5887 (1992).
[36] J. Luque and D. R. Crosley, SRI International Report MP 99-009 (1999).
[37] M. W. Chase, J. L. Curnutt, J. R. Downey, R. A. McDonald, A. N. Syverud, and E. A. Valenzuela, J. Phys. Chem. Ref. Data **11**, 695 (1982).
[38] There was a typo in Ref. 8, where E_{coll} = 0.005 eV. A translational temperature is derived from a Gaussian fit to the Doppler profile of background H-atoms arising from the photolysis of the nitric acid precursor. The background H-atoms are formed at the throat of the expansion and probed in the laser interaction region, which is in the collisional region of the expansion. The temperature gives a distribution of kinetic energies, which in turn we use as an estimate of the average collision energy for all species in the expansion; the collisions average over the relative orientations of the partners. It is important to note that the collision energy in the supersonic expansion is small compared to the energy released in the quenching event.
[39] R. N. Zare and D. R. Herschbach, Proc. IEEE **51**, 173 (1963).
[40] A more extensive analysis procedure was recently used in Ref. 8 and was also repeated here. The resultant $P(E_T)$ distributions are identical to those found by using the Maxwell-Boltzmann distribution. This implies that the H-atom Doppler profiles arising from quenching of OH $A\ ^2\Sigma^+$ by CO and O_2 are indeed very well modeled by single Gaussian fits. The Maxwell-Boltzmann distribution is preferred here due to the continuous nature of the functional form and ease of use in deriving average properties from the distribution.

[41] G. Herzberg, *Electronic spectra and electronic structure of polyatomic molecules*. (Van Nostrand, New York, 1966).
[42] M. N. R. Ashfold, R. N. Dixon, M. Kono, D. H. Mordaunt, and C. L. Reed, Philos. Trans. R. Soc. Lond. Ser. A-Math. Phys. Eng. Sci. **355**, 1659 (1997).
[43] A. Barbe, A. Chichery, T. Cours, V. G. Tyuterev, and J. J. Plateaux, J. Mol. Struct. **616**, 55 (2002).
[44] A. Chedin, J. Mol. Spectrosc. **76**, 430 (1979).
[45] M. S. Pindzola, Phys. Rev. A **17**, 1021 (1978).
[46] D. J. Bamford, M. J. Dyer, and W. K. Bischel, Phys. Rev. A **36**, 3497 (1987).
[47] L. P. Dempsey, C. Murray, and M. I. Lester, J. Chem. Phys. **127**, 151101 (2007).
[48] M. J. Bearpark, M. A. Robb, and H. B. Schlegel, Chem. Phys. Lett. **223**, 269 (1994).
[49] M. R. Manaa and D. R. Yarkony, J. Am. Chem. Soc. **116**, 11444 (1994).
[50] H. Lischka, R. Shepard, R. M. Pitzer, I. Shavitt, M. Dallos, T. Muller, P. G. Szalay, F. B. Brown, R. Ahlrichs, H. J. Böhm, A. Chang, D. C. Comeau, R. Gdanitz, H. Dachsel, C. Ehrhardt, M. Ernzerhof, P. Höchtl, S. Irle, G. S. Kedziora, T. Kovar, V. Parasuk, M. J. M. Pepper, P. Scharf, H. Schiffer, M. Schindler, M. Schüler, M. Seth, E. A. Stahlberg, J.-G. Zhao, S. Yabushita, Z. Y. Zhang, M. Barbatti, S. Matsika, M. Schuurmann, D. R. Yarkony, S. R. Brozell, E. V. Beck, and J.-P. Blaudeau, COLUMBUS, an *ab initio* electronic structure program (2006).
[51] H. Lischka, R. Shepard, R. M. Pitzer, I. Shavitt, M. Dallos, T. Muller, P. G. Szalay, M. Seth, G. S. Kedziora, S. Yabushita, and Z. Y. Zhang, Phys. Chem. Chem. Phys. **3**, 664 (2001).
[52] K. P. Huber and G. Herzberg, in NIST Chemistry WebBook, http://webbook.nist.gov.
[53] D. R. Yarkony, J. Chem. Phys. **112**, 2111 (2000).
[54] J. A. Klos, P. J. Dagdigian, M. H. Alexander, F. J. Aoiz, M. Brouard, J. H. Lehman, and M. I. Lester, personal communication (2012).
[55] R. A. Copeland, M. J. Dyer, and D. R. Crosley, J. Chem. Phys. **82**, 4022 (1985).
[56] J. J. Kay, G. Paterson, M. L. Costen, K. E. Strecker, K. G. McKendrick, and D. W. Chandler, J. Chem. Phys. **134**, 091101 (2011).

CHAPTER 5
Electronic Quenching of OH $A\ ^2\Sigma^+$ Induced by Collisions with Kr Atoms

The experimental research presented in this chapter was primarily performed at the University of Pennsylvania, with additional experiments at the University of Oxford, and the theoretical calculations were performed at University of Maryland, Johns Hopkinds University, and Universidad Complutense, Madrid. This research has been accepted for publication as a paper as part of the Terry A. Miller Festschrift in the *Journal of Physical Chemistry A*.

Reference: J. H. Lehman, M. I. Lester, J. Klos, M. H. Alexander, P.J. Dagdigian, D. Herraez-Aguilar, F.J. Aoiz, M. Brouard, H. Chadwick, T. Perkins, S.A. Seamons, *J. Phys. Chem. A*, accepted (2013).

I. Introduction

The hydroxyl radical is an important species in atmospheric and combustion environments, often detected using laser-induced fluorescence (LIF) on the OH $A\ ^2\Sigma^+ - X\ ^2\Pi$ band system.[1] However, extensive kinetics studies have shown that these radicals are efficiently removed from the excited $A\ ^2\Sigma^+$ state via collisions with molecular or atomic partners, resulting in dramatically reduced fluorescence lifetimes and quantum yields. Kinetic studies have been carried out over a variety of temperatures and initial OH $A\ ^2\Sigma^+$ rotational level, showing that rates decrease with increasing temperature and OH $A\ ^2\Sigma^+$ rotational excitation.[2-5] A recent example of such studies is the quenching cross section measurements for various spin-rotation levels of OH $A\ ^2\Sigma^+$ for Kr by Chadwick *et al.*[6] These trends are indicative of a quenching mechanism controlled by an attractive interaction on the excited state surface that depends on OH orientation.[2-5] Molecular partners, such as H_2 (~8 Å^2) and N_2 (~5 Å^2), have large quenching cross sections at room temperature. On the other hand, rare gas colliders typically have negligibly small quenching cross sections (σ_Q ~ 0.004 Å^2 and 0.047 Å^2 for He and Ar, respectively).[7-9] In contrast, the heavier rare gases, starting with Kr (σ_Q ~ 8 Å^2 at 300 K), have quenching cross sections very similar in magnitude to those of the molecular partners.[10]

In order to gain further insight into the quenching mechanism, recent experimental studies in one of our laboratories (University of Pennsylvania), and others,[11,12] have focused on the outcomes of the quenching event. Characteristics of the

reactive (forming new products) and/or nonreactive (returning OH to its ground $X\,^2\Pi$ state) events have been studied for several quenching partners (H_2, D_2, N_2, CO, CO_2, O_2).[11,13-20] Branching fractions have also been determined.[14-20] The importance of the nonreactive OH $X\,^2\Pi$ (v''=0–2) pathways varies significantly with collision partner, ranging, for example, from 12% for H_2 to 88% for N_2. The focus of the Oxford laboratory has been on the fate of the electronically excited OH that survives the quenching process and remains electronically excited after the collision.

On the other hand, the characteristics of the OH $X\,^2\Pi$ product state distributions following nonreactive quenching of OH $A\,^2\Sigma^+$, in which 4.06 eV of electronic energy is released to products, are quite similar for most collision partners. The OH $X\,^2\Pi$ product is released with a high degree of rotational but little vibrational excitation. In the OH + H_2 system, the rotational distribution is peaked about N'' = 15 with an average rotational energy $\langle E_{rot} \rangle$ = 4480 cm^{-1} in v''=0. OH $X\,^2\Pi$ is produced predominantly in v''=0 (75%) with less products found in v''=1 (20%) and v''=2 (5%). Collisional quenching with N_2 results in an even higher degree of rotation ($\langle E_{rot} \rangle$ = 6540 cm^{-1} in v''=0), with less energy going into OH vibration (97% of products are found in v''=0). Both collision partners also show a preference for populating the $\Pi(A')$ Λ-doublet component, where the unpaired electron of OH $X\,^2\Pi$ lies in a pπ orbital within the plane of nuclear rotation.[21] For collisions of OH $A\,^2\Sigma^+$ with Kr, only nonreactive quenching can occur. Based on the OH $X\,^2\Pi$ product state distribution seen in other systems, we might anticipate similar trends following quenching by Kr.

The pairing of experiment with theory has been essential for understanding the quenching process. For this reason, the OH + H_2 system has emerged as a benchmark for elucidating the quenching mechanism. Theoretical work has identified regions of conical intersection accessible from OH $A\ ^2\Sigma^+$ + H_2 when the oxygen side of OH points toward H_2.[13,22-25] These regions of strong nonadiabatic coupling allow population to be funneled from the excited state surface to OH $X\ ^2\Pi$ + H_2 or H_2O + H products. Interestingly, when the hydrogen side of OH $A\ ^2\Sigma^+$ points toward H_2, there is an attractive electrostatic interaction but no pathway leading to quenching.[13,23,26]

Characteristics of the conical intersection and topography of the potential energy surface have been used to explain, at least qualitatively, the significant rotational and minimal vibrational excitation of the OH $X\ ^2\Pi$ products.[13,22,25] Recently, classical trajectory[19,27-29] and quantum scattering calculations[30,31] for the OH $A\ ^2\Sigma^+$ + H_2 system yielded OH $X\ ^2\Pi$ product distributions and branching fractions similar to those measured experimentally. In the OH + N_2 system, *ab initio* calculations identified an energetically accessible conical intersection coupling the ground and electronically excited state surfaces, again when the oxygen side of OH $A\ ^2\Sigma^+$ points toward the N_2 partner.[17] In the OH–N_2 configuration, there is also an attractive intermolecular interaction but no pathway for quenching.[23] The forces in the region of conical intersection indicate a propensity toward nonreactive products with a large degree of OH rotation and

comparatively less OH vibration with N_2 than predicted for H_2, which is consistent with experimental results.[17]

The majority of previous experimental and theoretical studies for the OH ($X\ ^2\Pi$, $A\ ^2\Sigma^+$) + Kr system have been focused on the OH–Kr van der Waals complex formed when the H-side of OH $X\ ^2\Pi$ interacts with Kr and its subsequent electronic excitation.[32-35] High-resolution electronic spectroscopy studies by Miller and coworkers enabled analysis of several vibronic bands of OH–Kr on the $A\ ^2\Sigma^+ - X\ ^2\Pi$ transition.[32,33] These authors derived rotational constants and bond lengths for the ground state and several vibronic levels in the excited electronic state. In addition, they characterized intermolecular stretch progressions with and without bend excitation in the excited electronic state. The spectroscopic data was then utilized to develop an empirical potential energy surface for OH $A\ ^2\Sigma^+$ + Kr, which was reliable primarily in the $\theta \leq 60°$ region about the linear OH–Kr (Jacobi angle $\theta = 0°$) minimum energy configuration with a well depth of $D_e \sim 2420$ cm^{-1} at R_e=5.24 a_0. A second well in the linear HO–Kr configuration was estimated to have a well depth of 1900 cm^{-1} at a much shorter intermolecular distance of 4.16 a_0.

More recent theoretical work utilized RCCSD(T) calculations to map out the electronically excited OH $A\ ^2\Sigma^+$ + Kr potential energy surface for a fixed OH bond length.[6] This *ab initio* study revealed a significantly deeper potential well in the linear HO–Kr ($\theta = 180°$) configuration than the prior empirical potential with a substantially larger well depth of $D_e \sim 6079$ cm^{-1} at $R_e \sim 4.16$ a_0. The HO–Kr minimum is separated from the linear OH–Kr configuration by a large barrier (greater than 1850 cm^{-1}). The

properties of the OH–Kr well and its energy level structure were in reasonable agreement with the prior work by Miller and coworkers, although some vibrational level reassignments were suggested. The study of Chadwick *et al.*[6] also included new experimental measurements of OH $A\ ^2\Sigma^+$ – Kr rotationally-inelastic scattering cross sections using Zeeman quantum beat spectroscopy. Both quantum mechanical and quasi-classical trajectory scattering calculations were performed on the new OH $A\ ^2\Sigma^+$ + Kr potential energy surface, yielding cross sections, which were in good agreement with experiment.[6]

In this paper, we present the nascent OH $X\ ^2\Pi$ product state distribution, including vibrational, rotational, and fine-structure propensities, and cross sections for the quenching of OH $A\ ^2\Sigma^+$ by Kr. These measurements probe portions of the OH $A\ ^2\Sigma^+$ + Kr excited state potential that allow for nonadiabatic coupling and efficient population transfer from the excited state to the OH $X\ ^2\Pi$ + Kr ground state surface. Complementary theoretical calculations show that the nonadiabatic coupling occurs in the HO–Kr well region, which has heretofore not been experimentally probed. The experimental observables are a measure of the forces on the OH radical as it passes through the strong nonadiabatic coupling region and subsequently separates from Kr on the ground state surface.

II. Experimental Methods

Two types of experiments were performed. The first, performed under jet expansion conditions at the University of Pennsylvania, were used to determine lifetime and OH $X\,^2\Pi$ population data. The second set, performed under thermal conditions at 300 K at the University of Oxford, were used to determine thermally averaged collisional quenching cross-sections.

A. Lifetime and Population Measurements

The experimental methods for investigating the outcomes following collisional quenching of OH $A\,^2\Sigma^+$ by Kr are similar to those used previously for other quenching partners at the University of Pennsylvania.[13,14,16,17,19] Briefly, OH $X\,^2\Pi$ radicals are generated in the throat of a pulsed supersonic jet expansion by photolyzing nitric acid (98% fuming) at 193 nm. The nitric acid vapor is entrained in a 20% Kr/He gas mixture with a backing pressure of 80 psi. In the collision region of the expansion at a distance of x/D = 5 in nozzle diameters D, the OH radicals are excited on the $P_1(1)$ line of the $A\,^2\Sigma^+$ - $X\,^2\Pi$ (0,0) transition with the UV pump laser operating at 308 nm. The pump laser induced fluorescence (LIF) is collected with a photomultiplier tube (PMT, ET Enterprises 9813Q) using a 308 nm bandpass filter. After a 100 ns delay, a spatially overlapped and counter propagating UV laser intersects the expansion and probes the quenched OH $X\,^2\Pi$ products by means of various OH A-X transitions with vibrational (v''), rotational (N''), and fine-structure resolution. Probe LIF signals are collected using the same PMT but with different bandpass filters. The probe laser excitation and fluorescence collection schemes are the same as used in prior experiments with N_2 as a collision partner.[17]

The LIF signals are processed with a digital storage oscilloscope (LeCroy WaveRunner 6050A) and transferred to a laboratory computer for further analysis. The waveform traces are fit to single exponential decays to determine fluorescence lifetimes and integrated over a fixed gate to obtain intensities. The probe LIF intensities, recorded under saturated LIF conditions, are scaled relative to a reference line and converted to relative OH $X\,^2\Pi$ populations using the same analysis procedure that has been described previously.[13,14,16,17,19] The analysis procedure accounts for the lifetime and fluorescence quantum yield (Φ_f) of the emitting state as well as the filter transmission function.

An active background subtraction scheme,[13,14,16,17,19] is used in data collection. Briefly, the pump laser (5 Hz) is operated at half the repetition rate of the probe laser (10 Hz). The background signal arising from the probe laser only is subtracted from the combined pump and probe laser-induced signal. This scheme enables one to distinguish between the desired signal arising from the combination of pump and probe lasers, and background signals originating from the probe laser only.

B. Thermally averaged electronic quenching cross-sections.

Absolute, thermally averaged cross-sections for electronic quenching of OH $A\,^2\Sigma^+$ by Kr at 300 K were measured at the University of Oxford. The methods used are the same as described in previous studies[6] and so are summarized here only briefly.

OH $X\,^2\Pi$ is generated by the photolysis of hydrogen peroxide or nitric acid at 193 nm, and is excited to the $A\,^2\Sigma^+$ state on the (0,0) band with a pulsed dye laser after a delay

of around 10 μs to allow the radicals to thermalize translationally. A photoelastic modulator (PEM) is used to switch the laser polarization direction either parallel or perpendicular to the detection axis on alternate shots. The resulting fluorescence from OH $A\,^2\Sigma^+$ passes through a linear polarizer and is detected by a photomultiplier tube.

The fluorescence traces from parallel ($I_\parallel$) and perpendicular ($I_\perp$) laser polarization directions with respect to the detection axis are fitted using $I_\parallel + 2I_\perp$, which is sensitive only to the decay in population, and independent of the decay in polarization. The data are fitted to a single exponential

$$I = A\,\mathrm{e}^{-(k_\mathrm{f}+k_\mathrm{Q}[\mathrm{Kr}])t}$$

where k_f is the inverse of the fluorescence lifetime and k_Q is the quenching rate constant. By measuring decays over a range of Kr pressures in the range ~100 mTorr to ~600 mTorr, k_Q can be determined and converted into a thermal averaged quenching cross-section *via* $\sigma_Q = k_\mathrm{Q}(T)/\langle v_\mathrm{rel}\rangle$. Errors are taken as one standard deviation for comparison with the literature.[5]

In these unresolved measurements, rotational energy transfer (RET) does not directly contribute to the decay rate of the OH(*A*) emission. However, significant rotational energy transfer between rotational levels of OH(*A*) would scramble the initial state selectivity of the electronic quenching measurements. For this reason, only the first ~100 ns of the fluorescence decay was fitted to ensure that the measured electronic quenching rate constants were specific to a single *N* level. Detailed simulations and fits were performed, as described in Ref. 36, to verify that this procedure yielded the correct

initial state selected electronic quenching rate constants within the quoted errors in the measurements.

III. Experimental Results

A. OH $A\ ^2\Sigma^+$ Lifetimes

The OH radicals prepared in the lowest rovibrational level (v=0, N=0) of the excited $A\ ^2\Sigma^+$ electronic state have a fluorescence lifetime of 400(15) ns in the collisional region of the supersonic expansion, which is significantly shorter than the radiative lifetime of ~700 ns. Collisions with Kr in the 20% Kr/He carrier gas mixture are relatively efficient in quenching the OH $A\ ^2\Sigma^+$ (v=0, N=0); pure He carrier gas does not quench the fluorescence. Using a 20% N_2/He carrier gas mixture at 80 psi under similar experimental conditions, the fluorescence lifetime is approximately 320 ns. The fluorescence lifetimes are measured for each of the OH $A\ ^2\Sigma^+$ (v= 0, 1, N) levels accessed by the probe laser, shown in Fig. 1 with values at each N averaged over spin-orbit components. This data is used in the analysis of OH $X\ ^2\Pi$ populations. The experimentally measured total rates (k_{tot}) are the sum of the collisional (k_{coll}), radiative (k_{rad}), and electronic predissociation (k_{PD}) rates at each N. The radiative and electronic predissociation rates for OH $A\ ^2\Sigma^+$ are tabulated in LIFBASE.[37] The pseudo-first-order collisional rates, k_{coll}, are readily extracted and are plotted in Fig. 1.

In OH $A\ ^2\Sigma^+$ (v=0), the collisional rate is due solely to collisional quenching. The rate is largest for N=0 and smaller for the high N levels examined in this work, remaining fairly constant from N=18-22, but then increasing slightly at high N; the latter effect is

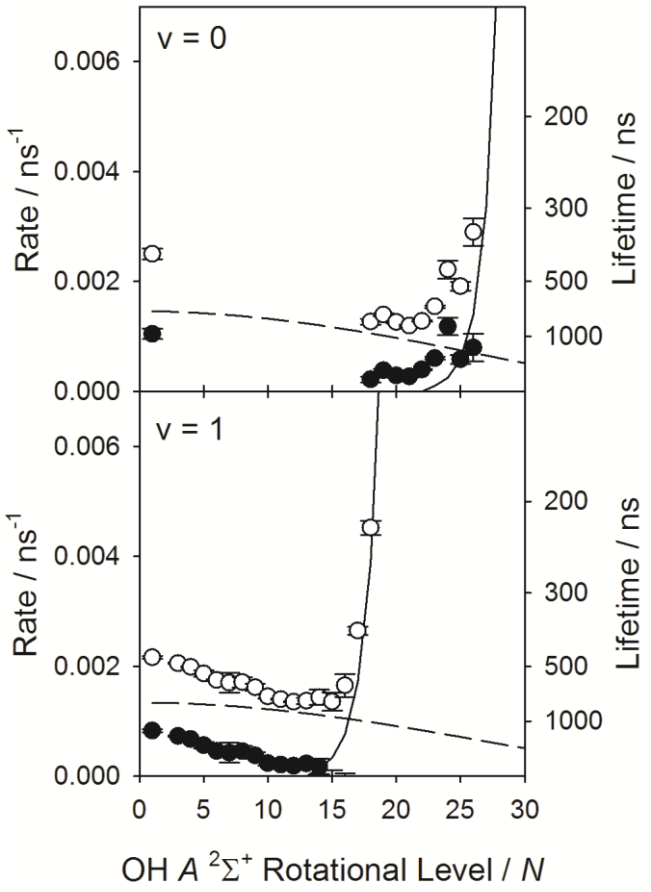

Figure 1. Experimentally determined OH $A\ ^2\Sigma^+$ total decay rates (k_{tot}, ○) for v=0 (top) and v=1 (bottom) as a function of rotational level (N) in the collisional region of the supersonic expansion. Pseudo first-order collisional rates (k_{coll}, ●) are derived from radiative (k_{rad}, dashed line) and predissociative (k_{PD}, solid line) rates from Ref. 37.

similar, but to a lesser extent, than that seen previously in collisions with N_2.[17] These highest N levels are above the energetic threshold to v=1, possibly indicating a rotational (v=0, high N) to vibrational (v=1, low N) energy transfer process. In OH $A\ ^2\Sigma^+$ (v=1), the collisional rate is the sum of the collisional quenching and vibrational energy transfer rates, which cannot be decoupled in this experiment. The collisional rate decreases with increasing N. In the present experiments with Kr, the radiative rate at low N is larger than the collisional rate.

B. OH $A\ ^2\Sigma^+$ Electronic Quenching Cross-Sections.

Absolute, thermally averaged electronic quenching cross-sections at 300 K for OH $A\ ^2\Sigma^+$ by Kr are presented in Fig. 2, which is resolved into two panels for quenching from F_1 (j= N+S) and F_2 (j= N-S) spin-rotation levels of OH $A\ ^2\Sigma^+$. Note that the data presented in Fig. 2 represent a much more extensive data set than that reported in our previous publication.[6] The thermally averaged cross-sections are compared to the results of Hemming *et al.*[5] – note that the spin-rotation level employed was not specified in that work. Agreement with the literature is seen to be excellent and supports the smooth downward trend in σ_Q with N, falling to zero around N = 10. As the OH(A) radical rotates faster, fewer collisions are able to sample the conical intersection region in the HO(A)-Kr well, and as a consequence are unable to undergo electronic quenching. Only a very small difference is observed between the electronic quenching cross-sections for the F_1 and F_2 spin-rotation levels.

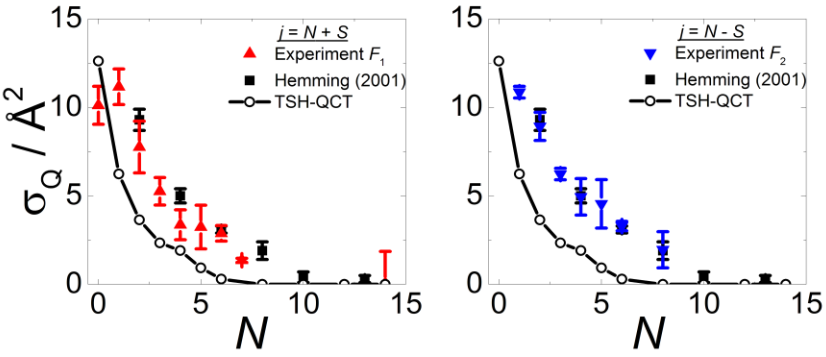

Figure 2. Electronic quenching cross-sections for OH $A\,^2\Sigma^+$ with Kr under thermal conditions at 300 K. Left (red): F_1, right (blue): F_2, black squares: Hemming *et al.*[5] The open circles denote TSH-QCT closed-shell quenching cross-sections. Note that the spin-rotation level employed by Hemming *et al.* is not specified in their paper.

C. OH $X\ ^2\Pi$ Product State Distribution.

Relative populations have been measured for over 40 distinct OH $X\ ^2\Pi$ product quantum states. In some cases, individual OH $X\ ^2\Pi$ levels could not be probed due to spectral congestion, the rapid onset of predissociation at high N especially in v=1, or a large OH $X\ ^2\Pi$ background at low N'' (v''=0) preventing acceptable signal-to-noise ratios during the active background subtraction procedure. The population distribution is shown in Figs. 3 and 4, plotted as a function of OH $X\ ^2\Pi$ internal energy and then again as rotational quantum number.

To aid in analysis of the population distribution, an arbitrary functional form was fit to the distribution after scaling v''=1 to v''=0. A sum of two Fisher-Tippet functions was used here in order to capture the shape of the distribution.[38] The v''=0 and v''=1 distributions have similar shapes, exhibiting a peak around 9 quanta of rotation, a slight dip in population and then a second peak around 17 quanta of rotation. The distribution drops off at high and low N''. The population in specific product states were compared between v''=0 and v''=1. This led to a ratio of ~7 times more population in v''=0 than v''=1.

In v''=0, all four spin-orbit (F_1 and F_2) and Λ-doublet (Π (A') and Π (A'')) states were probed for N''= 11-16. For a given Λ-doublet component, populations in equivalent (same N'') F_1 and F_2 levels were found to be approximately the same within experimental uncertainty. The degree of electron alignment (DEA) is defined as $[P_{\Pi(A')}-P_{\Pi(A'')}]/[P_{\Pi(A')} + P_{\Pi(A'')}]$, which has limiting values of +1 and –1 associated with the unpaired electron in the pπ orbital aligned in and out of the plane of molecular rotation, respectively. The

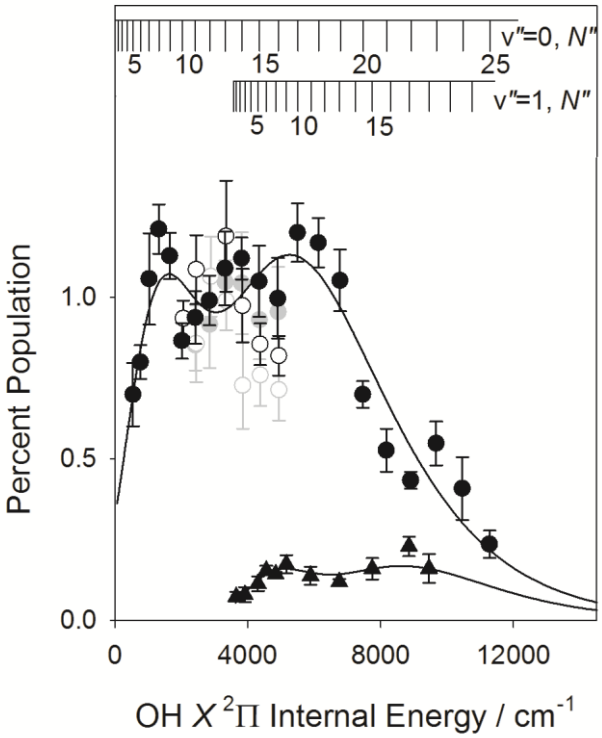

Figure 3. Nascent OH $X\ ^2\Pi$ quantum state distribution observed following quenching of OH $A\ ^2\Sigma^+$ (v=0, N=0) by Kr as a function of OH $X\ ^2\Pi$ internal energy. Percent populations for v''=0 (circles) and v''=1 (triangles) are depicted. The F_1 and F_2 manifolds are shown in filled and open symbols, respectively, with black and grey symbols representing the $\Pi(A')$ and $\Pi(A'')$ Λ-doublets, respectively. The fit through the data is primarily used as a guide to the eye, as described in the text.

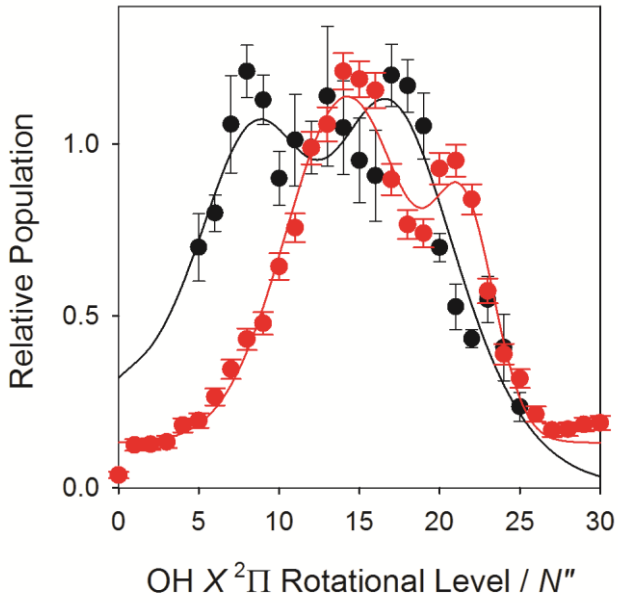

Figure 4. Nascent OH $X\,^2\Pi$ quantum state distribution observed following quenching of OH $A\,^2\Sigma^+$ (v=0, N=0) by Kr as a function of rotational level, N''. For simplification, the $\Pi(A')$ Λ-doublet for v''=0 is depicted as an average of the F_1 and F_2 manifolds (black circles). The OH $X\,^2\Pi$ rotational distribution resulting from QCT surface hopping calculations (red circles), arbitrarily scaled to the peak of the experimental distribution. The same functional form is used to fit both sets of data and is primarily used as a guide to the eye, as described in the text.

DEA was found to be 0.06(7), indicating little to no Λ-doublet propensity. This was tested again at a shortened pump-probe time delay (40 ns) with the same result within experimental uncertainty.

A branching fraction measurement was carried out following analogous studies with other quenching partners.[15-17,19] The amount of initially prepared OH $A\ ^2\Sigma^+$ (v=0, N=0) was compared to four different OH $X\ ^2\Pi$ product levels, two in v''=0 and two in v''=1. Approximately 1.1% of the quenched products are found in N''=13 and 14 of v''=0, 0.12% in N''=13 of v''=1, and 0.16% in N''=15 of v''=1. To determine the total branching to OH $X\ ^2\Pi$ (v''=0, 1) products, the fit to the data is used to estimate the population in unobserved quantum states. Assuming a DEA = 0.06 and equal population in F_1 and F_2 states, approximately 95(7)% of total quenched population can be identified in v''=0 [83(7)%] and v''=1 [12(1)%].

IV. Theoretical Methods and Results

A. Potential Energy Surfaces and Couplings.

The ground $X\ ^2\Pi$ and first excited $A\ ^2\Sigma^+$ states of the OH molecule differ in the filling of the non-bonding $2p_\pi$ and bonding 3σ orbital (formed from the bonding combination of the O $2p_\pi$ and H 1s orbitals). The electronic configuration of the X state is $2p_\pi^3 3\sigma^2$ while that of the A state is $2p_\pi^4 3\sigma^1$. The A state lies 4.06 eV above the ground state.

Approach of the spherically symmetric Kr atom lifts the degeneracy of the $2p_\pi$ orbitals, splitting the Π state into a state which is symmetric (A′) with respect to

reflection in the plane of the three atoms (which we take to be the *yz* plane), with electronic configuration $2p_{\pi x}{}^2 2p_{\pi y}{}^1 3\sigma^2$, and a state which is antisymmetric (A″), with electronic configuration $2p_{\pi x}{}^1 2p_{\pi y}{}^2 3\sigma^2$. We will label these states $\Pi_{A'}$ and $\Pi_{A''}$, respectively. In non-linear geometries approach of the Kr can mix the A′ component of the $X\,^2\Pi$ state with the $A\,^2\Sigma^+$ state, in which the electronic wavefunction has also A′ reflection symmetry. We will label this second A′ state as $\Sigma_{A'}$. This Π/Σ notation for the two diabatic states of A′ reflection symmetry follows earlier work on electronic quenching by Alexander and Corey[39] and Dagdigian *et al.*[40] For illustration, we show contour plots of the OH $\Sigma_{A'}$ (panel a) and $\Pi_{A'}$ (panel b) molecular orbitals discussed above as the Kr atom approaches the relevant states of OH in Fig. 5. The $\Pi_{A''}$ molecular orbital (not shown) is similar to the $\Pi_{A'}$ orbital in panel b, but perpendicular to the triatomic plane.

As mentioned before, last year Chadwick *et al.* reported[6] calculations of the Kr–OH ($A\,^2\Sigma^+$) PES that revealed a deep minimum for collinear Kr–OH approach. These authors characterized the single $\Sigma_{A'}$ PES at the coupled-cluster [RCCSD(T)] level and calculated ro-vibrational bound levels and cross sections for rotational energy transfer (RET) within the $A\,^2\Sigma^+$ state. The calculated RET cross-sections obtained on the single PES surface slightly overestimated the experimental results, which suggested the presence of a collisional quenching pathway, not included in the theoretical model. The *ab initio* PES of Chadwick *et al.*[6] was based on a coupled-cluster method, which is single-reference in nature and cannot describe well the two PES's of A′ symmetry in the

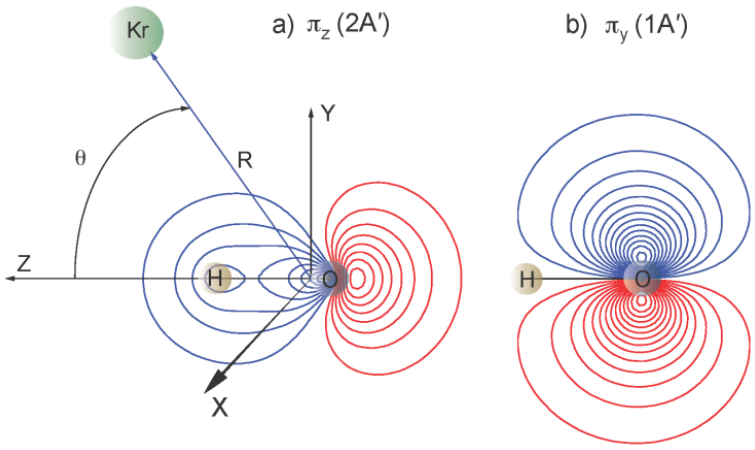

Figure 5. Visualization of the approach of the Kr atom (green sphere) to the (a) OH(*A*) π_z and (b) OH(*X*) π_y HOMO orbitals. The two orbitals are both symmetric (A′) with respect to reflection in the triatomic plane.

region where they cross. Here, we show that the crossing between $\Pi_{A'}$ and $\Sigma_{A'}$ Kr–OH PESs leads to significant non-radiative collisional quenching.

To determine the $\Pi_{A'}$ and $\Sigma_{A'}$ Kr–OH PESs, the coupling between these two diabatic states, and the PES for the single state of A″ reflection symmetry ($\Pi_{A''}$), we used the MOLPRO suite of *ab initio* codes. We maintained the OH distance to be that of isolated OH in the *A* state, r_e=1.0121 Å.[41] We used an augmented correlation-consistent triple-zeta basis set, optimized for all-electron scalar relativistic calculations with Douglas–Kroll integrals (aug-cc-pvtz-DK).[42] Multi-configurational Hartree-Fock (MCSCF) calculations were then used a multi-reference configuration-interaction calculation with inclusion of single and double excitations and, finally, the addition of the Davidson correction (MRCISD+Q) to reduce the error associated with lack of size consistency.

These calculations yield three adiabatic PES's, two of A′ and one of A″ reflection symmetry, which we label 1A′, 2A′, and 1A″. Making use of the quasi-diabatization capability in MOLPRO, we then transform, as defined in the next two equations, the 1A′ and 2A′ adiabatic states into the $\Pi_{A'}$ and $\Sigma_{A'}$ quasi-diabatic basis. The adiabatic and diabatic states of A′ reflection symmetry are related by a 2×2 orthogonal transformation, as follows:

$$\begin{bmatrix} V_{1A'} & 0 \\ 0 & V_{2A'} \end{bmatrix} = \mathbf{C} \begin{bmatrix} V_{\Pi_{A'}} & V_{\Sigma\Pi} \\ V_{\Sigma\Pi} & V_{\Sigma_{A'}} \end{bmatrix} \mathbf{C}^T \tag{1}$$

where

$$\mathbf{C} = \begin{bmatrix} \cos\gamma & \sin\gamma \\ -\sin\gamma & \cos\gamma \end{bmatrix} \tag{2}$$

Here, the mixing angle γ as well as the two diagonal and the off-diagonal diabatic PESs are a function of the three internal coordinates of the OH-Kr system. As expressed in Eqs. (1) and (2), the two adiabatic states represent an orthogonal admixture of the electronic configuration of the *A*-state and the electronic configuration of the A′ component of the *X* state.

In the quasi-diabatization the MCSCF orbitals are first rotated to maximize the overlap with a set of reference orbitals, taken here to be those for collinear KrOH at large Kr–O distance, where the *A* and *X* state are well separated in energy. The three diabatic PESs are then obtained by analysis of the CI coefficients in the basis of configurations built from the rotated orbitals. The third quasi-diabatic state, $\Pi_{A''}$, is unaffected by the adiabatic→quasi-diabatic transformation of the two A′ states, and is identical to the 1A″ adiabatic state. At large OH–Kr distances, the two diabatic and adiabatic states of A′ reflection symmetry become identical and correlate with the OH(*X*)+Kr and OH(*A*)+Kr asymptotes.

In the electronically adiabatic basis, the off-diagonal matrix elements of the derivative operator are responsible for the nonadiabatic coupling between the two states of A′ symmetry. It is easy to show, from Eqs. (1) and (2), that this matrix element – the so-called nonadiabatic coupling matrix element (NACME) – is equal to the derivative of the mixing angle, namely

$$\left\langle 1\mathrm{A}' \middle| \frac{\partial}{\partial q} \middle| 2\mathrm{A}' \right\rangle = \frac{\partial \gamma}{\partial q} \tag{3}$$

where q designates any of the three Jacobi coordinates. Equivalently, we can use the gradient operator to define a nonadiabatic coupling vector

$$\langle 1A' | \vec{\nabla}_q | 2A' \rangle = \vec{\nabla}_q \gamma \tag{4}$$

The PES's were determined on a grid in Jacobi coordinates, R (ranging from 2.75 to 15 bohr) and θ (ranging from 0° to 180° every 20° including 90°). To obtain interaction energies, we subtract the energy at a large separation between Kr and OH. The calculated interaction energies were not corrected for basis-set superposition error. Figure 6 shows radial cuts of the resultant adiabatic and diagonal diabatic PESs of A′ symmetry in near linear configurations. Figure 7 shows a surface plot of the two diabatic states, oriented to show clearly the small region of the crossing. This figure represents a 2-D extension of Fig. 6. Figure 8 displays a surface plot of the $V_{\Sigma\Pi}$ PES, which is the off-diagonal coupling in the diabatic basis.

In linear geometry, the $V_{\Sigma_{A'}}$ PES is crossed by the repulsive wall of the $V_{\Pi_{A'}}$ PES at energies below the Kr+OH(A) asymptote, as shown in Fig. 6 for θ = 170°. It is the presence of the deep, close-in Kr–OH(A) minimum that allows this crossing. In the other collinear geometry (Kr–HO) a crossing occurs, but at much higher energy far above the Kr+OH(A) asymptote, as illustrated in Fig. 6 for θ = 10°. The conical intersections in the two linear geometries become avoided crossings in bent geometries, as shown in Fig. 6.

This mixing of the two diabatic states provides a mechanism for electronic quenching of the OH A state in collisions with Kr. We observe in Fig. 6 that this crossing

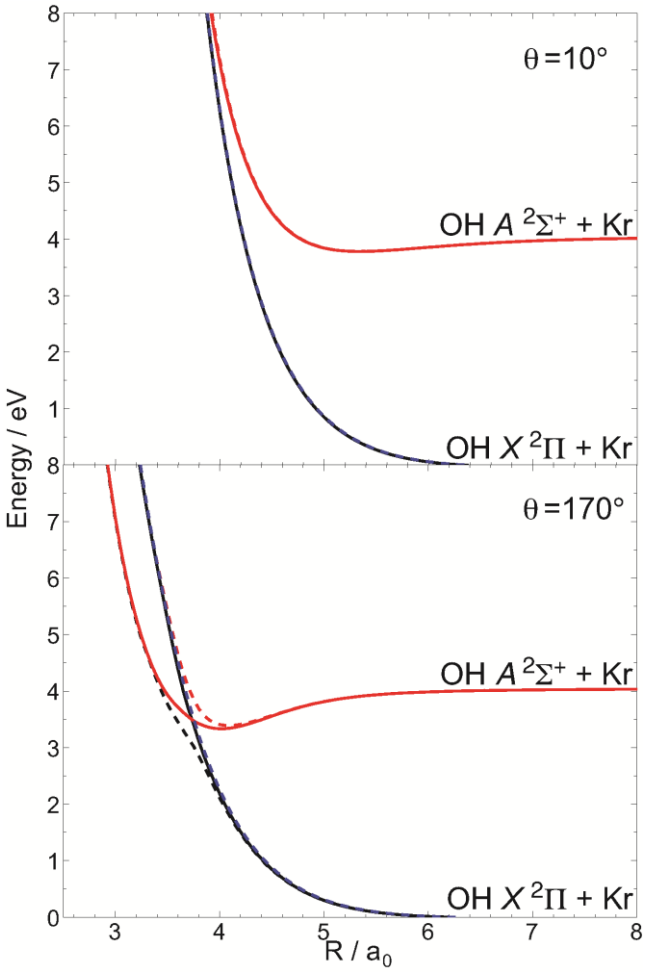

Figure 6. OH ($X\ ^2\Pi$, $A\ ^2\Sigma^+$) + Kr MRCISD+Q potential energy curves for the two states of A′ reflection symmetry, $\Pi_{A'}$ (solid black) and $\Sigma_{A'}$ (solid red), as a function of the OH–Kr center-of-mass distance for near collinear OH–Kr (top panel) and HO–Kr (bottom panel) orientations. The black and red dashed lines indicate the 1A′ and 2A′ electronically adiabatic potential curves, and the blue dashed line is the 1A″ adiabatic potential curve.

will be accessible for thermal or hyperthermal collisions only for near-linear KrOH geometries (e.g. θ = 170° in Fig. 6). The extent of this mixing is governed by the strength of the coupling ($V_{\Sigma\Pi}$) between the $\Pi_{A'}$ and $\Sigma_{A'}$ diabats.

B. Trajectory Surface Hopping Calculations

The quasiclassical trajectory (QCT) method employed in this work is similar to that described in previous papers,[6,43] and only those details relevant to the present work are included here. Single-PES QCT calculations[6] were performed on the upper electronically-adiabatic PES. We ran batches of 20000 trajectories for each initial state, at a collision energy of 0.039 eV (314.5 cm^{-1}). The initial distance between the incoming atom and the center of mass of the diatom was chosen to be 12 Å. The assignment of the final internal levels of the OH, N_f (both in the inelastic case or in the quenching channel), were carried out by equating the classical rotational angular momentum to $\hbar\left[N_f\left(N_f + 1\right)\right]^{1/2}$. Real values of N_f are rounded to the nearest integer.

The non-adiabatic classical calculations were carried out by the Trajectory Surface Hopping (TSH) method[44] using the *fewest switches* algorithm proposed by Tully.[45] Trajectories are propagated classically on the electronically adiabatic 1A′ and 2A′ PESs. Trajectories were started on the upper PES. In the QCT-TSH method, the kinetic coupling between these two states is the product of the NACMEs [Eq. (3)] and the nuclear velocities. As shown in Eq. (3), the NACMEs are derivatives of the diabatic mixing angles, which can be evaluated [Eqs. (1) and (2)] from the off-diagonal diabatic $V_{\Sigma\Pi}$ PES and the adiabatic potentials. The evolution with the nuclear motion of the

electronic population in the two states of A′ reflection symmetry was controlled by integrating the time-dependent Liouville equation of the density matrix with a predictor-corrector Adams-Bashforth-Moulton algorithm, simultaneously to the trajectory propagation.

Fast variations of the electronic populations can cause trajectories to jump from the current electronic state to any other of the same symmetry. We found that a time step of 0.05 fs was sufficiently small to ensure the conservation of the trace of the density matrix – the total electronic population – as well as the total energy of the system. Batches of 3×10^5 trajectories were run for each initial level at a collision energy of 39 meV. A trajectory can only experience a hop if the translational energy is at least equal to the difference between the upper and lower adiabatic PES; otherwise the hop is rejected.

Also in order to conserve the total energy of the system after a transition to the other adiabatic PES's, a kinetic energy correction is performed by rescaling the momentum of each nucleus in the direction of the non-adiabatic coupling vector [Eq. (4)].[45,46] If the velocity component along the non-adiabatic coupling vector is not enough to overcome the energy gap, the jump is forbidden. In the strong interaction region (the region of the Kr–OH well) trajectories were found to undergo several hops (usually from 1 to 4) between the 1A′ and 2A′ PESs. An even number of switches results in an inelastic transition on the original PES. An odd number of jumps gives rise to a quenched trajectory from the excited 2A′ to the ground 1A′state.

Figure 4 displays the comparison between the experimental and QCT-TSH rotational distribution of the nascent OH $X\ ^2\Pi$ originated by quenching from the lowest rotational level (N=0) of the excited OH $A\ ^2\Sigma^+$ state with Kr as the collision partner. At a fixed collision energy of E_{coll} = 39 meV, the total quenching cross section from the N=0 level was found to be σ_Q(TOT) = 12.8 Å^2. As commented on above, the theoretical prediction agrees with the experimental rotational distribution fairly well.

We also carried out TSH-QCT calculations for other initial OH $A\ ^2\Sigma^+$ rotational levels, N = 0–14, always at a collision energy of 39 meV. The QCT-TSH total quenching cross-sections, summed over final levels, are compared with experiment in Fig. 2 (open circles). Note that these calculations do not include the electron spin. Hence, identical results are displayed for both OH fine-structure levels in both panels of the figure.

The calculations successfully capture the correct order of magnitude for the quenching cross-sections and the trend with increasing N, although the size of the quenching cross-section is somewhat underestimated, especially with increasing OH rotation. The present TSH calculations consider only transitions between the upper and lower A′ states induced only by the mixing of the two dominant electron occupancies of these states. Specifically not included is Coriolis coupling between the nominally Σ and Π states. This will provide an additional pathway for collisional quenching of the 2A′ state. Since the magnitude of Coriolis coupling will depend on the OH rotational quantum number, it will lead to a selective increase in quenching for the higher rotational levels. If this effect were sufficiently large, it will bring the theoretical results into a better agreement with the experiment.

V. Discussion

Collisional electronic quenching of OH $A\ ^2\Sigma^+$ by Kr results in OH $X\ ^2\Pi$ products formed primarily in their lowest vibrational level with a substantial degree of rotational excitation and essentially no pπ orbital alignment (or Λ-doublet propensity). Branching fraction measurements for specific OH $X\ ^2\Pi$ product states were used to scale the overall product state distribution, which then accounts for nearly all of the quenching events. These experimental observables can be understood in terms of the properties of the potential energy surfaces, in particular the diabatic coupling and angular gradients in the vicinity of avoided crossing.

The minimal vibrational excitation is consistent with the small change in OH bond length between the ground and excited electronic states (r_e = 0.9697 and 1.0121 Å, respectively). The degree of vibrational excitation (83% and 12% in v''=0 and 1, respectively) agrees well with the square of the vibrational overlap between OH A (v=0) and OH X (v''=0) or (v''=1) (Franck-Condon factors), based on which we would predict a relative OH $X\ ^2\Pi$ vibrational distribution of 90.5% in v''=0 and 9.2% in v''=1. Since quenching of OH $A\ ^2\Sigma^+$ (v=0) by Kr leads overwhelmingly to OH X (v''=0) products, the approximation of a frozen OH distance, made here in our theoretical simulations, should be justified.

The same quenching process results in significant rotational excitation with an average rotational energy $\langle E_{rot} \rangle$ = 4400 cm^{-1} and average rotational quantum number $\langle N'' \rangle$ = 14 in v''=0. The QCT calculations predict a similarly high degree of rotational

excitation with $\langle E_{rot} \rangle$ = 5300 cm^{-1} and $\langle N'' \rangle$ = 18. The overall shape of the QCT product rotational distribution is quite similar to the experimental result and the same fitting function (sum of two Fisher-Tippet functions) has been used to guide the eye in Fig. 4. Based on this fit, the QCT distribution peaks at ~14 quanta of OH rotation, followed by a slight dip, and then has a secondary peak at ~21 quanta of OH rotation. The significant rotational excitation seen here in our experimental and QCT theoretical studies is a characteristic feature in nonreactive quenching of OH $A\ ^2\Sigma^+$ by many molecular collision partners.[13-17,19] Notwithstanding, only ~1/8 of the available energy appears as rotation.

Features of the OH + Kr potential energy surfaces provide insight into the mechanism for quenching and the origin of the degree of rotational excitation seen in the OH $X\ ^2\Pi$ product state distributions. As revealed by Fig. 7, at low collision energies the crossing between the V_Σ and V_Π potentials is only accessible for near linear Kr–OH configurations ($\theta \geq 160°$). A barrier on the excited state surface separates the OH–Kr and Kr–OH configurations and restricts access to the narrow Kr–OH well region where the ground and excited diabatic surfaces cross. The strong dependence of quenching on OH $A\ ^2\Sigma^+$ orientation, specifically favoring the O-side of OH pointing toward Kr, has been seen in theoretical studies involving several molecular partners, most notably the OH + H_2 and OH + N_2 systems.[17,22]

On the excited-state surface, an attractive interaction directs the approaching partners towards either the linear HO–Kr configuration, the global minimum, or toward the linear OH–Kr configuration, a local minimum. In the deeper HO–Kr well, a narrow

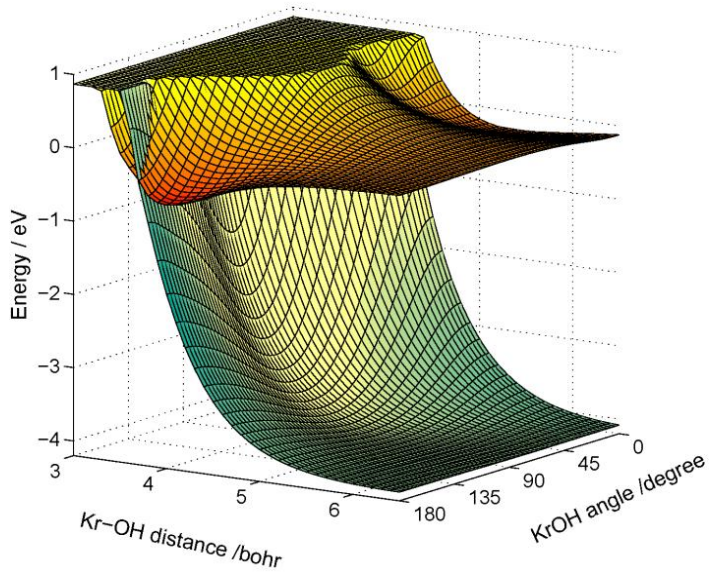

Figure 7. Surface plot relative to the OH $A\ ^2\Sigma^+$ + Kr asymptote of the $\Pi_{A'}$ (green) and $\Sigma_{A'}$ (orange) diabatic states as a function of the OH to Kr center of mass distance (R, a_0) and the angle of OH with respect to Kr (θ, degrees). The angular coordinate is defined in Fig. 5, where 0° and 180° correspond to linear OH–Kr and HO–Kr, respectively.

angular region about linearity is intersected by the ground state surface at small *R*. The collision partners that access this narrow region are funneled down to the ground-state surface, where they experience a steep angular gradient away from linear geometry. The strong torque resulting from this gradient results in significant rotational excitation of the OH $X\,^2\Pi$ products. Similar angular gradients on the potentials have been identified previously in the OH + H_2 system and qualitatively linked to the degree of rotational excitation of the OH products.[11,13-20,27-29] On the other hand, the region of coupling between the ground and excited states is limited to near-linear geometry (Fig. 7), which sets a limit to the amount of rotational excitation. This would explain why only 1/8 of the total available energy appears as OH rotation.

The coupling between the surfaces also plays an important role in the quenching events. The size of the off-diagonal coupling in the quasi-diabatic basis, shown in Fig. 8, illustrates the strength of the mixing between the ground and excited A′ states. The coupling vanishes in linear geometry, increases to a maximum near 120° at 3.1–3.2 a_0, decreases in magnitude, and then changes sign in near perpendicular geometry. The region of the strongest coupling is not energetically accessible. Nevertheless, coupling occurs throughout the crossing region in the HO-Kr well region with greater strength for increasingly bent configurations, thereby favoring these geometries in quenching events.

The surface-hopping QCT calculations presented here include only two potential energy surfaces, the ground and excited A′ states. Agreement with experimental quenching cross-sections is reasonable, but the theory underestimates somewhat the true extent of electronic quenching. Possibly expanding the theoretical treatment to include

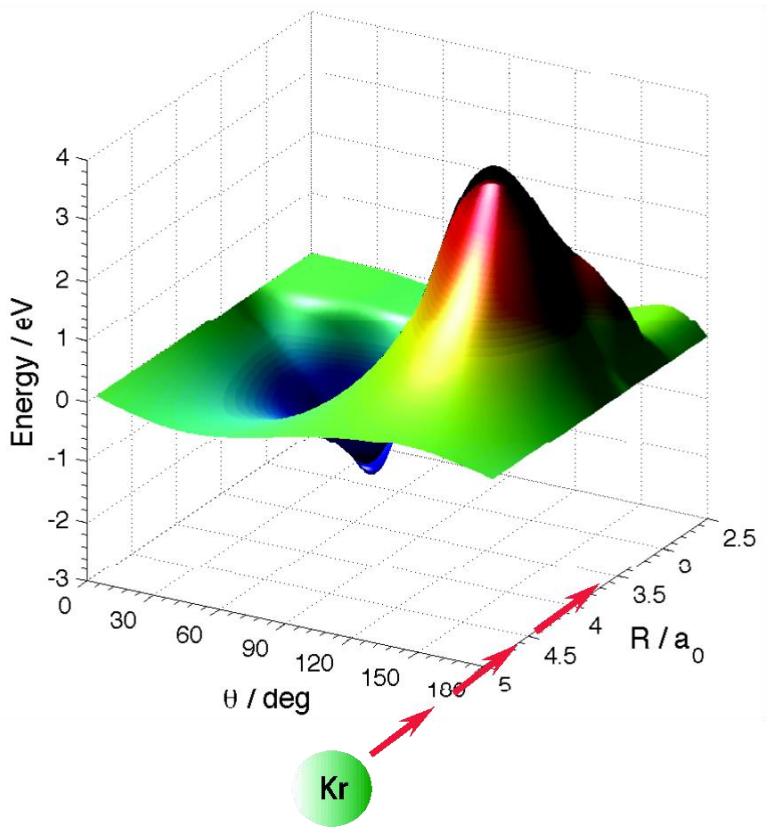

Figure 8. MRCISD+Q diabatic coupling $V_{\Sigma\Pi}$ PES. The coupling vanishes in linear geometry and changes sign in near perpendicular geometry.

the lowest A″ surface will increase the efficiency of quenching, leading to better agreement with experiment. In particular, the overall KrOH rotational motion will couple the excited $\Sigma_{A'}$ PES to the $\Pi_{A''}$ PES. Experimentally, quenched OH products are distributed equally over the two Λ-doublet components of each rotational level. This suggests that an accurate model of the distribution of the OH(*X*) products among the fine-structure and Λ-doublet multiplets will require inclusion of both the $\Pi_{A'}$ and $\Pi_{A''}$ PESs.

VI. Conclusions

Experiment reveals that OH $A\ ^2\Sigma^+$ is efficiently quenched by collisions with Kr, leading to OH $X\ ^2\Pi$ products in $v''=0$ and to a much lesser extent in $v''=1$. The minimal degree of vibrational excitation is consistent with the small change in OH bond length in its ground and excited states, with nearly diagonal Franck-Condon overlap. The quenched products exhibit a significant degree of rotational excitation. This is well predicted by quasi-classical trajectory calculations based on *ab initio* PESs.

We interpret the quenching in terms of crossings between these PESs. The calculated PES's associated with the two electronic states of A′ reflection symmetry cross in linear KrOH geometry, but undergo strong coupling as the triatomic system bends. This coupling gives rise to efficient population transfer from OH $A\ ^2\Sigma^+$ ($v=0$, $N=0$) to OH $X\ ^2\Pi$ (v'', N'') products. The crossing region is accessible at thermal or hyperthermal energies due to the deep well in the OH $A\ ^2\Sigma^+$ – Kr PES.

Classical-trajectory, surface-hopping calculations which include the coupling between the two A′ electronic states are able to account qualitatively for the electronic

quenching cross sections and OH $X\,^2\Pi$ level populations observed experimentally. However, a careful comparison with experiment suggests that couplings to the lowest A″ PES might be important. Similar quantum simulations of the electronic quenching are in progress, the results of which will be presented elsewhere.

Acknowledgements

The research at the University of Pennsylvania was supported by the Office of Basic Energy Sciences of the Department of Energy. M.H.A. and P.J.D. acknowledge the support of the National Science Foundation through grant no. CHE-1213332. F.J.A. acknowledges the financial support by the Spanish Ministry of Education and Science under Grant Nos. CTQ2008-02578/BQU, CSD2009-00038, and CTQ2012-37404-C02. M.B. thanks the EPSRC (U.K.) for Programme Grant No. EP/G00224X/1, which funded part of this research.

References

(1) Crosley, D. R. Laser Fluorescence Detection of Atmospheric Hydroxyl Radicals. *Advanced Series in Physical Chemistry* **1995**, *3*, 256-317.

(2) Creasey, D. J.; Heard, D. E.; Pilling, M. J.; Whitaker, B. J.; Berzins, M.; Fairlie, R. Visualization of a Supersonic Free-Jet Expansion Using Laser-Induced Fluorescence Spectroscopy. Application to the Measurement of Rate Constants at Ultralow Temperatures. *Appl. Phys. B: Lasers Opt.* **1997**, *65*, 375-391.

(3) Heard, D. E.; Henderson, D. A. Quenching of OH($A^2\Sigma^+$, v' = 0) by Several Collision Partners between 200 and 344 K. Cross-Section Measurements and Model Comparisons. *Phys. Chem. Chem. Phys.* **2000**, *2*, 67-72.

(4) Hemming, B. L.; Crosley, D. R. Rotational-Level Dependence of OH $A^2\Sigma^+$ Quenching at 242 and 196 K. *J. Phys. Chem. A* **2002**, *106*, 8992-8995.

(5) Hemming, B. L.; Crosley, D. R.; Harrington, J. E.; Sick, V. Collisional Quenching of High Rotational Levels in $A^2\Sigma^+$ OH. *J. Chem. Phys.* **2001**, *115*, 3099-3104.

(6) Chadwick, H.; Brouard, M.; Chang, Y. P.; Eyles, C. J.; Perkins, T.; Seamons, S. A.; Kłos, J.; Alexander, M. H.; Aoiz, F. J. A New Potential Energy Surface for OH($A^2\Sigma^+$)-Kr: The van der Waals Complex and Inelastic Scattering. *J. Chem. Phys.* **2012**, *137*, 154305.

(7) Hogan, P.; Davis, D. D. Electronic Quenching and Vibrational Relaxation of the OH($A^2\Sigma^+$, v'=1) State. *J. Chem. Phys.* **1975**, *62*, 4574-4576.

(8) Hogan, P.; Davis, D. D. Comments on "Electronic Quenching and Vibrational Relaxation of the OH($A^2\Sigma^+$, v' = 1) state". *J. Chem. Phys.* **1976**, *64*, 3901.

(9) Lengel, R. K.; Crosley, D. R. Comment on "Electronic Quenching and Vibrational Relaxation of the OH($A^2\Sigma^+$, v' = 1) State". *J. Chem. Phys.* **1976**, *64*, 3900-3901.

(10) Wysong, I. J.; Jeffries, J. B.; Crosley, D. R. Quenching of $A^2\Sigma^+$ OH at 300K by Several Colliders. *J. Chem. Phys.* **1990**, *92*, 5218-5222.

(11) Ortiz-Suárez, M.; Witinski, M. F.; Davis, H. F. Reactive Quenching of OH($A^2\Sigma^+$) by D_2 Studied Using Crossed Molecular Beams. *J. Chem. Phys.* **2006**, *124*, 201106.

(12) Hancock, G., personal communication.

(13) Cleary, P. A.; Dempsey, L. P.; Murray, C.; Lester, M. I.; Kłos, J.; Alexander, M. H. Electronic Quenching of OH $A^2\Sigma^+$ Radicals in Single Collision Events with Molecular Hydrogen: Quantum State Distribution of the OH $X^2\Pi$ Products. *J. Chem. Phys.* **2007**, *126*, 204316.

(14) Dempsey, L. P.; Murray, C.; Cleary, P. A.; Lester, M. I. Electronic Quenching of OH $A^2\Sigma^+$ Radicals in Single Collision Events with H_2 and D_2: A Comprehensive Quantum State Distribution of the OH $X^2\Pi$ Products. *Phys. Chem. Chem. Phys.* **2008**, *10*, 1424-1432.

(15) Dempsey, L. P.; Murray, C.; Lester, M. I. Product Branching between Reactive and Non-Reactive Pathways in the Collisional Quenching of OH $A^2\Sigma^+$ Radicals by H_2. *J. Chem. Phys.* **2007**, *127*, 151101.

(16) Dempsey, L. P.; Sechler, T. D.; Murray, C.; Lester, M. I. Quantum State Distribution of the OH $X^2\Pi$ Products from Collisional Quenching of OH $A^2\Sigma^+$ by O_2 and CO_2. *J. Phys. Chem. A* **2009**, *113*, 6851-6858.

(17) Dempsey, L. P.; Sechler, T. D.; Murray, C.; Lester, M. I.; Matsika, S. State-Resolved Distribution of OH $X^2\Pi$ Products Arising from Electronic Quenching of OH $A^2\Sigma^+$ by N_2 *J. Chem. Phys.* **2009**, *130*, 104307.

(18) Lehman, J. H.; Bertrand, J. L.; Stephenson, T. A.; Lester, M. I. Reactive Quenching of OD $A^2\Sigma^+$ by H_2: Translational Energy Distributions for H- and D-Atom Product Channels. *J. Chem. Phys.* **2011**, *135*, 144303.

(19) Lehman, J. H.; Dempsey, L. P.; Lester, M. I.; Fu, B.; Kamarchik, E.; Bowman, J. M. Collisional Quenching of OD $A^2\Sigma^+$ by H_2: Experimental and Theoretical studies of the State-Resolved OD $X^2\Pi$ Product Distribution and Branching Fraction. *J. Chem. Phys.* **2010**, *133*, 164307.

(20) Lehman, J. H.; Lester, M. I.; Yarkony, D. R. Reactive Quenching of OH $A^2\Sigma^+$ by O_2 and CO: Experimental and Nonadiabatic Theoretical Studies of H- and O-Atom Product Channels. *J. Chem. Phys.* **2012**, *137*, 094312.

(21) Alexander, M. H.; Andresen, P.; Bacis, R.; Bersohn, R.; Comes, F. J.; Dagdigian, P. J.; Dixon, R. N.; Field, R. W.; Flynn, G. W.; Gericke, K.-H.; Grant, E. R.; Howard, B. J.; Huber, J. R.; King, D. S.; Kinsey, J. L.; Kleinermanns, K.; Kuchitsu, K.; Luntz, A. C.; McCaffery, A. J.; Pouilly, B.; Reisler, H.; Rosenwaks, S.; Rothe, E. W.; Shapiro, M.; Simons, J. P.; Vasudev, R.; Wiesenfeld, J. R.; Wittig, C.; Zare, R. N. A Nomenclature for Λ-Doublet Levels in Rotating Linear Molecules. *J. Chem. Phys.* **1988**, *89*, 1749-1753.

(22) Hoffman, B. C.; Yarkony, D. R. The Role of Conical Intersections in the Nonadiabatic Quenching of OH($A^2\Sigma^+$) by Molecular Hydrogen. *J. Chem. Phys.* **2000**, *113*, 10091-10099.

(23) Lester, M. I.; Loomis, R. A.; Schwartz, R. L.; Walch, S. P. Electronic quenching of OH $A^2\Sigma^+$ (v' = 0, 1) in complexes with hydrogen and nitrogen. *J. Phys. Chem. A* **1997**, *101*, 9195-9206.

(24) Yarkony, D. R. Current Issues in Nonadiabatic Chemistry. *J. Phys. Chem.* **1996**, *100*, 18612-18628.

(25) Yarkony, D. R. Substituent Effects and the Noncrossing Rule: The Importance of Reduced Symmetry Subspaces. I. The Quenching of OH($A^2\Sigma^+$) by H_2. *J. Chem. Phys.* **1999**, *111*, 6661-6664.

(26) Miller, S. M.; Clary, D. C.; Kliesch, A.; Werner, H. J. Rotationally Inelastic and Bound State Dynamics of H_2-OH($X^2\Pi$). *Mol. Phys.* **1994**, *83*, 405-428.

(27) Bowman, J. M.; Czako, G.; Fu, B. High-dimensional Ab Initio Potential Energy Surfaces for Reaction Dynamics Calculations. *Phys. Chem. Chem. Phys.* **2011**, *13*, 8094-8111.

(28) Fu, B.; Kamarchik, E.; Bowman, J. M. Quasiclassical Trajectory Study of the Postquenching Dynamics of OH $A^2\Sigma^+$ by H_2/D_2 on a Global Potential Energy Surface. *J. Chem. Phys.* **2010**, *133*, 164306.

(29) Kamarchik, E.; Fu, B. N.; Bowman, J. M. Communication: Classical Trajectory Study of the Postquenching Dynamics of OH $A^2\Sigma^+$ by H_2 Initiated at Conical Intersections. *J. Chem. Phys.* **2010**, *132*, 091102.

(30) Zhang, P. Y.; Lu, R. F.; Chu, T. S.; Han, K. L. Nonadiabatic Quantum Reactive Scattering of the OH($A^2\Sigma^+$) + D_2. *J. Chem. Phys.* **2010**, *133*, 174316.

(31) Zhang, P. Y.; Lu, R. F.; Chu, T. S.; Han, K. L. Quenching of OH($A^2\Sigma^+$) by H_2 through Conical Intersections: Highly Excited Products in Nonreactive Channel. *J. Phys. Chem. A* **2010**, *114*, 6565-6568.

(32) Carter, C. C.; Lee, H. S.; McCoy, A. B.; Miller, T. A. The Structure of Floppy Molecules: the Rg.XH/D (Rg = Ar, Ne, and Kr, X = O or S) Family of Complexes. *J. Molec. Struct.* **2000**, *525*, 1-45.

(33) Carter, C. C.; Miller, T. A.; Lee, H. S.; Korambath, P. P.; McCoy, A. B.; Hayes, E. F. High Resolution Electronic Spectroscopy of Kr.OH/D and an Empirical Potential Energy Surface. *J. Chem. Phys.* **1999**, *110*, 1508-1520.

(34) Fei, S. L.; Zheng, X. N.; Heaven, M. C. Electronic Spectroscopy and Vibrational Predissociation Dynamics of OH-Kr and OD-Kr. *J. Chem. Phys.* **1992**, *97*, 1655-1663.

(35) Lemire, G. W.; Sausa, R. C. Detection and Spectroscopic Studies of Gas-Phase OH-Kr by Laser-Induced Fluorescence. *J. Phys. Chem.* **1992**, *96*, 4821-4824.

(36) Brouard, M.; Bryant, A.; Chang, Y.-P.; Cireasa, R.; Eyles, C. J.; Green, A. M.; Marinakis, S.; Aoiz, F. J.; Kłos, J. Collisional Depolarization of OH(A) with Ar: Experiment and Theory. *J. Chem. Phys.* **2009**, *130*, 044306.

(37) Luque, J.; Crosley, D. R. LIFBASE: Database and Spectral Simulation Program (Version 1.6). *SRI International Report MP 99-009* **1999**.

(38) *Handbook of Mathematical Functions with Formulas, Graphs and Mathematical Tables*; Abramowitz, M.; Stegun, I., Eds.; Dover Publications: New York, 1972.

(39) Alexander, M. H.; Corey, G. C. Collision-Induced Transitions between $^2\Pi$ and $^2\Sigma$ States of Diatomic Molecules - Quantum Theory and Collisional Propensity Rules. *J. Chem. Phys.* **1986**, *84*, 100-113.

(40) Dagdigian, P. J.; Patel-Misra, D.; Berning, A.; Werner, H.-J.; Alexander, M. H. A Joint Experimental and Theoretical study of $A^2\Pi$ - $X^2\Sigma^+$ Electronic Energy Transfer in the CN Molecule Induced by Collisions with He. *J. Chem. Phys.* **1993**, *98*, 8580-8592.

(41) Huber, K. P.; Herzberg, G. *Molecular Spectra and Molecular Structure. IV. Constants of Diatomic Molecules*; Van Nostrand Reinhold: New York, 1979.

(42) Wilson, A. K.; Woon, D. E.; Peterson, K. A.; Dunning, T. H., Jr. Gaussian Basis Sets for Use in Correlated Molecular Calculations. IX. The Atoms Gallium through Krypton. *J. Chem. Phys.* **1999**, *110*, 7667-7676.

(43) Aoiz, F. J.; Brouard, M.; Eyles, C. J.; Kłos, J.; de Miranda, M. P. The Collisional Depolarization of $^{2S+1}\Sigma$ Radicals by Closed Shell Atoms: Theory and Application to $OH(A^2\Sigma^+)$ + Ar. *J. Chem. Phys.* **2009**, *130*, 044305.

(44) Tully, J. C.; Preston, R. K. Trajectory Surface Hopping Approach to Nonadiabatic Molecular Collisions: The Reaction of H^+ with D_2. *J. Chem. Phys.* **1971**, *55*, 562-572.

(45) Tully, J. C. Molecular Dynamics with Electronic Transitions. *J. Chem. Phys.* **1990**, *93*, 1061-1071.

(46) Fabiano, E.; Keal, T. W.; Thiel, W. Implementation of Surface Hopping Molecular Dynamics using Semiempirical Methods. *Chem. Phys.* **2008**, *349*, 334-347.

CHAPTER 6
Ion Imaging Studies of the Photodissociation Dynamics of CH_2I_2 at 248 nm

The experimental research presented in this chapter was performed at the University of Pennsylvania. This manuscript has been submitted for publication in *Chemical Physics Letters*.

Reference: J. H. Lehman, H. Li, M. I. Lester, *Chem. Phys. Lett.*, submitted (2013).

I. Introduction

Recently, there has been renewed interest in the photodissociation dynamics of CH_2I_2 at 248 nm (and other convenient laser wavelengths) because the CH_2I product is utilized in an alternative synthetic route to generate the simplest Criegee intermediate, CH_2OO, for laboratory studies:[1-4]

$$CH_2I_2 + 248\ nm \rightarrow CH_2I + I/I^*$$

$$CH_2I + O_2 \rightarrow CH_2OO + I$$

High level *ab initio* calculations indicate that the latter step is a near thermoneutral process,[5] suggesting that any internal excitation in the CH_2I fragment is likely to be carried over into internal excitation of the CH_2OO intermediate. In the atmosphere, the CH_2OO intermediate is generated from ozonolysis of ethene and asymmetric alkenes such as 1-propene, where it is also formed with a large excess of internal excitation.[6-8] Depending on the degree of internal excitation, the Criegee intermediate may undergo unimolecular processes including decomposition and isomerization, collisional stabilization, and/or bimolecular reactions.[8,9] The present study aims to fully characterize the internal excitation of the nascent CH_2I fragments from 248 nm photolysis of CH_2I_2 using state-of-the-art methods.

The photodissociation dynamics of alkyl iodides has been investigated for decades both in the gaseous and condensed phases.[10-13] A portion of the room-temperature UV absorption spectrum of CH_2I_2, deconvoluted into four partially overlapping Gaussian bands, is reproduced in Figure 1.[14] Most of the prior experimental and theoretical work has focused on the photodissociation dynamics of

CH_2I_2 following excitation from the ground *X* A_1 state into the two lowest energy bands that comprise the dominant spectral feature, which are attributed to two repulsive states of B_1 symmetry, matching the assignments of a simple exciton model developed by Bersohn and coworkers in 1975.[15-20] The spectral breadth is assumed to arise from the repulsive nature of the excited electronic states.

Much less is known regarding the photodissociation dynamics of CH_2I_2 upon excitation at 248 nm into the third absorption band, which is the focus of the present investigation. The simple exciton model attributes this third band to an excited electronic state of B_2 and/or A_1 symmetry.[16] More recent theoretical work predicts an excited state of purely A_1 character, but it should be noted that the assignments of lower electronic states also differ from the exciton model.[20] Both the B_2 and A_1 electronic states correlate asymptotically with $CH_2I + I^*$ ($^2P_{1/2}$) products.[16]

Electronic excitation of CH_2I_2 at 248 nm can result in dissociation to several energetically accessible singlet channels:

$$CH_2I_2\ X\ A_1 + h\nu\ (248\ nm) \rightarrow CH_2I + I\ (^2P_{3/2}) \quad (1)$$

$$\rightarrow CH_2I + I^*\ (^2P_{1/2}) \quad (2)$$

$$\rightarrow CH_2 + I_2 \quad (3)$$

$$\rightarrow CH_2 + I\ (^2P_{3/2}) + I\ (^2P_{3/2}) \quad (4)$$

Prior studies have shown that pathways (1) and (2) are the primary dissociation processes.[21,22] The quantum yield for I^* ($^2P_{1/2}$) products in channel (2) is 46%.[21,23] Channel (3) is a minor channel with a quantum yield of 0.004.[24] Pathway (4) is energetically accessible (E_{avl} = 1.4 kcal mol^{-1}),[21] but has not been distinguished from

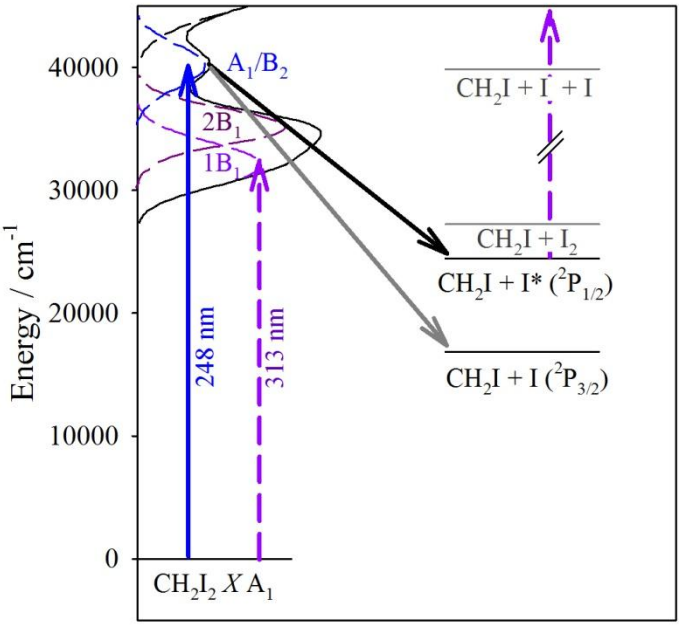

Figure 1. Schematic energetic diagram for CH_2I_2 photodissociation following absorption at 248 nm (blue solid line) and 313 nm (purple dashed line). Previously identified electronic transitions are shown within the CH_2I_2 absorption profile.[14] At 248 nm, 46(4)% of the products are CH_2I and the excited state of iodine [I* $^2P_{1/2}$, black arrow, channel (2)]. The ground state of iodine (I $^2P_{3/2}$, grey arrow) can also be generated [channel (1)], but is not probed in this experiment. The probe laser (313 nm, purple dashed line) is used to ionize the I* product following photodissociation, but can also dissociate CH_2I_2 resulting in one-color background (see Appendix II of this thesis). Channels (3) and (4) are also shown, but are not probed in this work.

channel (1). The multiple pathways observed indicate that more than one electronic state participates in the dissociation process.

Additional information on the photodissociation dynamics of CH_2I_2 at 248 nm under thermal conditions comes from IR emission studies of vibrationally excited CH_2I fragments.[21] Emission was seen in the C-H stretch, CH_2 bend, and C-I stretch regions, indicating highly vibrationally excited CH_2I products, although it should be noted that channels (1) and (2) with I ($^2P_{3/2}$) and I* ($^2P_{1/2}$) products were not separated. The highly excited CH_2I products were detected on a microsecond timescale and various deactivation processes were considered in the analysis.[21] Modeling showed CH_2I fragments produced in a quasicontinuum of vibrational states that accounts for ~85% of the available energy.

The present study reinvestigates the 248 nm photodissociation of CH_2I_2 utilizing velocity map imaging (VMI) with resonance enhanced multiphoton ionization (REMPI) detection of the nascent I* ($^2P_{1/2}$) fragments. The velocity distribution of the I* fragments also contain correlated information on the internal and translational energy distributions of the nascent CH_2I products. The angular distribution of the I* ($^2P_{1/2}$) fragments provides additional detail on the excited electronic state(s) involved in the dissociation dynamics.

II. Experimental Methods

Diiodomethane (CH_2I_2) vapor is entrained in argon carrier gas at a backing pressure of 20 psi and pulsed into a newly constructed VMI vacuum apparatus. The gas

mixture undergoes supersonic expansion and enters the interaction region (unskimmed) approximately 4 cm downstream of the pulsed valve orifice. Here, CH_2I_2 is photodissociated with the 248 nm output of a KrF excimer laser (Coherent, 20 ns, 10 Hz) that crosses the molecular beam at right angles, producing CH_2I and I ($^2P_{3/2}$) or I* ($^2P_{1/2}$). The I* ($^2P_{1/2}$) atoms are then state-selectively ionized via (2+1) REMPI process[25,26] (using the upper state of $5p^25p^46p(^2P_{1/2})$) by a counter-propagating ultraviolet (UV) probe laser at 313 nm, generated by frequency-doubling the output of a Nd:YAG (532 nm, Innolas, 7 ns, 10 Hz) pumped dye laser (DCM, Radiant Dyes, Narrowscan). The probe laser is focused with a 50 cm lens. The photolysis laser is focused with a 60 cm lens after spatially restricting the beam area to a 2 mm diameter and 1.5 mJ/pulse. The power density in the interaction region is on the order of 10^2 W/cm^2, well below the 10^5 W/cm^2 previously used in the work by Baughcum and Leone to reduce multiphoton absorptions.[21] The photolysis and probe lasers are spatially overlapped in the interaction region, but with a 600 ns time delay between the lasers.[27]

Ions are extracted and accelerated onto a position-sensitive detector after passing through a field-free time-of-flight (TOF) region. The electric fields in the extraction region are created by homemade ion optics (parts by Kimball Physics), which are similar to the design by Suits and coworkers.[28] The setup was calibrated from the analysis of O^+ images from the photodissociation of O_2 near 226 nm[29] and achieved approximately 5% velocity resolution. In this work, a pair of extractor and repeller electrodes are used with the repeller voltage (V_R) set at 1500 V and an extractor-to-repeller voltage ratio of 0.74. The detector is fast gated to allow imaging of only I^+ ions. To aid in maintaining a

low operating pressure in the detector region, a flange with a 20 mm hole separates the source and detector regions,[30] and generates some differential pumping between these two chambers (~10^{-6} and ~10^{-7} torr, respectively, under operating conditions). The overall length of the flight path from the interaction region to the detector is 70 cm. The 40 mm 2D position-sensitive detector consists of a pair of microchannel plates (MCP) coupled to a phosphor screen. The images on the phosphor screen are recorded using a charge-coupled-device (CCD) camera (656×492 pixels). Sydor Instruments designed and constructed the coupled detector, CCD camera, and MCP gating module system based on our specifications along with a custom light-tight camera enclosure with access for lens focusing. The MCP/phosphor detector, MCP gating module, and accompanying power supply were manufactured by Photek Ltd., while the CCD camera is from Allied Vision Technologies. Images and time-of-flight information were transferred to a computer and further analyzed via LabVIEW and reconstructed using pBASEX.[31]

The probe UV laser (313 nm) alone can photodissociate CH_2I_2 and subsequently ionize the I* products, and thus a background subtraction scheme is used in data collection. This background signal arising from the probe laser only (one-color) is subtracted every 2000 laser shots from the combined excimer and probe laser induced signal. The excimer laser polarization, selected by a Brewster window, is set parallel to the plane of the detector. The probe laser polarization can be rotated to be either parallel or perpendicular to the plane of the detector. Images were taken under both polarization schemes and will be discussed further in Section III.

The 248 nm excimer laser also dissociates CH_2I_2, resulting in a decrease in the amount of 'background' I* produced from probe laser-induced dissociation of CH_2I_2 at 313 nm. The combination of the one-color background at 313 nm and this decrease can lead to some incomplete image subtraction in the spatial region where the iodine produced by the probe laser alone (one-color) is strongest. This problem was overcome by changing the polarization of the probe laser to perpendicular to the plane of the detector, as described in the results section.

III. Results

Photodissociation of CH_2I_2 at 248 nm can result in ground state iodine I ($^2P_{3/2}$) atoms formed with either CH_2I (1) or CH_2 + I ($^2P_{3/2}$) (4) as cofragments. On the other hand, spin-orbit excited iodine I*($^2P_{1/2}$) can only be formed with CH_2I as its cofragment (2), since the CH_2 + I + I* pathway is not energetically accessible. The I* products from pathway (2) are state-selectively probed in this work, which gives direct information regarding the internal energy distribution of the CH_2I cofragments. Pathway (2) has a significant quantum yield with I* accounting for 46% of the products following 248 nm excitation.[21,23] This indicates the possibility of adiabatic dissociation to correlated I* products from the nominally A_1 and/or B_2 electronic states of CH_2I_2 as well as nonadiabatic processes to form ground state I-atom products.

A. TKER Distribution

Photodissociation of CH_2I_2 at 248 nm, followed by I* ionization via REMPI near 313 nm, with both lasers polarized parallel to the plane of the detector, results in the

image shown in Figure 2b (left image), which includes contributions from both the combined 248 nm + 313 nm lasers and 313 nm alone. The one-color I* signal from 313 nm photolysis/ionization alone is shown in Figure 2a (left image) and described in detail in Appendix II. The one-color I* signal is also evident in Figure 2b. However, there are additional features in the image that are clearly due to the presence of the 248 nm excimer laser. These additional features include a broad region with large kinetic energy release and a smaller, low kinetic energy release portion.

The polarization of the probe laser was then rotated perpendicular to the plane of the detector, resulting in a circular I* image from 313 nm alone (Figure 2a, right image) that improved the image subtraction process discussed below. The total image from the combination of the probe laser at 313 nm, now perpendicularly polarized, and the parallel polarized 248 nm excimer laser (Figure 2b, right image), is reconstructed and the resulting total kinetic energy release (TKER) profile is shown in the left hand side of Figure 2b, where the total translational energy is obtained through conservation of momentum based on the velocity of I*. The TKER profile is fit to a sum of three Gaussian functions. The middle Gaussian profile is the same in both peak position and breadth as one-color I* signal seen in Figure 2a when the 313 nm probe laser (alone) is polarized perpendicular to the detector. The additional components arising from 248 nm photolysis required two Gaussians functions to fit the profile: a large, broad feature at high TKER and a smaller, narrow feature at low TKER, which are discussed in more detail below.

Subtracting the one-color I* signal from 313 nm alone yields I* arising from CH_2I_2 photodissociation at 248 nm followed by state selective ionization by the probe laser, which is shown as the difference image in Figure 2c. The raw image is reconstructed and the resulting TKER profile is shown on the left hand side of Figure 2c. The features evident in the subtracted raw image are more clearly seen in the TKER profile. Fitting the TKER profile from the reconstruction of the subtracted image shows two Gaussians with widths and peak positions analogous to those of the features evident prior to the image subtraction process. The dominant higher TKER feature is centered at 2100 cm^{-1} with a *fwhm* ~2800 cm^{-1} and a smaller, narrow, low TKER feature is peaked at 500 cm^{-1} with a *fwhm* ~500 cm^{-1}.[32]

Small, low TKER features have been seen, but not assigned, in prior one-color photodissociation studies of CH_2I_2 in the 277-304 nm region.[15,19] In the present two-color study, the low TKER product requires both 248 nm and 313 nm light and the 313 nm must be resonant with the I* REMPI transition, indicating that spin-orbit excited iodine atoms are being ionized. We speculate that if CH_2I radicals produced by 248 nm photodissociation were to absorb a second photon of either 313 nm or 248 nm and dissociate to CH_2 + I*, the resultant I* fragments would have low kinetic energy, as suggested in earlier studies.[17] We note that the integrated area of this feature is an order of magnitude smaller than the larger feature at higher TKER and does not influence the results derived from the dominant peak, and thus will not be considered further here.

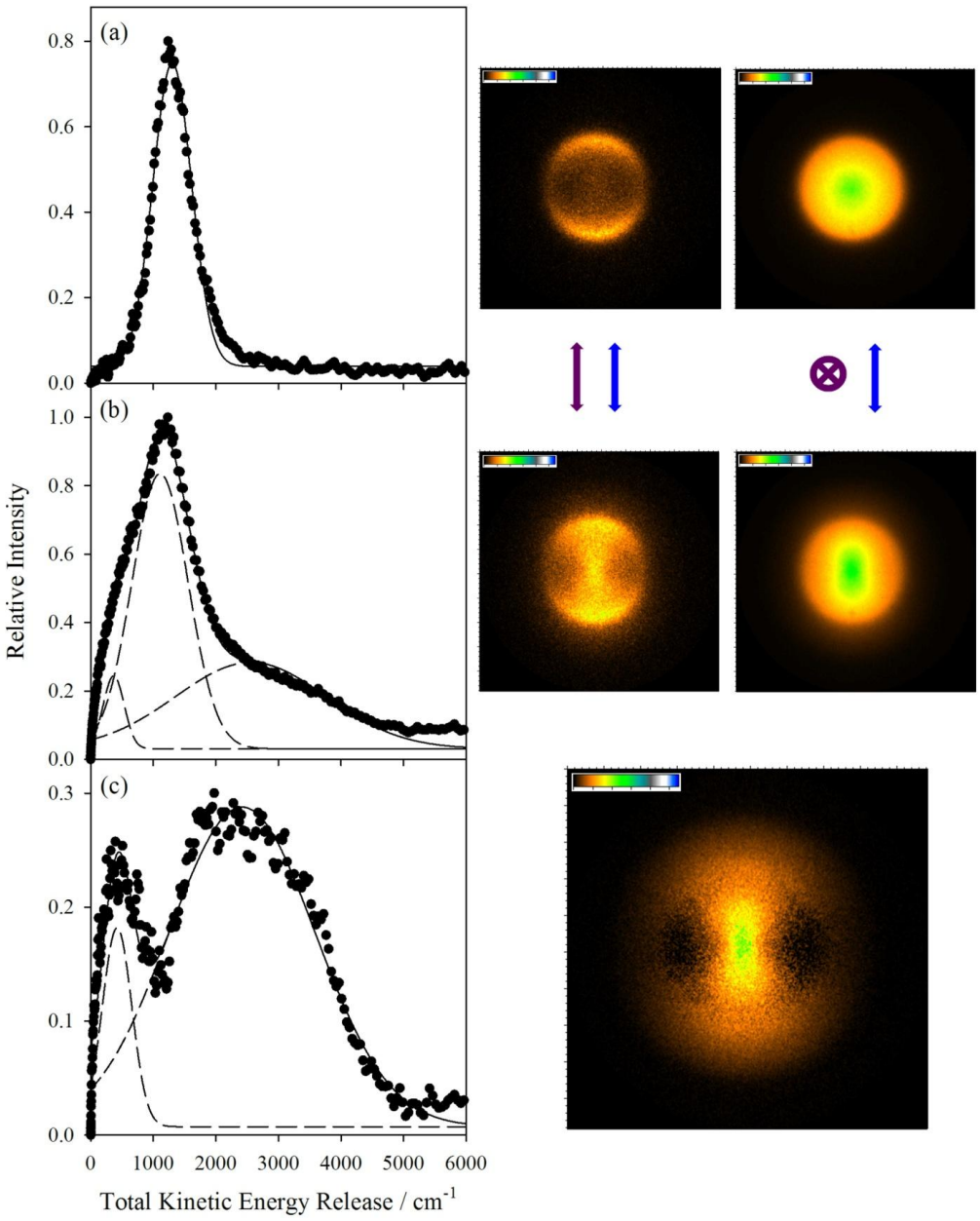
(a)
(b)
(c)
Relative Intensity
Total Kinetic Energy Release / cm-1

Figure 2. Raw images (right columns) and reconstructed total kinetic energy release profiles (left column) of I* ($^2P_{1/2}$) resulting from (a) 313 nm probe laser photodissociation and ionization, discussed in Appendix II, (b) the combination of 248 nm photodissociation and 313 nm probe laser photodissociation and ionization, and (c) the subtraction, indicating signal arising from 248 nm photodissociation followed by probe laser ionization. Gaussian functions are used to fit the data, shown as dashed lines. The polarizations of the probe and excimer lasers are illustrated with purple and blue arrows, respectively. Note that the raw images with the probe laser polarization parallel to plane of the detector were averaged for less than 10,000 shots, whereas the images with the probe laser polarization perpendicular to the plane of the detector were averaged for ~178,000 shots. The image in panel c is linearly scaled to approximately 1.5 times the size of the previous panels.

B. Angular Distribution

Another important aspect of the experimental results is the character of the electronic transition involved in the photodissociation process, which is reflected in the angular distribution derived from the image. The anisotropy of the I* image determined in the reconstruction can often be directly related to the properties of the excited electronic state involved in the photodissociation process. The lab frame angular distribution, $I(\theta)$, is defined as:

$$I(\theta) \propto 1 + \beta P_2(\cos(\theta))$$

where θ is the angle between the recoil direction and the polarization of the photolysis laser, P_2 is the second-order Legendre polynomial, and β is the anisotropy parameter. The anisotropy parameter, β, can range from -1 for a pure perpendicular transition to +2 for a pure parallel transition for the dissociation of a diatomic with the additional assumption of a rapid dissociation process compared to the rotational period of the molecule.[33]

Following 248 nm excitation, the angular distribution at the peak and nearby vicinity of the dominant high TKER feature shows a β parameter of +0.81(5), indicating that this feature arises from a prompt dissociation process. The electronic states accessed via 248 nm excitation have been proposed to be of B_2 and A_1 symmetry,[16] although recent theoretical work labels it as a single state of A_1 symmetry.[20] The molecular frame anisotropy formula, $\beta \approx 2P_2(\cos\chi)$, where χ is defined as the angle between the transition dipole moment and the fragment recoil velocity, can be used to predict the β parameter. The dipole moment for the CH_2I_2 $A_1 \leftarrow X$ A_1 transition would bisect the ICI

angle, which in the ground state is experimentally determined to be 114.7°,[34] resulting in a predicted β = -0.13. The dipole moment for CH_2I_2 $B_2 \leftarrow X$ A_1 transition is perpendicular to the ICI plane. This would result in a β parameter of -1. A mixing of these two states, no matter the relative composition, would give a negative β parameter and not the positive value obtained experimentally.

It is difficult to rationalize the observed β = +0.81(5) value based on simple models for the electronic states of CH_2I_2 at 248 nm. One scenario is an alternative assignment (other than A_1 or B_2) for the excited state in the Franck-Condon region, including the possibility of mixed electronic character. A transition to a state with B_1 character would yield a positive β parameter since the dipole moment for a $B_1 \leftarrow X$ A_1 transition lies parallel to the I-I direction,[15,16,19] resulting in a β = +1.13. In addition to the lower B_1 states, there is the possibility of another heretofore unidentified B_1 state contributing to the absorption at 248 nm, e.g. a higher state of unknown symmetry reported near 226 nm,[25] yet the simple exciton model originally used to assign the electronic absorption bands of CH_2I_2 does not predict another B_1 state in this vicinity. Another possible explanation is that the dissociation process accesses regions of nonadiabatic interaction and the resultant mixing of states with different electronic character could influence the observed β parameter. While the B_2 and/or A_1 states of interest both correlate to the CH_2I + I* products,[16,23] there are a significant number of electronic states, both singlet and triplet in character, coupled by spin-orbit interactions that could influence the dissociation dynamics.[20]

IV. Discussion

The total energy available, E_{avl}, to CH_2I + I* ($^2P_{1/2}$) fragments in channel (2) following photodissociation of CH_2I_2 at 248 nm can be expressed as

$$E_{avl} = h\nu - D_0 - E_{I^*} = E_T + E_{int}$$

where $h\nu$ is the photon energy, D_0 is the dissociation energy,[21] E_{I^*} is the I* ($^2P_{1/2}$) – I ($^2P_{3/2}$) energy,[35] E_T is the total translational energy of the fragments, or TKER, and E_{int} is the internal excitation of the CH_2I fragment. The dominant TKER feature in Figure 2c arising from photodissociation of CH_2I_2 at 248 nm via channel (2) has an average total translational energy $\langle E_T \rangle$=2100 cm^{-1}, corresponding to only 14% of the available energy (E_{avl} ~ 14800 cm^{-1}). The remaining 86% of the available energy is deposited into the nascent CH_2I photofragments with an average internal energy $\langle E_{int} \rangle$ = 12,700 cm^{-1} (36.3 kcal mol^{-1}). The distribution over translational energies also reveals the corresponding spread of internal energies for the CH_2I fragments.

The present findings are consistent with the prior IR emission from CH_2I fragments produced by channel (1) or (2).[21] The observation of significant IR emission over a broad range of wavelengths indicated extensive CH_2I internal excitation, with vibrational excitation nearing a quasicontinuum of states. The CH_2I internal energy (~85% of E_{avl}) estimated from IR emission arising from both I and I* channels can be compared with the present experimental result (~86% of E_{avl}) for channel (2) alone to demonstrate that the CH_2I fragments acquire similar percentages of the available energy in channels (1) and (2).

A simple impulsive model can be applied to CH_2I_2 dissociation to predict the fraction of available energy being channeled into product translation.[21,36] An instantaneous impulse coming from the C-I bond rupture causes translational energy to be imparted to products based on the reduced mass of the atoms directly involved with the dissociating bond (C-I) relative to the system as a whole. This simple model predicts that translational energy will account for 16% of the available energy, leaving the remaining 84% as CH_2I internal energy. This is quite similar to what is seen experimentally (86%). Moreover, as observed experimentally here and elsewhere,[19] this fraction does not change significantly over the photolysis wavelength from 313 nm to 248 nm, remaining close to 80-85%. This simple impulsive model seems to work well to describe the CH_2I_2 photodissociation dynamics for the many different excited electronic states accessed in this wavelength range as well as for both I and I* product channels (1) and (2).

Interestingly, the internal energy distribution of the CH_2I fragments is broader upon photolysis of CH_2I_2 at 248 nm than the narrow distribution observed upon photolysis at 313 nm (shown in Figure 2a and discussed in Appendix II) and the 277-305 nm wavelength region probed previously.[19] The TKER distribution and corresponding internal energy distribution of the CH_2I fragments resulting from 248 nm photolysis is almost four times as broad (*fwhm* ~ 2800 cm^{-1}) as that from 313 nm photolysis (*fwhm* ~700 cm^{-1}). A prior photodissociation study of CH_2I_2 at 266 nm showed a similarly broad distribution (*fwhm* ~ 3100 cm^{-1}), although this study did not distinguish between I and I* cofragments in channel (1) and (2).[17]

The photodissociation of CH_2I_2 at 248 nm is of renewed interest because it is being used in laboratory settings to generate the smallest Criegee intermediate, CH_2OO.[1-4] The subsequent reaction of CH_2I photofragments with O_2 generates CH_2OO + I in a near thermoneutral process.[5] The internal energy distribution of the CH_2I fragments determined in this work should enable future modeling of the internal excitation of the CH_2OO intermediates.

The CH_2I fragment is generated with an average internal energy of ~36 kcal mol^{-1} with an ~8 kcal mol^{-1} breadth (*fwhm*) in the CH_2I + I* channel (0.46 quantum yield).[22] Since a similar partitioning of available energy to CH_2I fragments is evident in the I* channel (this work) and combined I/I* channels (prior work),[21] one can infer that the CH_2I + I channel will have the same partitioning. As a result, the average internal energy of the CH_2I fragments in the I channel is expected to be close to ~54 kcal mol^{-1}, likely with a similar breadth. [A small fraction of the CH_2I fragments may even have enough internal energy to dissociate into CH_2 + I (ΔH_{rxn} = 62.6 kcal mol^{-1})[21], which would no longer be relevant to the formation of CH_2OO via the $CH_2I + O_2$ reaction.] This bimodal distribution of internally 'hot' CH_2I fragments is expected to give rise to highly excited CH_2OO intermediates.

Moreover, the degree of CH_2OO internal excitation produced in the new laboratory scheme with 248 nm photolysis of CH_2I_2, in particular channel (1), is comparable to that acquired in alkene-ozone reactions in the atmosphere, which are highly exothermic reactions with up to 60 kcal mol^{-1} released to products.[9] This suggests that the CH_2OO intermediates generated via the alternative laboratory scheme at

248 nm may undergo unimolecular and bimolecular processes similar to those observed upon ozonlysis of alkenes. Notably, there should be adequate internal excitation of the Criegee intermediate to isomerization to dioxirane (barrier height of 19.2 kcal mol^{-1}),[37] and release OH radicals.[4,8,9]

The simplest Criegee intermediate has also been generated using 351 nm photolysis of CH_2I_2.[38] CH_2I_2 has an order of magnitude smaller absorption cross section at 351 nm than 248 nm,[39] which in principle can be overcome by the high photon flux of excimer lasers. The internal energy distribution of the CH_2OO intermediate is also expected to be much lower, since the CH_2I fragments will have substantially less internal excitation. The fraction of available energy channeled into CH_2I internal energy is similar at 351 nm and 248 nm, but the amount of CH_2I internal excitation is substantially different. Since only the $CH_2I + I$ product channel is open,[22] CH_2I fragments will be generated with ~25 kcal mol^{-1} of internal energy, assuming 85% partitioning of the available energy. This is significantly less than the CH_2I internal excitation from 248 nm photodissociation via channels (1) and (2). The lower internal excitation of CH_2I and correspondingly lower internal energy of CH_2OO should make it easier to collisionally stabilize the Criegee intermediates for subsequent study.

V. Conclusion

The photodissociation dynamics of CH_2I_2 at 248 nm is examined using velocity map imaging with detection of the $I^*(^2P_{1/2})$ product by 2+1 REMPI at 313 nm. The polarization of the 313 nm probe laser is oriented perpendicular to that of photolysis laser

and the plane of the detector as a means to improve subtraction of the one-color I* signal from 313 nm photolysis/ionization alone. The resultant image arising from 248 nm photolysis is reconstructed to obtain the velocity and angular distributions of the I* products as well as the corresponding kinetic energy release to products and anisotropy parameter. The dominant feature in the TKER distribution has a sizable breadth and $\langle E_T \rangle$ = 2100 cm^{-1}, which corresponds to only 14% of the available energy. This leaves the remaining 86% channeled into the internal excitation of the CH_2I cofragment, where $\langle E_{int} \rangle$ = 12,700 cm^{-1} (36.3 kcal mol^{-1}). This is in accord with a previous investigation of IR emission from CH_2I fragments originating from a combination of the I and I* channels.[21] The dominant TKER feature has a positive anisotropy parameter of β = +0.81(5) derived from the image reconstruction. This is not consistent, however, with the electronic character (A_1 and/or B_2) previously predicted for 248 nm excitation of CH_2I_2 (β = -0.13 or -1 for A_1 or B_2 transitions, respectively). The positive β value suggests mixing of electronic states in the Franck-Condon region and/or in the dissociation dynamics. A more in depth theoretical treatment, similar to what has been done recently at lower energies,[20] would be necessary to understand the dissociation dynamics at this high energy. Photodissociation of CH_2I_2 at 248 nm is of renewed interest because reaction of the CH_2I fragments with O_2 is being used to produce the simplest Criegee intermediate CH_2OO in the laboratory. Assuming that the high degree of internal excitation of the CH_2I fragment is carried over into CH_2OO, the internal energy of the Criegee intermediate produced in the laboratory likely mimics that from alkene ozonolysis in the atmosphere.

Acknowledgements

This research was principally supported by the U.S. Department of Energy, Basic Energy Sciences (DE-FG02-87ER13792). The authors thank Joseph M. Beames for helpful discussions.

References

[1] O. Welz, J.D. Savee, D.L. Osborn, S.S. Vasu, C.J. Percival, D.E. Shallcross, C.A. Taatjes, Science 335 (2012) 204.
[2] C.A. Taatjes, O. Welz, A.J. Eskola, J.D. Savee, D.L. Osborn, E.P.F. Lee, J.M. Dyke, D.W.K. Mok, D.E. Shallcross, C.J. Percival, Phys. Chem. Chem. Phys. 14 (2012) 10391.
[3] J.M. Beames, F. Liu, L. Lu, M.I. Lester, J. Am. Chem. Soc. 134 (2012) 20045.
[4] J.M. Beames, F. Liu, L. Lu, M.I. Lester, J. Chem. Phys. 138 (2013) 244307.
[5] E.P.F. Lee, D.K.W. Mok, D.E. Shallcross, C.J. Percival, D.L. Osborn, C.A. Taatjes, J.M. Dyke, Chem.-Eur. J. 18 (2012) 12411.
[6] J.G. Calvert, R. Atkinson, J.A. Kerr, S. Madronich, G.K. Moortgat, T.J. Wallington, G. Yarwood: The Mechanisms of Atmospheric Oxidation of the Alkenes Oxford University Press, Oxford, 2000.
[7] R. Criegee, Angew. Chem. Int. Edit. 14 (1975) 745.
[8] O. Horie, G.K. Moortgat, Acc. Chem. Res. 31 (1998) 387.
[9] D. Johnson, G. Marston, Chem. Soc. Rev. 37 (2008) 699.
[10] W.M. Kwok, D.L. Phillips, J. Chem. Phys. 104 (1996) 2529.
[11] R. Vogt, R. Sander, R. Von Glasow, P.J. Crutzen, J. Atmos. Chem. 32 (1999) 375.
[12] S.J. Riley, K.R. Wilson, Faraday Discuss. 53 (1972) 132.
[13] T. Donohue, J.R. Wiesenfeld, J. Chem. Phys. 63 (1975) 3130.
[14] M. Ito, P.C. Huang, E.M. Kosower, Transactions of the Faraday Society 57 (1961) 1662.
[15] K.W. Jung, T.S. Ahmadi, M.A. El-Sayed, Bull. Korean Chem. Soc. 18 (1997) 1274.
[16] M. Kawasaki, S.J. Lee, R. Bersohn, J. Chem. Phys. 63 (1975) 809.
[17] P.M. Kroger, P.C. Demou, S.J. Riley, J. Chem. Phys. 65 (1976) 1823.
[18] G. Schmitt, F.J. Comes, J. Photochem. 14 (1980) 107.
[19] H.F. Xu, Y. Guo, S.L. Liu, X.X. Ma, D.X. Dai, G.H. Sha, J. Chem. Phys. 117 (2002) 5722.
[20] Y.J. Liu, L. De Vico, R. Lindh, W.H. Fang, Phys. Chem. Chem. Phys. 8 (2007) 890.
[21] S.L. Baughcum, S.R. Leone, J. Chem. Phys. 72 (1980) 6531.
[22] J.B. Koffend, S.R. Leone, Chem. Phys. Lett. 81 (1981) 136.

[23] T.F. Hunter, K.S. Kristjansson, Chem. Phys. Lett. 90 (1982) 35.
[24] S.Y. Chen, P.Y. Tsai, H.C. Lin, C.C. Wu, K.C. Lin, B.J. Sun, A.H.H. Chang, J. Chem. Phys. 134 (2011).
[25] A. Gedanken, M.B. Robin, Y. Yafet, J. Chem. Phys. 76 (1982) 4798.
[26] Y.J. Jung, Y.S. Kim, W.K. Kang, K.H. Jung, J. Chem. Phys. 107 (1997) 7187.
[27] Other delays were also tested, but I+ ions generated directly from the 248 nm photolysis laser interfered at shorter times. Iodine atoms did not move out of the interaction region during this time delay, as corroborated by the single laser experiment utilizing an iodine REMPI scheme near 248 nm.
[28] D. Townsend, M.P. Minitti, A.G. Suits, Rev. Sci. Instrum. 74 (2003) 2530.
[29] A.T.J.B. Eppink, D.H. Parker, Rev. Sci. Instrum. 68 (1997) 3477.
[30] P.C. Samartzis, D.J. Smith, T.P. Rakitzis, T.N. Kitsopoulos, Chem. Phys. Lett. 324 (2000) 337.
[31] G.A. Garcia, L. Nahon, I. Powis, Rev. Sci. Instrum. 75 (2004) 4989.
[32] For a few one-laser experiments, the UV probe laser was set near 248 nm utilizing a weaker 2+1 REMPI transition [C.J. Hu, S.X. Pei, Y.L. Chen, K.P. Liu, J. Phys. Chem. 111 (2007) 6813)] to ionize I* (2P1/2) atoms following photodissociation with the same laser. This scheme was used to validate the general trend of the kinetic energy release from the subtracted image as well as the strongly positive β parameter. Although the signal is weaker due to the less intense REMPI transition, the image and kinetic energy release profile resulting from reconstruction (not shown) are quite similar to the dominant, higher TKER portion of the subtracted image from the two-color experiment shown in Figure 2c.
[33] B.J. Whitaker: Imaging in Molecular Dynamics Technology and Applications, Cambridge University Press, 2003.
[34] S.A. Kudchadker, A.P. Kudchadker, J. Chem. Ref. Data 4 (1975) 457.
[35] JANAF Thermochemical Tables, National Bureau of Standards, Washington, D.C., 1971.
[36] G.E. Busch, K.R. Wilson, J. Chem. Phys. 56 (1972) 3626.
[37] R. Gutbrod, E. Kraka, R.N. Schindler, D. Cremer, J. Am. Chem. Soc. 119 (1997) 7330.
[38] C.A. Taatjes, O. Welz, A.J. Eskola, J.D. Savee, A.M. Scheer, D.E. Shallcross, B. Rotavera, E.P.F. Lee, J.M. Dyke, D.K.W. Mok, D.L. Osborn, C.J. Percival, Science 340 (2013) 177.
[39] IUPAC, Summary of evaluated kinetic and photochemical data for atmospheric chemistry, 2004.

CHAPTER 7
UV Photodissociation Dynamics of CH_2OO

The experimental research presented in this chapter was performed at the University of Pennsylvania. This research is being prepared for publication as a communication in the *Journal of Chemical Physics*.

Reference: J. H. Lehman, H. Li, J. M. Beames, M. I. Lester, *J. Chem. Phys.*, manuscript in preparation (2013).

Alkenes are an important tropospheric constituent, originating from biogenic and anthropogenic sources. A major atmospheric removal process for alkenes is ozonolysis.[1,2] This is a highly exothermic process that produces a primary ozonide with a cyclic structure, which dissociates to form a carbonyl oxide, known as the Criegee intermediate, and an aldehyde (or ketone).[1,3,4] The Criegee intermediates are generated with a large amount of internal excitation, which can lead to unimolecular decomposition or rearrangement, forming products such as OH, HO_2, CO, CO_2, CH_3, and H_2CO.[2,4] The Criegee intermediate can also be collisionally stabilized and/or react with tropospheric species including H_2O, NO_2 and SO_2.[5-7] The rates for these bimolecular reactions are more rapid and conformer-specific than previously thought, which may substantially change predictions of their tropospheric chemistry.[8]

Recent experiments in this laboratory have revealed an additional atmospheric decay pathway for the simplest Criegee intermediate CH_2OO and other alkyl substituted carbonyl oxides, namely solar photolysis in the UVA region.[9,10] For CH_2OO, Beames *et al.* obtained the $B\ ^1A' \leftarrow X\ ^1A'$ absorption spectrum in the UVA region by measuring the UV-induced depletion of the ground state population and corresponding VUV photoionization signal at m/z=46. The CH_2OO *B*-*X* spectrum peaks at ~335 nm with a breadth of ~40 nm (*fwhm*) and a large absorption cross section of ~5 x 10^{-17} cm^2 $molecule^{-1}$. Theoretical calculations indicate that this is a $\pi^* \leftarrow \pi$ transition primarily involving 4π e^- localized on the carbonyl oxide group in the Franck-Condon region.[11] A very large depletion approaching 100% near the peak of the profile is indicative of rapid dynamics in the excited $B\ ^1A'$ electronic state and consistent with the repulsive *B*-state

potential along the O-O coordinate computed theoretically.[9,10,12] The UV absorption spectrum was combined with the solar actinic flux to estimate an atmospheric lifetime for CH_2OO at midday on the order of ~1 s with respect to solar photolysis.

In this Communication, we significantly extend the previous study of the UV *B* $^1A' \leftarrow X\ ^1A'$ absorption spectrum for the simplest Criegee intermediate CH_2OO by probing the resultant dissociation dynamics using velocity map imaging (VMI). Specifically, we obtain the kinetic energy and angular distributions of the O ^1D products from direct dissociation of CH_2OO *B* $^1A'$ to O ^1D + H_2CO *X* $^1A_1$ products. The ground *X* $^1A'$ state of CH_2OO also correlates with this same asymptotic limit. (The lower energy O ^3P + H_2CO *X* $^1A_1$ product channel is spin-forbidden.) Notably, the translational energy release is used to infer an upper limit for the ground state binding energy (D_0) of CH_2OO *X* $^1A_1$, which is then compared with the wide range of theoretical predictions for this important thermodynamic property.[12-15]

Only recently have the CH_2OO and CH_3CHOO Criegee intermediates been observed directly in the gas phase utilizing VUV photoionization near threshold to provide isomer- and mass-selective detection;[5,7,16] prior studies have relied on indirect methods for detection.[17] These recent studies also introduced a new photosynthetic route for generating the Criegee intermediates from diiodo alkane precursors.[5,7] The simplest Criegee intermediate CH_2OO is generated in this laboratory in a similar manner.[9,10] Specifically, a gas mixture of CH_2I_2 entrained in a 10% O_2/Ar (15 psi) is irradiated along the length of a quartz capillary tube reactor using the 248 nm output from an excimer

laser, initiating the photolysis of CH_2I_2 and subsequent reaction of CH_2I with O_2 to form CH_2OO.

The Criegee intermediates are collisionally stabilized in the capillary tube, cooled in a supersonic expansion, and then travel ~4 cm downstream into the interaction region of a VMI apparatus. The frequency-doubled output of a Nd:YAG pumped dye laser utilizing many dyes (~0.5 mJ, ~0.3 cm^2, 7 ns) crosses the interaction region and excites CH_2OO on the *B*-*X* transition in the 300-365 nm range (pump laser). After a short time delay (30 ns), the O ^{1}D dissociation products are ionized via 2+1 resonance enhanced multiphoton ionization (REMPI) at 205.47 nm,[18] which is generated by frequency-tripling the output of another Nd:YAG pumped dye laser (probe laser). This laser is scanned over the O-atom Doppler profile during image collection. The probe laser is focused into the center of the interaction region (50 cm focal length lens) and spatially overlapped with the unfocused UV pump laser. Ions travel through a field free time-of-flight (TOF) region and are velocity focused onto a spatially sensitive MCP/phosphor screen coupled detector, which is gated for the O^+ mass (m/z = 16). The pump and probe laser polarizations are both set parallel to the plane of the detector. The VMI apparatus design and calibration are discussed in detail elsewhere.[19] TOF profiles along with the spatial images captured by a CCD camera, such as the example shown in Figure 1, are transferred to a laboratory computer for further analysis. Image reconstruction is performed using the BASEX program.[20] The resultant radial distribution is then transformed to give the velocity distribution of the O ^{1}D fragments.

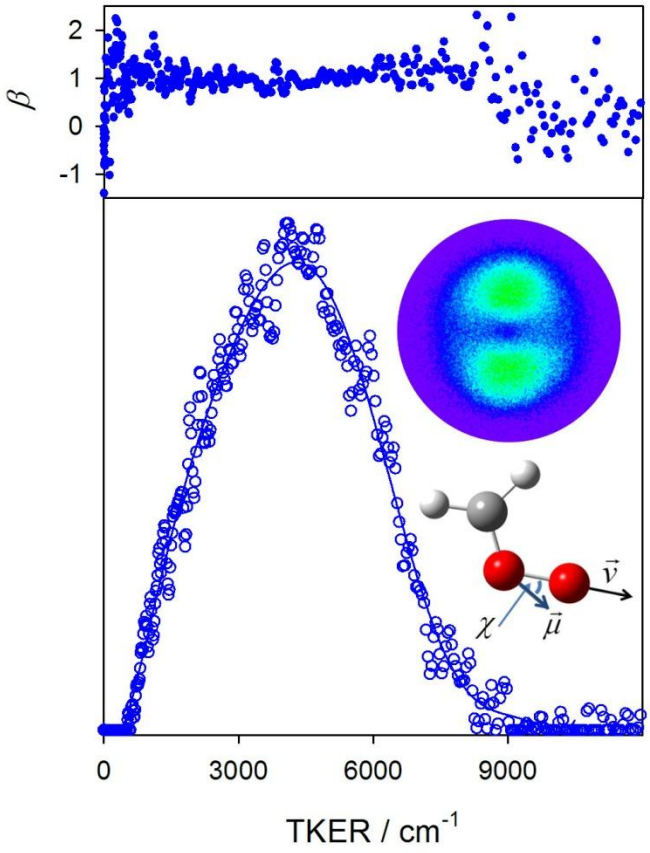

Figure 1. Velocity mapped raw image with derived total kinetic energy release (TKER) and anisotropy parameter (β) distributions for O ^{1}D products resulting from photolysis of the simplest Criegee intermediate CH_2OO at 360 nm. The polarizations of the pump and probe lasers are vertical in the plane of the detector. The TKER distribution is fit to a polynomial expansion as a guide to the eye with baseline at zero. The anisotropic angular distribution in the raw image and associated β parameter arise from the interaction of the transition dipole moment (TDM, $\vec{\mu}$) with the pump laser polarization. In the molecular frame, the angle χ between the TDM of CH_2OO and the recoil velocity ($\vec{v}$) of the O-atom fragment is evaluated from the anisotropy parameter.

Table 1. Characteristics of the total kinetic energy (TKER) and anisotropic angular distributions derived from reconstructed images of O ^{1}D products following photolysis of CH_2OO at 308, 330, and 360 nm. The peak and *fwhm* of the TKER distributions are obtained from a Gaussian fit. The anisotropy parameter β is defined in the main text.

	308 nm	330 nm	360 nm
Peak / cm^{-1}	6,300	5,400	4,000
fwhm / cm^{-1}	6,800	5,500	4,400
β	0.98(2)	0.99(2)	0.97(3)

Following excimer photolysis, a large pump laser induced O^+ signal is detected with resonant probe laser ionization. No O^+ signal is seen when the probe laser is tuned off-resonance of the REMPI transition, demonstrating that the O^+ signal arises exclusively from ionization of O ^{1}D. In addition, a much smaller O^+ signal is observed with the excimer and 2+1 REMPI probe lasers only; no signal is detected with the probe laser alone. Using velocity information from the image, this small signal is attributed to photodissociation of IO at 205.47 nm, producing I* ($^2P_{1/2}$) + O ^{1}D, which is subsequently ionized by the same laser.[21] In order to remove this small excimer + probe signal, an active background subtraction scheme was implemented for TOF and image data collection. This is achieved by operating the pump laser (5 Hz) at half the repetition of the other lasers (10 Hz).

Initially, the pump laser is stepped across a broad UV spectral range while monitoring the O^+ signal arising from O ^{1}D REMPI, yielding the UV action spectrum shown in the leftmost panel of Figure 2. The UV action spectrum with peak at ~331 nm and breadth of ~40 nm (*fwhm*) reproduces the UV absorption spectrum for CH_2OO reported previously within experimental uncertainty.[9] This close correlation indicates that the species generating O ^{1}D is indeed CH_2OO. The experimental uncertainties, derived from repeated measurements (error bars) and Gaussian fits, for the UV action and absorption spectra of CH_2OO are sufficiently large to preclude determination of small changes in the O ^{1}D quantum yield. The absolute O ^{1}D quantum yield is not determined in this work. We note that there is another energetically accessible product asymptote, O

$^3P + H_2CO$ *a* $^3A''$, shown in Figure 2, but no information is currently available on the branching to this product channel.

The VMI images collected (and reconstructed) following UV excitation of CH_2OO at several wavelengths (308, 330, and 360 nm) provide a wealth of new information on the velocity distribution and anisotropic angular distribution of the O ^1D photofragments. The total kinetic energy released (TKER) to the O $^1D + H_2CO$ *X* $^1A_1$ products in the photodissociation process is obtained through conservation of momentum based on the velocity distribution of the O ^1D fragments. A representative image and corresponding TKER distribution resulting from 360 nm photolysis (pump laser) is shown in Figure 1. The TKER distribution peaks at ~4000 cm^{-1}, falling off to higher and lower energy, but is otherwise unstructured over its 9000 cm^{-1} span. Analogous TKER distributions are obtained following 308 and 330 nm photolysis of CH_2OO with their properties listed in Table 1.

The VMI image of the O ^1D fragments also exhibits an anisotropic angular distribution, I(θ), indicative of prompt dissociation of CH_2OO. I(θ) can be recast in terms of an anisotropy or β parameter $I(\theta) \propto 1 + \beta P_2(\cos\theta)$, where P_2 is a second-order Legendre polynomial and θ is the angle between the recoil direction and the polarization of the UV photolysis laser.[22] At 360 nm, a β parameter of 0.97(3) is obtained for O ^1D fragments with kinetic energies near the peak of the TKER distribution. Analogous angular distributions are seen upon photolysis of CH_2OO at 308 and 330 nm with the same value for β (Table 1). In the molecular frame, the β parameter is related to the

angle χ between the transition dipole moment (TDM, $\vec{\mu}$) and the velocity recoil $\vec{v}$ vectors via $\beta = 2\langle P_2(\vec{\mu}\cdot\vec{v})\rangle = 2\langle P_2(\cos\chi)\rangle$.[22] The experimentally derived β parameters yield an average χ of 35.7(2)°, thereby determining the angle between the TDM and the O ^{1}D recoil along the original O-O bond axis as shown in Figure 1.

Complementary electronic structure calculations[10] at the EOM-CCSD/6-311++G(2d,2p) level of theory are used to evaluate the TDM for the *B*-*X* transition of CH_2OO in the Franck-Condon region. The angle between the TDM and O-O bond is evaluated to be 30° and oriented as shown in Figure 1. The theoretically derived angle is in good agreement with that determined experimentally, demonstrating that the angular distribution of the O ^{1}D products is a reflection of the $\pi^* \leftarrow \pi$ transition originating from the 4π e^- system of the COO group in the CH_2OO intermediate. Early GVB calculations by Wadt and Goddard also placed the TDM at 30° from the O-O bond.[23]

Using conservation of energy, $E_{avl} = E_{h\nu} - D_0 = TKER + E_{int}(H_2CO)$, the TKER distribution can be directly related to the internal energy distribution of the formaldehyde cofragment $E_{int}(H_2CO)$ using the photon energy $E_{h\nu}$ and dissociation energy D_0 to O ^{1}D + H_2CO X $^1A_1$ products or corresponding available energy E_{avl}. (The internal energy of the jet-cooled Criegee intermediate is assumed to be small and is neglected.) However, the dissociation energy for CH_2OO or other Criegee intermediates has not been established in any prior experimental study and varies greatly among theoretical predictions as discussed below.[12-15] Nevertheless, plotting the TKER distributions arising from photodissociation of CH_2OO at 308, 330, and 360 nm as $E_{h\nu} - TKER$ in Figure 2

shows the similar profiles of the distributions starting at $E_{h\nu}$ and terminating at a common energy of ~54 kcal mol^{-1}. The lowest translational energies at $E_{h\nu}$ correspond to the highest internal energies for H_2CO; similarly, the highest translational energies at $E_{h\nu} - \mathrm{TKER}$ = 54 kcal mol^{-1} indicate the lowest internal (vibrational + rotational) energy for H_2CO. Since the lowest internal energy of the H_2CO fragment is its zero-point level, the 54 kcal mol^{-1} cutoff of the TKER distributions represents a rigorous upper limit for the CH_2OO $X\ ^1A'$ binding energy relative to O ^1D + H_2CO $X\ ^1A_1$ products.

The rotational energy of the nascent H_2CO fragments can be separately estimated using an impulsive model, which assumes prompt dissociation, as seen experimentally, on the repulsive *B*-state potential in the Franck-Condon region. Specifically, a model developed by Butler and coworkers equates the rotational angular momentum imparted to formaldehyde as a result of impulsive O-O bond breakage with the orbital angular momentum arising from the recoiling O ^1D atom product.[24] The rotational energy of the H_2CO fragments can then be related to the experimentally derived recoil kinetic energy using $E_{rot} = \frac{\mu b^2}{I_C} E_T$, where μ is the reduced mass of the H_2CO + O system, b is the impact parameter, I_C is the moment of inertia about the C inertial axis of the H_2CO subunit, and E_T is the total kinetic energy release (TKER). The factor $\mu b^2 / I_C$ is evaluated to be 0.20 based on the equilibrium geometry for CH_2OO.[25] This factor changes only slightly if the equilibrium geometry for the separated H_2CO product is utilized,[26] although the geometries differ as detailed below. Using this model, the rotational energy of the H_2CO product is estimated to be ~5 kcal mol^{-1} at the maximum

TKER following 360 nm photolysis of CH_2OO, and even greater rotational energies (up to 8 kcal mol^{-1}) can result from 330 and 308 nm photolysis. It should be noted that zero-point vibrational motion of CH_2OO, particularly the COO bend, will result in a range of impact factors and corresponding small changes (~1 kcal mol^{-1}) in the predicted rotational energies of the H_2CO fragments. Using the estimated rotational energy for the H_2CO product reduces the CH_2OO binding energy to $D_0 \leq 47$ kcal mol^{-1}.

The broad span of the TKER distributions is indicative of a high degree of vibrational excitation in the H_2CO products. Vibrational excitation extending over 9000 to 13,500 cm^{-1} is evident following photolysis of CH_2OO, corresponding to ~80% of E_{avl}. This substantial vibrational excitation likely originates from changes in the equilibrium structure for CH_2OO as compared to H_2CO. In particular, the HCH angle decreases by close to 10° and the C-O bond length decreases by ~0.07 Å upon dissociation, suggesting multiple quanta of CO stretch, HCH rock, and/or HCH bend excitation in the H_2CO products. The TKER distribution lacks structure because of the substantial vibrational and/or rotational excitation of the H_2CO fragments.

There are several theoretical predictions of the CH_2OO $X\ ^1A' \rightarrow O\ ^1D + H_2CO$ $X\ ^1A_1$ dissociation energy (D_e) or the bond dissociation energy (BDE) for the spin-forbidden channel of CH_2OO $X\ ^1A'$ to ground state $O\ ^3P + H_2CO$ $X\ ^1A_1$ products. The latter value differs by the energy difference between the ground (^3P) and excited (^1D) states of atomic oxygen (45.5 kcal mol^{-1}) as shown in Figure 1. Using CCSD(T)/CBS, Nguyen *et al.* reported a BDE for CH_2OO of 5.8 kcal mol^{-1},[15] corresponding to D_e = 51.3 kcal mol^{-1}. Alpincourt *et al.* considered the dissociation of CH_2OO $X\ ^1A'$ along the O-O

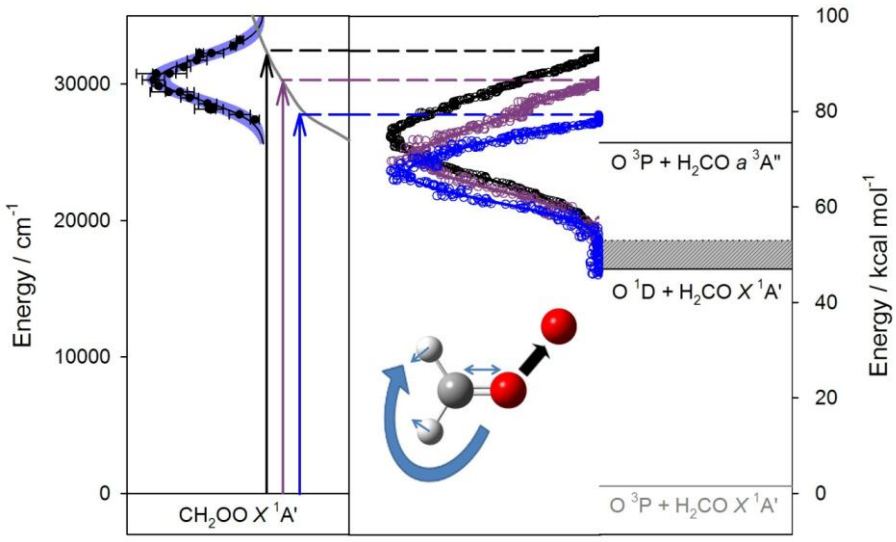

Figure 2. Left panel: CH_2OO action spectrum is obtained by detecting O ^{1}D products following UV excitation in the 300-365 nm range. The smooth curve is a fit to a Gaussian function with baseline at zero; the uncertainty is illustrated by the shaded area. A schematic repulsive potential for the CH_2OO *B*-state in the Franck-Condon region is illustrated with arrows indicating the excitation wavelengths used for image analysis. Right panel: Total kinetic energy release (TKER) distributions for O ^{1}D + H_2CO X ^{1}A′ products arising from photodissociation of CH_2OO at 308 nm (black), 330 nm (purple), and 360 nm (blue) are plotted relative to the photon energy, $E_{h\nu}$. The common termination of the distributions at 54 kcal mol^{-1} corresponds to an upper limit for the CH_2OO X ^{1}A′ dissociation energy. The gray shaded area represents the rotational energy of the H_2CO product estimated using an impulsive model, which reduces the upper limit for the dissociation energy of CH_2OO X ^{1}A′ to O ^{1}D + H_2CO X ^{1}A′ products to $D_0 \leq 47$ kcal mol^{-1}. The other asymptotic limits are positioned accordingly. The rotational and vibrational excitation of the separating H_2CO product is shown schematically.

coordinate with CASPT2/ANO1, although a specific value for D_e was not reported.[12] Another study by Anglada and coworkers[14] using MRDCI+Q (with an augmented Huzinaga-Dunning double-ζ basis set) computed a CH_2OO $X\ ^1A'$ dissociation energy of D_e ~34 kcal mol^{-1}. Earlier work by Cremer *et al.* using CCSD(T)/TZ+2P predicted D_e to be 47.0 kcal mol^{-1}.[13] Additional high level multi-reference *ab initio* calculations are underway in this group. In order to compare the theoretical predictions for D_e with the experimental value for the stabilization of CH_2OO $X\ ^1A'$, one must take into account the reduction in zero-point energy upon dissociation. This change is estimated using the anharmonic frequencies computed by Su *et al.* for CH_2OO[27] and the experimental frequencies for H_2CO,[28] giving 2.5 kcal mol^{-1}. Thus, the theoretical predictions need to be reduced by 2.5 kcal mol^{-1} to compare with experiment, indicating very good agreement with Nguyen *et al.*[15]

The best estimate for the stability of CH_2OO $X\ ^1A'$ relative to the $O\ ^1D + H_2CO$ $X\ ^1A_1$ asymptotic limit, $D_0 \leq 47$ kcal mol^{-1}, is greater than the bond energy of a typical O-O single bond, reflecting the biradical and/or zwitterionic character of the COO group. Similarly, the O-O bond length of CH_2OO, recently determined by Fourier transform microwave spectroscopy, r_{OO} = 1.345 Å,[25] is shorter than a typical O-O single bond. One should note that isomerization of CH_2OO to dioxirane is predicted to have a lower barrier of 19.2 kcal mol^{-1} using CCSD(T)/6-31G(d,p),[29] indicating that isomerization and subsequent decomposition to OH radicals and other products[2,4] will be favored over O-O bond breakage for energized CH_2OO intermediates.

The UVA photolysis of CH_2OO intermediates has potentially significant atmospheric implications since the O ^{1}D products will react at a gas kinetic rate with H_2O in the troposphere to generate secondary OH radicals.[30] Under atmospheric conditions, Criegee intermediates formed by alkene ozonolysis will be rapidly photolyzed by solar radiation in the UVA region[9,10] to generate O ^{1}D and secondary OH radicals. This mechanism is quite similar to the primary scheme for OH production in the troposphere, in which O ^{1}D is generated from O_3 photolysis with UVB solar radiation,[30] differing mainly in the requirement of an alkene-rich environment.

References

1 J. G. Calvert, R. Atkinson, J. A. Kerr, S. Madronich, G. K. Moortgat, T. J. Wallington, and G. Yarwood, *The Mechanisms of Atmospheric Oxidation of the Alkenes* (Oxford University Press, Oxford, 2000).

2 D. Johnson and G. Marston, Chem. Soc. Rev. **37**, 699 (2008).

3 R. Criegee, Angew. Chem. Int. Edit. **14**, 745 (1975).

4 O. Horie and G. K. Moortgat, Acc. Chem. Res. **31**, 387 (1998).

5 O. Welz, J. D. Savee, D. L. Osborn, S. S. Vasu, C. J. Percival, D. E. Shallcross, and C. A. Taatjes, Science **335**, 204 (2012).

6 C. A. Taatjes, O. Welz, A. J. Eskola, J. D. Savee, D. L. Osborn, E. P. F. Lee, J. M. Dyke, D. W. K. Mok, D. E. Shallcross, and C. J. Percival, Phys. Chem. Chem. Phys. **14**, 10391 (2012).

7 C. A. Taatjes, O. Welz, A. J. Eskola, J. D. Savee, A. M. Scheer, D. E. Shallcross, B. Rotavera, E. P. F. Lee, J. M. Dyke, D. K. W. Mok, D. L. Osborn, and C. J. Percival, Science **340**, 177 (2013).

8 L. Vereecken, H. Harder, and A. Novelli, Phys. Chem. Chem. Phys. **14**, 14682 (2012).

9 J. M. Beames, F. Liu, L. Lu, and M. I. Lester, J. Am. Chem. Soc. **134**, 20045 (2012).

10 J. M. Beames, F. Liu, L. Lu, and M. I. Lester, J. Chem. Phys. **138**, 244307 (2013).

11 J. M. Anglada, J. Gonzalez, and M. Torrent-Sucarrat, Phys. Chem. Chem. Phys. **13**, 13034 (2011).

12 P. Aplincourt, E. Henon, F. Bohr, and M. F. Ruiz-Lopez, Chem. Phys. **285**, 221 (2002).

[13] D. Cremer, J. Gauss, E. Kraka, J. F. Stanton, and R. J. Bartlett, Chem. Phys. Lett. **209**, 547 (1993).

[14] J. M. Anglada, J. M. Bofill, S. Olivella, and A. Solé, J. Am. Chem. Soc. **118**, 4636 (1996).

[15] M. T. Nguyen, T. L. Nguyen, V. T. Ngan, and H. M. T. Nguyen, Chem. Phys. Lett. **448**, 188 (2007).

[16] C. A. Taatjes, G. Meloni, T. M. Selby, A. J. Trevitt, D. L. Osborn, C. J. Percival, and D. E. Shallcross, J. Am. Chem. Soc. **130**, 11883 (2008).

[17] N. M. Donahue, G. T. Drozd, S. A. Epstein, A. A. Presto, and J. H. Kroll, Phys. Chem. Chem. Phys. **13**, 10848 (2011).

[18] S. T. Pratt, P. M. Dehmer, and J. L. Dehmer, Phys. Rev. A **43**, 4702 (1991).

[19] J. H. Lehman, H. Li, and M. I. Lester, manuscript in preparation (2013).

[20] V. Dribinski, A. Ossadtchi, V. A. Mandelshtam, and H. Reisler, Rev. Sci. Instrum. **73**, 2634 (2002).

[21] K. S. Dooley, J. N. Geidosch, and S. W. North, Chem. Phys. Lett. **457**, 303 (2008).

[22] B. J. Whitaker, Imaging in Molecular Dynamics Technology and Applications. (Cambridge University Press, 2003).

[23] W. R. Wadt and W. A. Goddard, J. Am. Chem. Soc. **97**, 3004 (1975).

[24] B. J. Ratliff, C. C. Womack, X. N. Tang, W. M. Landau, L. J. Butler, and D. E. Szpunar, J. Phys. Chem. A **114**, 4934 (2010).

[25] M. Nakajima and Y. Endo, J. Chem. Phys., submitted (2013).

[26] L. V. Gurvich, Pure Appl. Chem. **61**, 1027 (1989).

[27] Y.-T. Su, Y.-H. Huang, H. A. Witek, and Y.-P. Lee, Science **340**, 174 (2013).

[28] T. Nakanaga, S. Kondo, and S. Saeki, J. Chem. Phys. **76**, 3860 (1982).

[29] R. Gutbrod, E. Kraka, R. N. Schindler, and D. Cremer, J. Am. Chem. Soc. **119**, 7330 (1997).

[30] Y. Matsumi and M. Kawasaki, Chem. Rev. **103**, 4767 (2003).

APPENDIX I
Doppler Profile Analysis Procedure

The experimental research presented in this chapter was performed at the University of Pennsylvania. This appendix was published as online supplementary material in the *Journal of Chemical Physics* in conjunction with Chapter 3 of this thesis.

Reference: J. H. Lehman, J. L. Bertrand, T. A. Stephenson, M. I. Lester, *J. Chem. Phys.*, **135**, 144303 (2011).

I. Analysis Procedure

A Doppler profile is a one dimensional projection of a three dimensional distribution of velocities along the laser propagation axis. Only hydrogen atoms with zero velocity component along the laser propagation axis will absorb precisely at the two-photon transition frequency, υ_0, of 82259.17 cm^{-1}. The Doppler shift from this central frequency is described by $\upsilon = \upsilon_0\left(1 \pm \frac{v}{c}\right)$, where v is the velocity, c is the speed of light, and υ is the Doppler shifted frequency. A Gaussian-shaped Doppler profile can be directly related to a translational temperature, T,[1] assuming a Boltzmann translational energy distribution:

$$T = \frac{\left(\frac{fwhm}{2\upsilon_0}\right)^2 m_{H(D)}c^2}{2k\ln 2}$$

where the $fwhm$ (cm^{-1}) is the breadth of the Gaussian Doppler profile, $m_{H(D)}$ is the mass of the H or D atom, and k is the Boltzmann constant. The product translational energy distribution, $P(E_T)$, is derived from the Maxwell-Boltzmann speed distribution and can be determined once the temperature is known:

$$P(E_T)dE_T = \frac{2}{\pi^{1/2}(kT)^{3/2}} E_T^{1/2} e^{-E_T/(kT)} dE_T$$

An example Gaussian Doppler profile, corresponding to a spatially isotropic H-atom velocity distribution with a temperature of 5200 K, is shown in the left panel of Figure 1. The lower axis shows the Doppler shift from the central frequency, while the upper axis shows the corresponding velocity along the laser propagation axis. The

Doppler profile is converted to a translational energy distribution using the above procedure in the right panel of Figure 1. Note that this conversion is exact in the case of a Gaussian shaped Doppler profile.

The Gaussian Doppler profile is also fit using the new analysis procedure described in Chapter 3 of this thesis. A discrete basis set is fit to the Doppler profile in a chi-squared minimization routine by varying the weighting of each velocity component. A discrete set of velocity components spaced by ~1800 m/s, corresponding to the experimental linewidth (0.5 cm^{-1}), is utilized. The resultant fit is shown as a jagged line in the left hand panel of Figure 1.

The weighting of the velocity basis functions yields the speed distribution. This is converted to the translational energy distribution, $P(E_T)$, shown as discrete points in the right hand panel of Figure 1. The new analysis method yields a discrete translational energy distribution which reproduces that obtained using the Maxwell-Boltzmann distribution, although limited by the experimental resolution. A finer grid of velocity basis functions would yield an improved fit to the Doppler profile and overall decrease in uncertainty for the corresponding $P(E_T)$ distribution. As evident in Figure 1, there is larger uncertainty in the weighting of the discrete basis functions at low E_T, corresponding to small Doppler shifts, than at higher E_T with larger Doppler shifts. This arises because a greater number of basis functions can potentially contribute to the fit of the Doppler profile near line center than in the wings. This uncertainty is combined with the experimental uncertainty derived from repeated measurements of the Doppler

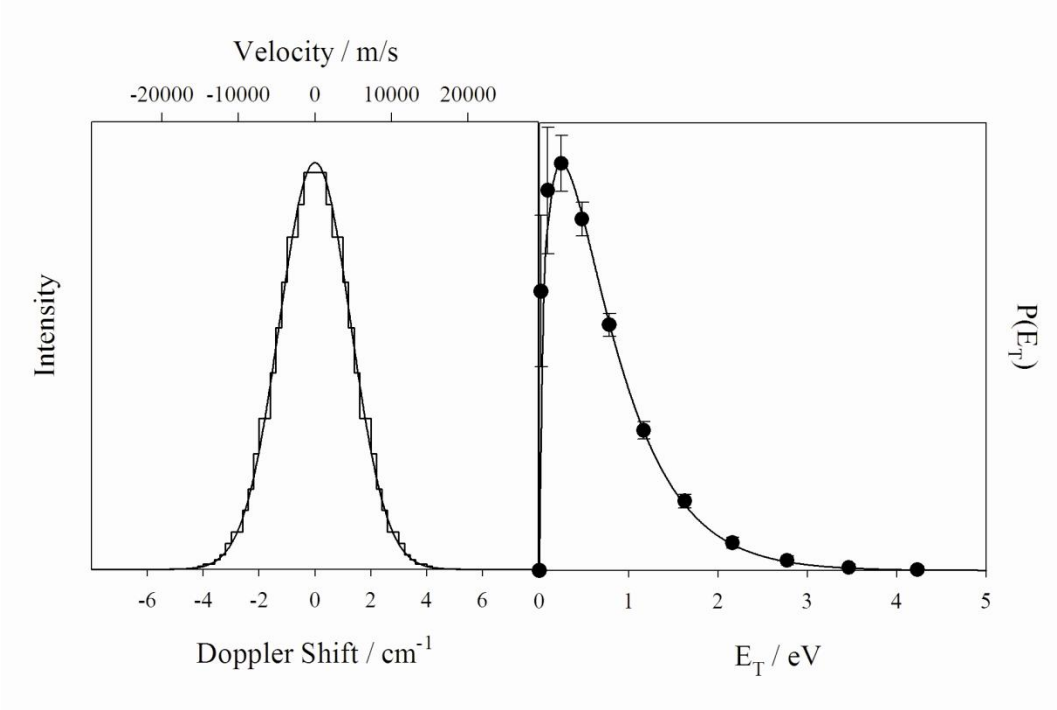

Figure 1. Example Gaussian Doppler profile (left panel) plotted as a function of Doppler shift and velocity. The corresponding translational energy distribution (right panel) can be directly determined using a Maxwell-Boltzmann distribution (solid line). The Gaussian Doppler profile is also fit using a new analysis procedure, which makes no assumption of the functional form of the Doppler profile, and the resultant summed discrete step functions are shown (left panel). The $P(E_T)$ distribution obtained using the new analysis procedure (black circles, right panel) reproduces that derived from the Gaussian Doppler profile.

profiles, typically 10-15%, to give the error bars in the $P(E_T)$ distributions presented in Figure 4 of Chapter 3 of this thesis.

II. Reanalysis of H/D-atom Doppler profiles from OH $A\ ^2\Sigma^+ + D_2$

The previously published H/D-atom Doppler profiles[5] resulting from reactive quenching of OH $A\ ^2\Sigma^+$ by D_2 have been reanalyzed here using the new analysis procedure. The summed discrete step functions representing the best fits from the new analysis procedure are superimposed on the Doppler profiles in Figure 2. These fits are transformed into the $P(E_T)$ distributions shown in Figure 4 (middle panels) of Chapter 3 of this thesis.

The earlier analysis of the D-atom Doppler profile was based on the sum of two Gaussian functions, which necessarily gave rise to a bimodal $P(E_T)$ distribution. The revised analysis of the D-atom Doppler profile (Figure 2), which makes no assumption of its functional form, yields a notably different $P(E_T)$ distribution that can be viewed as a primary peak at low E_T with a long tail extending out to higher energies as shown in Figure 4 of Chapter 3 of this thesis. The shape of the $P(E_T)$ distribution can be reasonably well represented using either one or two lognormal distributions. Thus, the $P(E_T)$ distribution derived from the new analysis does not lead to an obvious separation into two distinct components as had been reported previously.[5]

In the prior analysis of the H-atom Doppler profile from OH $A\ ^2\Sigma^+$ by D_2, the data was fit to a single Gaussian function, neglecting points near line center that were noisy. This led to a broad $P(E_T)$ distribution with an average translational energy of 1.8 eV.

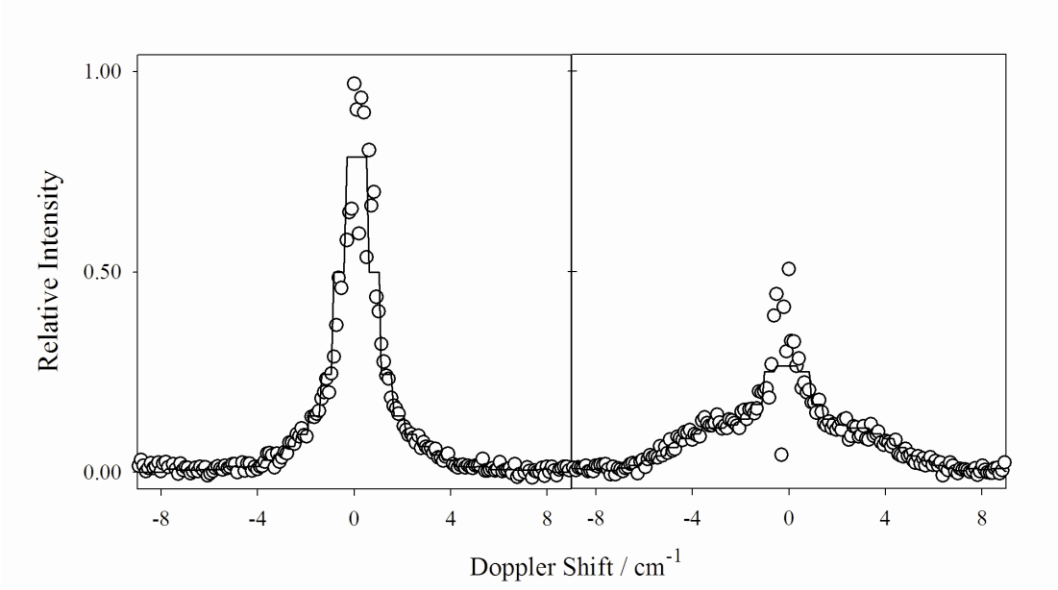

Figure 2. Doppler profiles arising from quenching of OH $A\ ^2\Sigma^+$ by D_2, with original data (open circles) reproduced from Todd et al. (Ref. 5) and refit using the new analysis method. The left and right panels show the D- and H-atom Doppler profiles for the D + HOD and H + D_2O product channels, respectively. The summed discrete step functions representing the best fits from the new analysis procedure are superimposed on the Doppler profiles.

Newer data acquired in the present work for other isotopic variants show highly effective background subtraction near line center (see Figure 2, Chapter 3 of this thesis), and thus the entire data set is included in reanalysis of the H-atom Doppler profile from OH $A\ ^2\Sigma^+$ + D_2, including points near line center. The revised analysis results in a different $P(E_T)$ distribution, which is modeled much better with the sum of two lognormal distribution functions as compared to a single lognormal function. The $P(E_T)$ distribution exhibits a distinctive peak at ~1.8 eV and suggests a smaller peak at low E_T.

III. Revised analysis of H-atom Doppler profile for OH $A\ ^2\Sigma^+ + H_2$

Doppler measurements for the H-atom products from reactive quenching of OH $A\ ^2\Sigma^+$ by H_2 were repeated in the present study and analyzed using the new fitting procedure, as shown in Figure 3. This gives essentially the same $P(E_T)$ distribution as that derived from reanalysis of previously reported data.[3] As discussed in Chapter 3 of this thesis, this $P(E_T)$ distribution shows a prominent peak at low translational energies followed by a secondary broader peak at approximately 2.6 eV with a tail that extends to the energetic limit. The previously reported $P(E_T)$ distribution, based on the original Gaussian fitting procedure (sum of two Gaussian functions), had a similar bimodal shape but with somewhat different characteristics: It had a narrow component at low translational energy (~0.15 eV) and a broad component at higher energy with average E_T of 2.0 eV.[3,5] Again, the new analysis (and subsequent results) is preferred because it makes no implicit assumption of the functional form of the Doppler profile. The

properties of the product translational energy distributions following reactive quenching of OH $A\ ^2\Sigma^+$ by H_2 and its isotopic variants are summarized in Table 1.

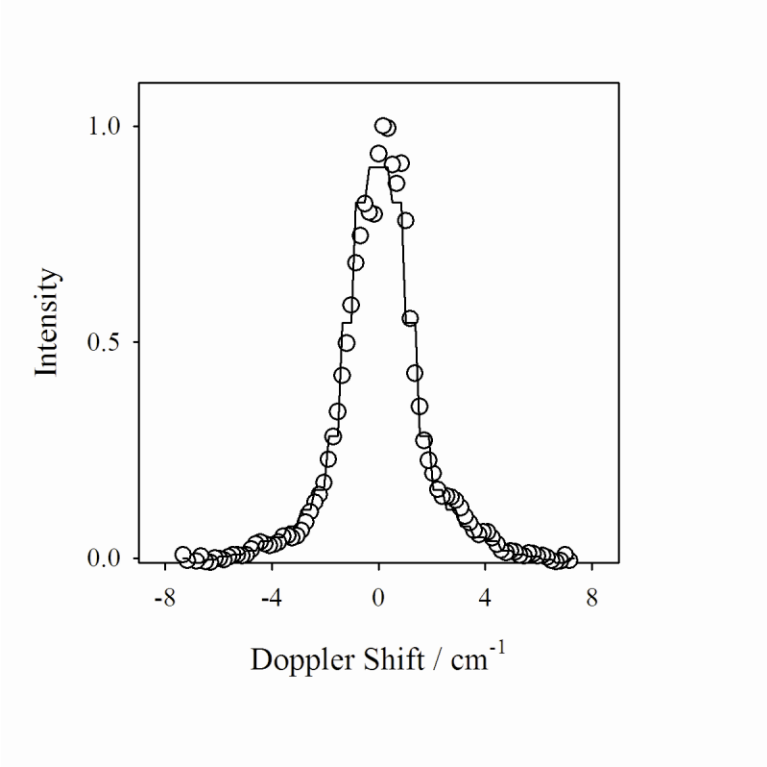

Figure 3. Doppler profile of the H-atom products resulting from quenching of OH $A\ ^2\Sigma^+$ by H_2, as repeated in the present study (open circles). The fit through the data is the summation of the discrete velocity basis functions from the new analysis procedure.

Table 1. Parameters characterizing product translational energy distribution following reactive quenching of OH $A\ ^2\Sigma^+$ by H_2 and its isotopic variants. Average energy released into product translation $\langle E_T \rangle$, fraction of available energy E_{avail} deposited into translation of products $\langle f_T \rangle$, and fractional contribution from abstraction or insertion product channel are listed.

	$\langle E_T \rangle$ (eV)	$\langle f_T \rangle$	Product Channel
OH $A\ ^2\Sigma^+ + H_2 \rightarrow H + H_2O$ (E_{avail} = 4.72 eV)[a]			
Anderson et al.[b]	0.84	0.18	
Fu et al.[c]	0.74	0.16	0.99 (abstraction)
Fu et al.[c]	1.3	0.28	0.01 (insertion)
OH $A\ ^2\Sigma^+ + D_2 \rightarrow$ **D** + HOD (E_{avail} = 4.72 eV)[a]			
Todd et al.[d]	0.56	0.12	0.57
Fu et al.[c]	1.2	0.26	0.98 (abstraction)
Ortiz-Suarez et al.[e]	0.8	0.16	(abstraction)
OH $A\ ^2\Sigma^+ + D_2 \rightarrow$ **H** + D_2O (E_{avail} = 4.80 eV)[a]			
Todd et al.[d]	1.1	0.23	0.43
Fu et al.[c]	1.3	0.27	0.02 (insertion)
OD $A\ ^2\Sigma^+ + H_2 \rightarrow$ **H** + HOD (E_{avail} = 4.71 eV)[a]			
This work	0.48	0.10	0.75
OD $A\ ^2\Sigma^+ + H_2 \rightarrow$ **D** + H_2O (E_{avail} = 4.64 eV)[a]			
This work	0.82	0.18	0.25

[a] E_{avail} takes into account changes in OH/OD transition frequency, zero-point energy for the different isotopes of water (Ref. 2), and E_{coll} ~ 0.005 eV.

[b] Analysis using new method for H-atom Doppler profile from this work and Ref. 3.

[c] Trajectory calculations from Ref. 4.

[d] Reanalysis of H- and D-atom Doppler profiles from Ref. 5.

[e] Crossed molecular beam study from Ref. 6 with E_{coll} ~ 0.16 eV.

References

1 R. N. Zare and D. R. Herschbach, Proc. IEEE **51**, 173 (1963).

2 M. W. Chase, J. L. Curnutt, J. R. Downey, R. A. McDonald, A. N. Syverud, and E. A. Valenzuela, J. Phys. Chem. Ref. Data **11**, 695 (1982).

3 D. T. Anderson, M. W. Todd, and M. I. Lester, J. Chem. Phys. **110**, 11117 (1999).

4 B. Fu, E. Kamarchik, and J. M. Bowman, J. Chem. Phys. **133**, 164306 (2010).

5 M. W. Todd, D. T. Anderson, and M. I. Lester, J. Phys. Chem. A **105**, 10031 (2001).

6 M. Ortiz-Suárez, M. F. Witinski, and H. F. Davis, J. Chem. Phys. **124**, 201106 (2006).

APPENDIX II
Photodissociation of CH_2I_2 at 313 nm

The experimental research presented in this chapter was performed at the University of Pennsylvania. This appendix was submitted as online supplementary material in conjunction with Chapter 6 of this thesis.

Reference: J. H. Lehman, H. Li, M. I. Lester, *Chem. Phys. Lett.,* submitted (2013).

Numerous experimental studies have probed the iodine atom products following excitation of CH_2I_2 to electronic states of B_1 symmetry via the lowest two absorption bands. The primary findings are briefly summarized here. Dissociation of CH_2I_2 is prompt compared to the period of rotation as evident from the anisotropic angular distribution of the iodine photofragments.[1] The anisotropic distribution is characteristic of a $B_1 \leftarrow A_1$ transition,[1-4] confirming the B_1 symmetry of the two lowest excited states and the ordering of electronic states predicted by a simple exciton model.[1] In addition, the translational energy release to iodine atoms is only a small fraction of the available energy, indicating that the CH_2I fragments are generated with high internal excitation. Specifically, some 75 to 90% of the available energy is channeled to internal excitation of CH_2I radicals produced with ground state I ($^2P_{3/2}$) and/or spin-orbit excited I*($^2P_{1/2}$) cofragments.[2-5]

The photodissociation of CH_2I_2 and subsequent ionization of the I ($^2P_{3/2}$) or I* ($^2P_{1/2}$) atoms by 2+1 REMPI can be examined in a one-laser (one-color) experiment, as previously explored by Xu *et al.* in the 277-304 nm range.[4] In the present study, a one-color experiment of CH_2I_2 photodissociation and subsequent ionization of the I* ($^2P_{1/2}$) products is performed at 313 nm. We are extending the earlier investigation to longer wavelength because of the utility of 2+1 REMPI at 313 nm as a probe of the I* ($^2P_{1/2}$) products from photodissociation of CH_2I_2 at 248 nm presented in Sec. III of Chapter 6 of this thesis. The I* yield [combined absorption and quantum yield (~0.2)][6,7] from probe laser photolysis of CH_2I_2 (background) is reduced compared to other shorter wavelengths suitable for 2+1 REMPI detection of I* ($^2P_{1/2}$).[8-10]

Following 313 nm photolysis of CH_2I_2, the resultant one-color image and reconstruction for the $CH_2I + I^*$ ($^2P_{1/2}$) pathway is shown in the top panel of Figure 2 in Chapter 6 of this thesis, where the probe laser polarization is set parallel to the plane of the detector. The total kinetic energy release (TKER) profile from the reconstructed image is shown on the left side of Figure 2a of Chapter 6 of this thesis. Using a Gaussian fit to the TKER profile, the average total translational energy, $\langle E_T \rangle$, is approximately 1300 cm^{-1} with a *fwhm* ~ 700 cm^{-1}. Given the available energy of ~6400 cm^{-1}, the $\langle E_T \rangle$ indicates that approximately 80% of the available energy goes into internal excitation of the CH_2I fragment with $\langle E_{int} \rangle$~5100 cm^{-1}. The high degree of CH_2I internal excitation is in accord with previous photodissociation results at somewhat shorter wavelengths (277-305 nm) corresponding to the $2B_1$ excited state of CH_2I_2.[4]

When the probe laser is operated with the polarization parallel to the plane of the detector, as in the left image of the main text Figure 2a, a β parameter of 1.15(4) is derived from the angular distribution. This angular distribution is obtained around the peak of the TKER feature in the image reconstruction from the 313 nm photodissociation process. Using the model outlined in Chapter 6 of this thesis, the C_{2v} symmetry of CH_2I_2 can be used to predict β parameters based on the angle between the transition dipole moment and the recoil velocity vectors. The transition dipole moment for a $B_1 \leftarrow X\,^1A_1$ transition in CH_2I_2 with C_{2v} geometry would lie parallel to the I-I direction.[1,3,4] Using the experimentally determined ground state ICI angle (114.7°),[11] the angle χ is found to be ~33°, resulting in a predicted β = 1.13, which is very close to the present experimental observation and similar to what was observed at other excitation

wavelengths within the $2B_1$ band.[1,3,4] Since the observed β parameter from I* products matches the predicted anisotropy for a $B_1 \leftarrow X\,^1A_1$ transition, the photodissociation of CH_2I_2 at 313 nm investigated in this work appears to probe only the adiabatic dissociation pathway from the $2B_1$ excited electronic state, which correlates to the I* product channel. Note that the previously reported I* quantum yield (20%) suggests that other nonadabatic channel(s) are involved in the dissociation dynamics.[6,7]

References

[1] M. Kawasaki, S.J. Lee, R. Bersohn, J. Chem. Phys. 63 (1975) 809.
[2] P.M. Kroger, P.C. Demou, S.J. Riley, J. Chem. Phys. 65 (1976) 1823.
[3] K.W. Jung, T.S. Ahmadi, M.A. El-Sayed, Bull. Korean Chem. Soc. 18 (1997) 1274.
[4] H.F. Xu, Y. Guo, S.L. Liu, X.X. Ma, D.X. Dai, G.H. Sha, J. Chem. Phys. 117 (2002) 5722.
[5] S.L. Baughcum, S.R. Leone, J. Chem. Phys. 72 (1980) 6531.
[6] T.F. Hunter, K.S. Kristjansson, Chem. Phys. Lett. 90 (1982) 35.
[7] J.B. Koffend, S.R. Leone, Chem. Phys. Lett. 81 (1981) 136.
[8] A. Gedanken, M.B. Robin, Y. Yafet, J. Chem. Phys. 76 (1982) 4798.
[9] C.J. Hu, S.X. Pei, Y.L. Chen, K.P. Liu, J. Phys. Chem. A 111 (2007) 6813.
[10] Y.J. Jung, Y.S. Kim, W.K. Kang, K.H. Jung, J. Chem. Phys. 107 (1997) 7187.
[11] S.A. Kudchadker, A.P. Kudchadker, J. Chem. Ref. Data 4 (1975) 457.